Geometric and Dynamic Phases in Rydberg State Interferometry

J. D. R. Tommey

Supervisor Prof. S. D. Hogan

A thesis presented for the degree of
Doctor of Philosophy

Department of Physics & Astronomy
University College London
United Kingdom
January 19, 2025

Declaration

I, Jake David Raymond Tommey confirm that the work presented in this thesis is my own. Where information has been derived from other sources, I confirm that this has been indicated in the thesis.

Parts of this thesis have been, or are in preparation to be, published as follows:

Chapter 4 J. D. R. Tommey and S. D. Hogan, "Resonant rydberg-atom–microwave-field interactions in the ultrastrong-driving regime: Beyond the rotating-wave approximation," Physical Review A, vol. 100, no. 5, p. 053 417, Nov. 25, 2019, Publisher: American Physical Society

Chapter 6 J. D. R. Tommey and S. D. Hogan, "Matter-wave interferometry with helium atoms in low-l rydberg states," Physical Review A, vol. 104, no. 3, p. 033 305, Sep. 3, 2021, Publisher: American Physical Society

Chapter 7 paper in preparation

Signed: _____

J.D.R. Tommey

Abstract

Rydberg states of atoms or molecules are characterised by having a highly excited valence electron. This leads to many exaggerated properties such as extended lifetimes and large susceptibilities to electromagnetic fields.

In Part I of this thesis we explore such properties, looking at the ultra-strong driving regime of the Rabi model with Rydberg states, observing coherent Rydberg atom and microwave field interactions. Under ultra-strong driving simpler models break down, so Floquet methods are used and show excellent experimental agreement. The results presented are of importance for applications in the detection and precise calibration of microwave fields and in fast quantum state preparation for quantum information processing.

The appeal of Rydberg states with their unique properties has meant that there has been an increased focus for applications in quantum technologies such as for Rydberg state sensing. Part II of this thesis develops a coherent approach to this by performing interferometry with Rydberg states of atoms. We demonstrate experiments that probe dynamic and geometric phases in a Ramsey-type interferometer using Rydberg states of helium.

A first experiment involves inhomogeneous electric-field gradients. Forces are applied to create a half-loop Stern-Gerlach interferometer. These experiments replicate approaches seen with atom-chip interferometers, resulting in coherent superpositions of spatially separated momentum states. The experiment demonstrated here used low-ℓ Rydberg states in order to overcome non-adiabatic losses seen in a previous experiment using circular Rydberg states. Dispersive effects fundamentally limited this approach. Future experiments aimed at overcoming this dispersion could allow for a full-loop interferometer that could be sensitive to inertial effects.

This inspired an experiment where the phase due to the motional-Stark effect is measured in a Ramsey-type interferometer. The motional-Stark phase is closely related to the He-McKellar-Wilkens geometric phase, an electromagnetic dual of the Aharonov-Bohm phase. The motional-Stark effect couples the external and internal motion of the atom and under certain electro-magnetic potentials can lead to a non-dispersive phase. The use of the motional-Stark phase for interferometery presents some interesting future application including the implementation of an atom diode, performing accelerometry with Rydberg states, and exploring topological effects in neutral atom systems.

Impact statement

In the last few decades, the field of Rydberg physics has seen a resurgence, pushing the field in many new and exciting directions from molecular physics to quantum sensing, quantum simulation and beyond. This interest can be attributed to the many attractive features of Rydberg states including enormous electric transition dipole moments in the microwave frequency range and strong tuneable long-range dipole-dipole interactions. Furthermore, this can be credited to advancements in experimental techniques, meaning Rydberg atoms are now more readily prepared and manipulated.

The potential new research directions that are relevant to the work presented in this thesis include: Quantum sensing, the realisation of technologies that exceed the accuracy and remit of classical sensors, and accelerometery, with potential applications for better understanding the nature of gravity in anti-matter systems, and as an alternative approach to cold-atoms for low sensitivity applications.

The research of this thesis makes the following contributions to their associated fields of study:

1. **Chapter 4:** The limitations of models of atom-light interactions involving Rydberg states are pushed as we explore the *ultra-strong* driving regime. Standing alone, this result is useful as reference for other researchers using these models. The effects such strong driving can have on the structure of energy levels can have applications for the deceleration and trapping of Rydberg atoms and molecules, with applications in hybrid quantum computing.

2. **Chapter 6:** In this chapter I describe experiments of Stern-Gerlach type interferometery with Rydberg states. Experiments of this nature were first performed at UCL using circular states. These states suffered non-adiabatic losses in the inhomogenous field gradients used. In the experiments described here the experiments are repeated using low-ℓ states which are isolated from nearby states and are not sensitive to adiabatic losses. We increase the approaches robustness and therefore achieve much larger coherent separations between the two paths. This has applications in an eventual full-loop interferometer which would be sensitive to inertial effects. This makes possible further experiments ultimately aimed at probing antimatter gravity with Rydberg positronium.

3. **Chapter 7:** Here I utilise the feature of large electric dipole moments of atoms in Rydberg states to perform a Ramsey-type inter-

ferometer that is sensitive to the motional-Stark phase. Measurements of this phase are difficult to measure with ground state atoms due to their small electric dipole moments. The approach could allow for the realisation of a Rydberg state interferometer sensitive to inertial effects. The geometric nature of the phase may make this possible in a way which is dispersionless and applicable in situations in which an atomic beam of atoms is used.

Acknowledgements

My partner, Fariha, I don't think it is an overstatement to say that without your support I would not have completed this thesis; I am sorry that you now know more about Rydberg state interferometery than you ever wished. I love you with all my heart.

My grandparents, Gommie and Gompsie, you have done so much to support me over the years, thank you for letting me live with you when I needed to and for being so loving and supportive to all of us grandchildren.

My parents, Gavin and Sheryll. Thank you for never imposing a path on me and raising me with love. I could not have wished for better parents. Lorna, thank you for letting me live with you during the lockdown while I finished the research phase of this project, it was a lovely time within an overall terrible time! Also, since for all the love and support you have continued to give me. John, thank you for all the lovely meals and conversations over the years, I really appreciate the wisdom and perspective you have imparted on me, I always leave your company calmer and with a clearer mind.

My sister, Tat, I loved all the visits to the spooky house and really appreciate you and how caring and thoughtful you are. Having you in my life is a blessing, I love you to the moon and back. Jack, you probably only distracted me over the duration of the PhD, but it was always appreciated, I love you brother. My nephew Ozzy, watching you grow from a baby into such a loving and funny young man has been a complete joy throughout this period of my life. Little Flo-flo your confidence is inspiring and your dance moves even more so.

Thank you to all the housemates I have had: Evan, Liam, Paige, Anaïs, Nida, Jamie, Edith, Callum, Gemma, Anna and Stephen. It has been a really great period of my life, sorry you had to put up with me for some of it. And to all the other friends who have supported me when I needed it: Suraj, Jamie, Elliott, Zac, Laura, Joey, Lana, Grace, Ben, and the rest!

The best thing about doing my PhD through a CDT was all the people I met along the way. Alex, Andrew, Charlie, Fagin, Jingyu, Laura, Lindsey, Lisa, Ollie, Tom, Tom, Virginia; you all mean a lot to me.

Finally, I'd like to thank my supervisor Stephen Hogan, it was a pleasure to work with you all these years.

Dedication

I dedicate this thesis to my grandfather, Raymond Tommey or Gompsie.

Academia has exposed me to some brilliant people who have taught me a great deal about technical subjects, but no person or book has ever taught me as much about life and shared as much wisdom with me as you have. You have always been the person I have looked up to the most, and I hope I have made you as proud of me as I am of you.

Contents

1
Introduction to Rydberg states

> They are floppy, fragile, and huge.
>
> Daniel Kleppner

1.1 Early Rydberg state experiments

TOWARDS the end of the 19^{th} century, observing the emission and absorption spectra of atoms had given us the first glimpse of the quantised nature of light. Each individual atomic element studied could be associated with its own distinct pattern of wavelengths of light that could be absorbed or emitted, known as its absorption or emission spectrum. Johannes Rydberg was the first to pinpoint the relationship between these lines, that represent intervals between energy levels, and the inverse of their wavelengths.

Rydberg was investigating the spectral lines emitted by alkali elements and found an empirical formula describing the separation of wavelengths in atomic spectra, the general form being,

$$\frac{1}{\lambda} = R\left(\frac{1}{n_1^2} - \frac{1}{n_2^2}\right), \tag{1.1}$$

where R is a constant that depends on the atomic species, n_1 is the principal quantum number of a lower energy level, and n_2 is that of the initial higher energy level in the transition [1]. This relationship became known as the Rydberg formula.

This was a significant advance as atomic emission spectra were previously understood only in terms of wavelengths – hiding the more fundamental energy-based relationship between the spectral lines. Here Rydberg unified the many different series observed within a given atomic species, as demonstrated in Fig. 1.1 for hydrogen, into a unified set of energy levels. The integer nature of the variables n in this formula alludes to the quantum revolution to come in the following decades.

The first physical model of the atom to successfully explain Rydberg's formula was the Bohr model of hydrogen. In this model, the electron is viewed as a point particle orbiting in a central potential whose value falls off as $1/r$. The model is in close analogy with the

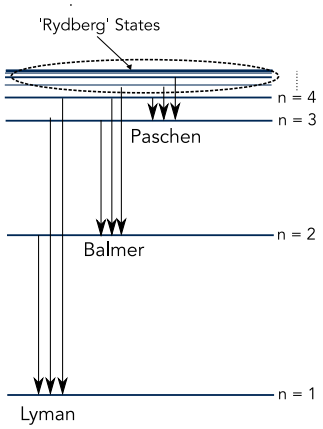

Figure 1.1: Visualization of the Lyman, Balmer, and Paschen emission series of the hydrogen atom, illustrating electron transitions between energy levels. The Lyman series consists of transitions ending at the first energy level ($n = 1$), the Balmer series ends at the second energy level ($n = 2$), and the Paschen series ends at the third energy level ($n = 3$). The figure also highlights the high-energy Rydberg states for each series, where the electron transitions originate from very high energy levels ($n \gg 1$) and approach the ionization limit. These Rydberg states are marked by large atomic orbitals and unique quantum properties.

celestial mechanics of planetary systems, where an electric field from the positive core replaces the gravitational field, 1.2.

This model predicts quantised energy levels with energy $E_n \propto \frac{R}{n^2}$, in agreement with the experimentally observed spectral lines. Despite the successes of the Bohr approach in predicting spectral lines, there is a conflict in the assumption of a classically rotating electric charge. The rotating charge (i.e. electron) should radiate energy, causing it to spiral inwards and have unstable orbits. Furthermore, this model is insufficient to explain phenomena such as the Zeeman and Stark splittings of spectral lines in magnetic and electric fields.

The Bohr-Sommerfeld model [2], an extension of the Bohr model proposed by Arnold Sommerfeld, introduced the quantization of the $\hat{z}$ component of angular momentum, incorporating elliptical orbits alongside the circular ones. For a given principal quantum number n, these elliptical orbits exhibit energy degeneracy, which can be lifted in the presence of external electromagnetic fields. This refinement allowed the model to successfully explain the Stark and Zeeman effects by accounting for the splitting of spectral lines under electric and magnetic fields. However, while the Bohr-Sommerfeld model offered significant advancements, it still falls short of a full quantum mechanical description, notably in its inability to explain electron spin and to provide a fully accurate explanation of fine-structure effects requiring a more comprehensive quantum framework.

A critical insight from the Bohr model is good intuition for the 'physical extent' of an atom as the Bohr radius a_0. This is the radius of the orbit of the least energetic state of an idealised hydrogen atom (comprised of an electron bound to an infinitely heavy positive point charge), shown in Fig. 1.2. The radius of this orbit scales as $r \propto n^2$, and for states with large n, this can result in orbits of many thousands of Bohr radii. States of this type are called Rydberg states as Rydberg's formula provides a good account of their energies.

An atom in a Rydberg state appears to behave like a hydrogen atom with some exaggerated properties. For example, due to the valence electron spending most of its time far from the positive core, these states possess significant electric dipole moments. The theoretical details behind these properties are discussed in Chap. 2. Another such exaggerated property is the cross-sectional area, which scales as n^4, making Rydberg states have enormous volumes.

Many of these properties were explored experimentally in the first half of the 20th century. For example, in [3], Amaldi and Segré examined the energy shifts of high-lying potassium (K) states in a dielectric gas. Additionally, Jenkins and Segrè observed the *quadratic Zeeman shift* in high-lying Rydberg states [4]. This shift arises as a second-order effect, where the energy shift is proportional to the square of the applied magnetic field, given by $\Delta E \propto B^2$. Such second-order interactions reflect the more complex coupling of the atom's magnetic moment to the external field beyond the linear Zeeman effect.

Interest in these exotic states declined over the next couple of decades, until the discovery of Rydberg states in space. This led to increased

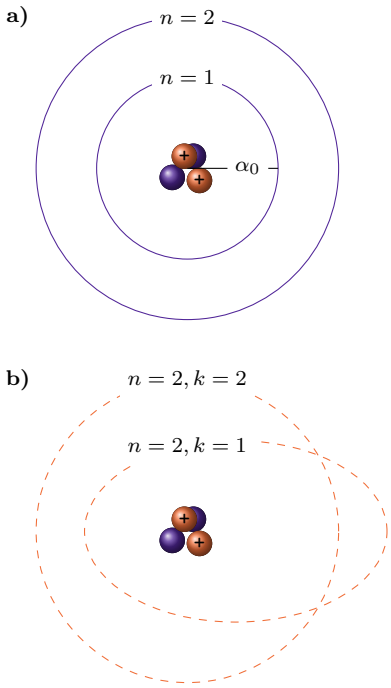

Figure 1.2: Early quantum models of the atom, such as the Bohr model and its extension, the Bohr-Sommerfeld model, provide valuable intuition for understanding the properties of Rydberg states. In a), the Bohr model quantizes electron orbits in circular paths around the nucleus, with energy levels inversely proportional to the square of the principal quantum number n. The Bohr radius, α_0, represents the radius of the electron's orbit in the ground state. In b), the Bohr-Sommerfeld model expands on this by incorporating elliptical orbits and introducing an additional quantum number, the radial quantum number k. This extension resolves degeneracies in the energy levels and provided an explanation of fine structure phenomena, including Zeeman and Stark shifts, where spectral lines split in the presence of magnetic and electric fields.

interest in Rydberg physics, particularly for astronomical and plasma physics [5]. The growing use of Dye laser systems in the 1970s is the primary catalyst for many current research directions involving Rydberg atoms. This made it feasible to optically excite particular transitions and controllably populate certain Rydberg states in large numbers.

Properties of Rydberg states made them valuable tools for exploring several topics within quantum physics, particularly in quantum electrodynamics. The large transition dipole moments of Rydberg states combined with many Rydberg-Rydberg transitions in the centimetre region of the electromagnetic spectrum make them appealing. The interaction between a Rydberg atom and a microwave cavity, a field known as cavity-QED has resulted in many interesting results.

Cavity-QED experiments use the highest angular momentum Rydberg states in a given manifold, known as circular states. Due to angular momentum transition rules, these only possess a single radiative decay channel which can be suppressed by modifying the environment to exclude the mode associated with this transition frequency. Kleppner showed theoretically that the lifetime of an atomic state could be enhanced by placing it in a wave-guide with dimensions tuned to the emission frequency [6]. At this time, experimental interest and schemes to excite these states were emerging [7][8]

This direction continued with a series of experiments exploring ever more precise experiments exploring the interaction between atoms and electromagnetic fields, resulting in many beautiful experiments by the group of Serge Haroche. His pioneering work involved sending individual Rydberg atoms through a high-Q superconducting microwave cavity, where the atoms would interact with a quantized electromagnetic field. This allowed the detection of single photons and the observation of phenomena like quantum superposition and entanglement[9], [10]. By using single atoms and controlling their interaction with single photons, Haroche's experiments made critical advances in the understanding of quantum mechanics and the nature of light-matter interaction, culminating in his Nobel Prize in 2012 [11].

1.2 Applications of Rydberg states of matter and anti-matter

1.2.1 Quantum Sensing

Rydberg states exhibit a high sensitivity to external electric and magnetic fields, making them ideal candidates for precise field sensing [12], [13]. The advent of tunable single-frequency diode lasers has significantly enhanced the ability to excite specific energy levels, especially in alkali atoms. This, in turn, has allowed for field sensing across a broad frequency spectrum, ranging from MHz to THz.

The interactions of Rydberg states with both RF and static fields are well-understood [14]. Off-resonant fields cause shifts in energy levels, while on-resonant fields induce a splitting of resonances, as exemplified by the Autler-Townes effect [15]. These effects provide a

detailed understanding of the external fields responsible for the observed transitions, making Rydberg atoms effective tools for probing electromagnetic environments.

The commercialization of Rydberg-based sensors is progressing rapidly. Alkali atoms in vapor cells are emerging as promising mediums due to their compact size and room-temperature operation [16], [17]. Notably, recent advancements have enabled the detection of both the magnitude and phase of external fields [18], broadening the practical applications of Rydberg sensors in various domains, including telecommunications, defence, and environmental monitoring.

1.2.2 Quantum information processing

Rydberg states have become a promising tool in quantum information processing due to their strong dipolar interactions over micrometer distances [19]. These interactions allow the implementation of quantum gates, particularly using the Rydberg blockade mechanism. This mechanism occurs when the excitation of one Rydberg atom prevents the excitation of nearby atoms [20]. This phenomenon is critical to quantum logic gate operations such as the Controlled-NOT (CNOT) gate [21].

The qubit states used in such systems are typically the hyperfine ground states, which are stable due to their weak quadratic Zeeman shift and long lifetimes. Techniques like trapping atoms in optical tweezers or lattices have become the primary methods for building these systems [22], [23]. Rydberg states are also being utilized for analogue quantum simulations, where arrays of Rydberg atoms are set up to mimic and explore complex Hamiltonians [24].

Hybrid approaches, such as coupling Rydberg atoms to superconducting circuits, are another area of active research. This hybrid coupling has already been demonstrated experimentally, combining the unique advantages of Rydberg atoms and superconducting systems for potential applications in quantum information processing [25], [26].

1.2.3 Rydberg optics and beam experiments

The large electric dipole moments of Rydberg states can be harnessed to apply forces using inhomogeneous electric fields. The force experienced by an atom or molecule in such a field is determined by the spatial gradient of the Stark energy shift, as described by the following equation:

$$\mathbf{f} = -\nabla E_{\text{Stark}}, \tag{1.2}$$

where $\mathbf{f}$ represents the force applied to the atom or molecule, and ∇E_{Stark} is the spatial gradient of the Stark energy, which is the energy shift experienced by the Rydberg atom due to the external electric field. The negative sign indicates that the force is directed along the gradient of decreasing energy.

This Stark-induced force can be used to decelerate and trap atoms or molecules in states with static electric dipole moments [27]–[29].

Such control over atomic or molecular motion is crucial in various applications, including precision measurements, quantum simulations, and the development of quantum technologies.

Rydberg states can be prepared in a wide range of atomic and molecular species. Therefore deceleration and trapping of Rydberg states with inhomogeneous fields gives experimental control over a wide range of atomic and molecular species. This is particularly useful for such species which can only be produced in fast-moving beams.

High-resolution spectroscopy in Rydberg states is of interest for studies of atom-surface interactions [30][31] and studies of ionisation and disassociation [32]. The experiment of [30] that employed microwave spectroscopy techniques to probe stray electron fields close to a surface is illustrated in Fig. 1.3. In many cases, the precision in these types of experiments is limited not by the bandwidth of the laser but by the interaction time [12].

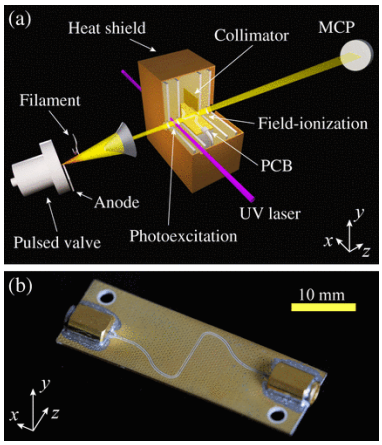

Figure 1.3: Experimental setup for driving Rydberg state transitions using a co-planar wave-guide. The co-planar wave-guide generates a microwave field, which couples to the Rydberg states of the atoms, facilitating control over their internal states [27].

Rydberg physics plays an essential role in the study of anti-matter systems and studies of anti-gravity. Anti-hydrogen is the recombination of anti-protons and positrons [33], or anti-proton collisions with positronium [34]. These high energy collisions result in excited Rydberg states that will eventually decay to ground states that can be trapped [35]. Methods to control them while still in the Rydberg states would be desirable to improve ground state trapping efficiencies in these experiments.

Positronium (Ps), an electron and anti-electron pair, has a very fast decay rate in its ground state [1]. In the Rydberg states, the spatial overlap between the two charges is reduced as the two constituent particles orbit far apart, protecting the state from annihilation. The fluorescence lifetimes are in the same range as those of ordinary matter Rydberg states [37].

[1] The triplet ground-state has a lifetime of 142 ns [36]

Positronium (Ps), particularly in its Rydberg state, holds significant potential for antimatter gravity experiments due to its unique quantum properties. However, one of the key challenges is the high velocity of Ps atoms, which are typically produced by implanting pulsed positron beams into silica targets. This process generates beams travelling at speeds of around 10^5 m/s, making them difficult to decelerate and manipulate for precise gravitational experiments.

Deceleration techniques originally demonstrated for Rydberg atoms and molecules [38] could be adapted for Ps beams. By applying these techniques, it may be possible to slow down and control the fast-moving Ps beams, making them more suitable for sensitive antimatter gravity studies. With this level of control, positronium becomes an excellent candidate for investigating gravitational effects on antimatter [39], [40], potentially paving the way for significant breakthroughs in this field.

The use of inhomogeneous fields has recently been extended to enable coherent manipulation of Rydberg states. In such systems, the applied force is directly proportional to the electric dipole moment of the atom. As a result, a coherent superposition of two Rydberg states leads to a corresponding superposition of momentum states, creating opportunities for interferometry experiments sensitive to inertial ef-

fects. Recent experiments involving Rydberg helium atoms by Palmer and Hogan [41] have started experiments in this direction. Chapter 6 of this thesis builds on these developments.

2
Properties of Rydberg States

Rydberg states, with their highly excited electron orbitals in states with a large principal quantum number, exhibit exaggerated properties when compared to ground states. In this chapter, an emphasis is placed on explaining several of these properties relevant to the research conducted in this thesis. That is, the interactions of the states with various configurations of electric field and their lifetimes. For a more comprehensive look at the many wonderful properties of Rydberg states, a good reference is Gallagher's textbook [14].

2.1 Rydberg states of atoms

2.1.1 Hydrogenic Rydberg states

The Bohr and Bohr-Sommerfeld models, depicted in Fig. 1.2 could not fully explain the properties of the hydrogen atom. A full description of the hydrogen atom was quickly determined in the 1920s using the newly developed theory of quantum mechanics.

This radically new approach no longer considered the electron as a well-defined point-like particle. Instead, the electron is seen as a cloud of electric charge localized around a central positive core. The exact solution for this charge density is found by solving the Schrödinger equation using an inverse potential $U(r) \propto \frac{1}{r}$. For a single electron moving in an inverse potential, this has the form

$$[\nabla^2 + \frac{1}{r}]\psi(r,\phi,\theta) = E\psi(r,\phi,\theta), \tag{2.1}$$

in atomic units, where $\psi(r,\phi,\theta)$ is the electron wave function in spherical coordinates and E is the eigenenergy of the state.

The solution to this equation is separable and may be written as the product of a radial term, given by a Laguerre polynomial, and an angular term, given by a spherical harmonic.

The energy eigenstates can be written as $\psi(r,\theta,\phi) = R_{n\ell}(r)Y_{\ell,m_\ell}(\theta,\phi)$. These solutions are characterised using three quantum numbers: n, ℓ, and m_ℓ. The principal quantum number $n \geq 1$ is found by solving the radial equation and is related to the radial extent of the electron. The orbital quantum number $0 \leq \ell \leq n-1$ represents the total orbital angular momentum. The magnetic quantum number $-\ell \leq m_\ell \leq \ell$ is the projection of the angular momentum along a directional axis.

The energy of an eigenstate to first order is given by

$$E_{n,\ell,m_\ell} = E_{\text{ion}} - \frac{R}{2n^2}. \tag{2.2}$$

Here, E_{n,ℓ,m_ℓ} is the energy of the electron in a hydrogen atom, E_{ion} is the ionisation energy, which is the energy required to completely remove the electron from the atom, and R is the Rydberg constant.

The predicted energies have the same form as those predicted by the Bohr model; only the principal quantum number n is relevant. The differences arise when considering the influence of external fields on the energy levels. These can lift the symmetries and can lead to the emergence of energies which are dependent on the ℓ and m_ℓ quantum numbers.

The average spatial extent of the wave function is given by the following expression:

$$\langle r \rangle = \frac{a_0}{2}[3n^2 - \ell(\ell+1)], \tag{2.3}$$

where $\langle r \rangle$ represents the expectation value of the radial position, and a_0 is the Bohr radius. This equation demonstrates that the radial extent of the wave function scales quadratically with the principal quantum number n, as predicted by the Bohr model, but with an additional term to account for the orbital angular momentum quantum number ℓ.

The ℓ quantum number affects the shape of the wave function and therefore its radial distribution. For low ℓ values, the electron's probability density is more concentrated near the nucleus. As ℓ increases, the centrifugal force can be seen to push the electron out from the nucleus. The Bohr-Sommerfeld model depicted in Fig. 1.2 captures this conceptually with quantum number k instead of ℓ. The $n = 2$, $k = 1$ orbit is less elliptical and has a broader spatial distribution compared to the $n = 2$, $k = 0$ orbit.

Additionally, for each orbital angular momentum quantum number ℓ, the magnetic quantum number m_ℓ can take values from $-\ell$ to $+\ell$, allowing for $2\ell + 1$ orientations of the orbit. The magnetic quantum number m_ℓ describes the projection of the electron's angular momentum along the z-axis, where $m_\ell\hbar$ represents the z-component of angular momentum. In external field-free conditions, m_ℓ does not affect $\langle r \rangle$ as it only determines the orientation of the orbit about the given axis. However this orientation of the orbit can have an impact when an external field is applied, breaking the symmetry.

2.1.2 Non-hydrogenic Rydberg states

The presence of additional electrons and nuclei manifests as corrections to the hydrogenic case. The additional particles in the core introduce a new term in the potential energy of the valence Rydberg electron $U_{\text{core}} \propto \frac{1}{r^4}$. The influence of this term drops faster than that of the hydrogenic $\frac{1}{r}$ Coulomb term, however, it does produce significant effects in regions closer to the core.

The valence electron in a Rydberg state has large $\langle r \rangle$ and most of the probability density is far from the core. This leads to a situation where the equations for the hydrogenic case are nearly correct and only a small correction is required. The correction is given by a phase shift in the radial wave function at the boundary of the core. For states with a higher probability density near the core (i.e., low-ℓ states), this phase shift has a larger effect on the energy levels and other properties of the states.

These non-hydrogenic shifts to the energy levels can be accounted for by introducing a phenomenological quantum defect $\delta_{n,\ell}$, enabling the hydrogenic equation for energy to still apply, such that

$$E_{n,\ell} = E_{\text{ion}} - \frac{R}{(n - \delta_{n,\ell})^2}. \tag{2.4}$$

Here, the principal quantum number n is modified into an effective principal quantum number $n^* = n - \delta_{n\ell}$, where the defect $\delta_{n\ell}$ encapsulates the interactions with the core.

The experiments performed in this thesis make use of $n = 0$ and $n = 1$ Rydberg states of helium. These states have large quantum defects in helium and we will collectively refer to them as low-ℓ states. Their response to applied external electric fields is a tool used extensively throughout these experiments. In the next section we will discuss how the behaviour of these states differs from the equivalent states in hydrogen.

2.2 Lifetimes of Rydberg states

It is important to consider the lifetimes of Rydberg states in order to understand the limits of experiments involving them. The main two decay mechanisms for Rydberg states are radiative emission and black-body induced transitions.

The radiative decay rate Γ_{fl} is given by the sum of all Einstein A coefficients for transitions to states lower in energy [42],

$$\Gamma_{\text{fl}} = \sum_{n\ell m_\ell \to n'\ell' m'_\ell} A_{n\ell \to n'\ell'}. \tag{2.5}$$

The A coefficients can be calculated using Fermi's golden rule,

$$A_{n\ell \to n'\ell'} = \frac{\omega_{nn'}^3}{3c^3} \frac{\ell_{\max}}{2\ell + 1} R_{nl \to n'l'}^2. \tag{2.6}$$

where $\omega_{nn'}$ is the energy difference and $R_{nl \to n'l'}$ is the radial transition dipole moment between the states. There is no explicit dependence on m_ℓ due to degeneracy of these states. The total decay rate is the sum of all possible transitions obeying the selection rules.

An interesting feature of these coefficients is that while the nearby transitions to Rydberg states possess large radial overlaps, and therefore transition dipole moments $R_{n\ell \to n'\ell'}$, the energy difference $\omega_{nn'}$ is very small and so it is those transitions to low-lying levels which dominate the spontaneous decay.

At finite temperatures the presence of a black-body radiation (BBR) field further reduces the lifetime of a state. The probability of a transition of a given frequency is related to the number of photons which exist in the black-body radiation field of that frequency [43],

$$\bar{n} = \frac{1}{\exp\{(\omega/k_B T)\} - 1}. \tag{2.7}$$

Here T is the temperature, k_B is Boltzmann's constant, and ω is the frequency of the photon.

The rate of BBR induced transfer to a given state is then given by the Einstein A coefficient multiplied by the number of photons at that frequency,

$$\Gamma_{\rm BBR} = \sum_{nlm_\ell \to n'l'm'_\ell} \Gamma_{n\ell\to n'\ell'} = \sum_{nlm_\ell \to n'l'm'_\ell} \frac{A_{nl\to n'l'}}{\exp\{(\omega_{nn'}/k_B T)\} - 1}, \tag{2.8}$$

where the sum is over all possible transitions allowed by selection rules.

Here it can be seen that rather than those transitions to low-lying states, the dominant transitions are to states which are closer in energy. This is due to the small occupation numbers of photons corresponding to transitions to low-level states at room temperatures.

The total decay rate is then given by the sum,

$$\Gamma_{\rm decay} = \Gamma_{\rm fl} + \Gamma_{\rm BBR}, \tag{2.9}$$

Rydberg atoms for low-ℓ states in the absence of external fields can enjoy surprisingly long lifetimes which scale as $\tau_{\rm decay} = \frac{1}{\Gamma_{\rm decay}} \propto n^3$.

2.3 Rydberg states in static electric fields

Although the Rydberg states of the atoms are electrically neutral, the large separation between the valence electron and core leads to significant dipoles. Due to the large static and induced polarizabilities of

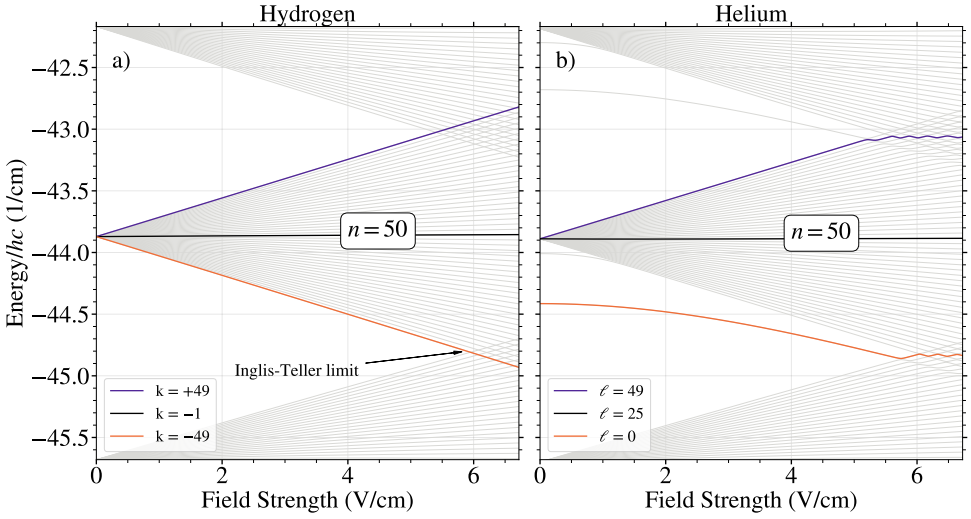

Figure 2.1: Comparison of the Stark maps for hydrogen (left) and helium (right) around $n = 50$ with $|m_\ell| = 0$. In hydrogen (a), the energy levels exhibit exact crossings due to the absence of quantum defects. However, in helium (b), the interaction between the Rydberg electron and the ionic core causes the low-ℓ states (those with small orbital angular momentum and larger defects) to be separated from the rest of the manifold. Additionally, in helium, the presence of these quantum defects leads to avoided crossings at higher electric field strengths, as opposed to the exact crossings observed in hydrogen.

Rydberg states, the application of static electric fields is a useful tool for manipulating a number of their properties.

The effect of the applied field is computed by introducing a static electric field to the Coulomb potential in the Hamiltonian for the valence electron. Rather than a spherically symmetric potential, the electron now moves in a field with cylindrical symmetry. The Hamiltonian for the system can be written as

$$H = H_0 + F\hat{z}. \tag{2.10}$$

Here, H_0 represents the field-free potential and $F\hat{z}$ represents a static electric field along the z direction.

The energy shift in the eigenvalues of the Hamiltonian caused by this field is called the Stark shift. The Stark shift due to this static field is different for hydrogenic states (with no quantum defects) and low-ℓ states in non-hydrogenic atoms with large quantum defects. This we explore in the following section.

2.3.1 Hydrogenic atoms in static electric fields

In hydrogen, the Hamiltonian associated with an applied static electric field can be solved analytically using parabolic coordinates. The solutions are characterized by four quantum numbers: n, the principal quantum number; m, the azimuthal quantum number; and the parabolic quantum numbers n_1 and n_2, which are subject to the constraint $n = n_1 + n_2 + |m| + 1$.

The resulting eigenstates are labelled with the index $k = n_1 - n_2$, which ranges between $-(n-|m|-1) < k < (n-|m|-1)$ in increments of two. The energy of these states to first-order perturbation is

$$E_{n,m,n_1,n_2} = E_{\text{ion}} - \frac{R}{n^2} + \frac{3}{2}nkea_0F + \ldots \tag{2.11}$$

where e is the electric charge, a_0 is the Bohr radius, and F is the electric field strength.

In the presence of an electric field, the states exhibit linear energy shifts $\mu_{n,k} = \frac{3}{2}nkea_0$ because of their static electric dipole moments. The direction of the shift depends on the value of k.

This can be understood by observing the distribution of the electric charge density of the valence electron around the core, as shown in Fig. 2.2. This figure shows the electric charge density in a 2D plane centred on the nucleus of the atom. There is an electric field along the $\hat{z}$ axis. The states at the far edge of the manifold, $k = \pm 49$ for the $n = 50$ manifold shown in Fig. 2.2, have electron charge heavily concentrated on either side of the core.

This results in a dipole that is either energetically aligned or anti-aligned with the field, resulting in either an increasing or decreasing potential energy in the field. The $k = -1$ state, in the center of the figure, has a more symmetrical charge distribution with respect to the applied field axis. This state experiences very little energy shift as the field is increased.

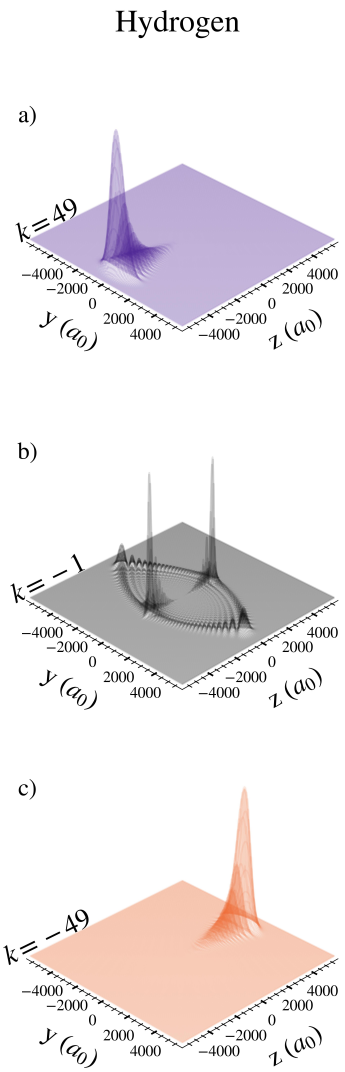

Figure 2.2: Electric charge density in the $(\hat{y}, \hat{z})$ plane for the valence electron in the $n = 50$ and $m_\ell = 0$ state of hydrogen. The figure shows the spatial distribution of the electric charge density under the influence of a static electric field along the positive z axis. The purple $k = 49$ state (a) is anti-aligned with the field whereas the orange $k = -49$ state (c) is aligned. The black $k = -1$ state (b) is nearly symmetric. These electric charge distributions can be compared with the Stark map for hydrogen shown in Fig. 2.1 to understand how the energy of each of these states behaves as a function of electric field strength.

The electric dipole moment scales with the principal number and leads to large energy shifts. Additionally, the eigenvectors of the hydrogen atom in a homogeneous field comprise a mixture of states with the same principal quantum number, which leads to no mixing between different n manifolds – as states approach each other, they go through exact crossings. This can be seen in Fig. 2.1 at around 6 V/cm. The point at which the states between adjacent manifolds overlap in energy is the Inglis-Teller limit. In hydrogen these wavefunctions of these states have no overlap so they undergo exact crossings.

This occurs because of the conservation of the Runge-Lenz vector. The symmetry is broken for non-hydrogenic atoms as the radial symmetry of the Kepler potential is broken by interactions with the core. We explore the effects of this in the next section, where we discuss the case of non-hydrogenic atoms.

2.3.2 Non-hydrogenic atoms in static electric fields

The effects of applied static electric fields differ for non-hydrogenic states with quantum defects. A comparison of the effects of an electric field on hydrogen and non-hydrogenic Rydberg states can be seen in the Stark maps shown in Fig. 2.1.

The lowest ℓ states in helium have lower energy and are detached from the other states in the manifold due to their non-zero quantum defects. Additionally, non-hydrogenic states display a quadratic induced dipole due to being separated from the manifold of Rydberg-Stark states. The eigenstates at zero field no longer remain eigenstates as the field strength increases. This results in the electron cloud density changing as a function of electric field and becoming more polarized at high field strengths.

At higher fields, the core interactions lead to avoided crossings where states from adjacent manifolds are no longer uncoupled. The field value for which the outermost Stark states from two consecutive n-manifolds cross is called the Inglis-Teller limit. The Inglis-Teller field is given by $F_{\mathrm{IT}} = \frac{F_0}{3n^5}$, where $F_0 = \frac{2hcR}{ea_0}$. The quantum defects have broken a symmetry isolating the n manifolds. The overlap between the states wavefunctions becomes non-zero and they undergo avoided crossings. This is shown in Figure 2.1 where the coloured lines that follow the adiabatic energy of the $\ell = 0$ and $\ell = 49$ states no longer pass through the states from the adjacent manifold.

The difference in the electron charge density for similar states can be seen by comparing Fig. 2.2 with Fig. 2.3. Due to the $\ell = 49$ and $\ell = 25$ states being in the manifold of states with very small quantum defects, their behaviour is very nearly hydrogenic. Comparing the electric field distributions of these states in the external field with the equivalent states for hydrogen (see Figure 2.2) shows this similarity.

The $\ell = 0$ state has very different behaviour than the equivalent $k = -49$ state in hydrogen. It exhibits a quadratic Stark shift rather than a linear shift and its electric charge density becomes increasingly polarized as the field strength increases. In zero electric field the

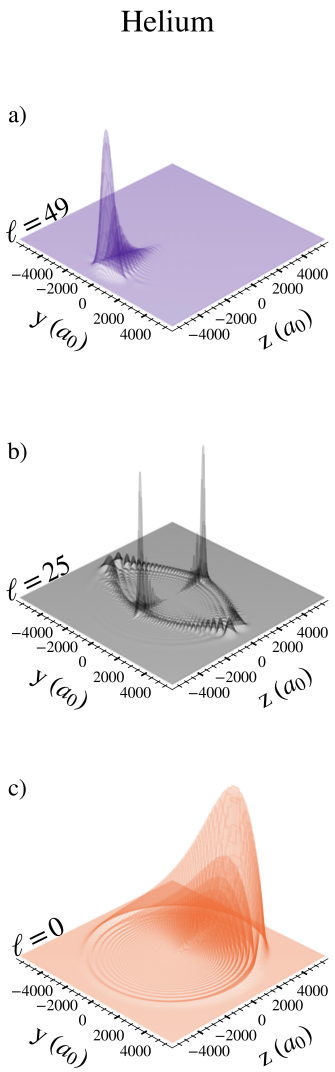

Figure 2.3: Electric charge density in the $(\hat{y}, \hat{z})$ plane for the valence electron in the $n = 50$ and $m_\ell = 0$ state of helium. The figure shows the spatial distribution of the electric charge density under the influence of a static electric field $F = 1$ V/cm along the positive z axis. Comparing the electric field distributions of each state with its equivalent state in Fig. 2.2 highlights the effect of the quantum defects on the states. For $\ell = 49$ (a) and $\ell = 25$ (b) with small quantum defects, the electron cloud density remains similar to the hydrogenic case. However, for the $\ell = 0$ state with significant defect, the state has an induced quadratic Stark shift and the electron cloud density is highly dependent on the field strength.

state has no static electric dipole. Instead it acquires a dipole due to the electric field. The scaling of the polarizability can be shown using perturbation theory. The second-order energy shift caused by the coupling to the nearest state in energy $E_{n,\ell}$ with an allowed transition ($\ell' = \ell \pm 1$) is given by

$$\Delta E \propto \frac{\langle n, \ell | \, er \, | n', \ell' \rangle \, \langle n', \ell' | \, er \, | n, \ell \rangle}{E_{n,\ell} - E_{n',\ell'}}. \tag{2.12}$$

The dipole moment terms $\langle n, \ell | \, er \, | n', \ell' \rangle$ are proportional to n^2 and the energy difference between the states $E_{n,\ell} - E_{n',\ell'}$ is proportional to n^{-3} [14]. This leads to polarizabilities that scale as n^7.

The low-ℓ states also have the desirable properties of being isolated in energy from other states in the manifold due to their unique quantum defects. This makes them less susceptible to non-adiabatic losses in rapidly switched fields and makes them more robust to black-body transitions. This is because they have fewer transitions available at the energy of background photons.

2.4 Rydberg states in oscillating electric fields

The Hamiltonian describing a Rydberg atom in the presence of an oscillating electric field can be expressed as

$$H = H_{ind} + H_{\mu}(t), \tag{2.13}$$

where $H_{ind} = H_0 + H_{int}$ is the total Hamiltonian consisting of the bare Hamiltonian H_0 and any static interaction terms. The time-dependent interaction Hamiltonian, $H_{\mu}(t) = F_{osc} \cos(\omega_{\mu} t)\hat{z}$, represents the interaction with an oscillating field.

As opposed to the static case, when the applied field is oscillating, the shifts in the atomic energy structure are more complicated. The effect produced by the oscillation on the energy level spectrum depends on how close to resonance the field is with a transition between states, and on the strength of the field itself.

For a state without near-resonant transitions at the driving frequency, the effect produced is similar to the static case. These shifts in the energy level are called dynamic/AC Stark shifts. This does not induce transitions between states and results in a perturbation to the energy level.

Whether the frequency of the driving field is larger or smaller than a transition determines if this induces a positive or negative energy shift. When the frequency of the oscillating field is greater than the nearest transition $\omega > \omega_0$, the field is said to be blue-shifted and experiences a positive shift to its energy [14]. The alternative is a red-shifted state when $\omega < \omega_0$.

The tunability of these shifts make AC Stark shifts useful tools to modify the energy levels of atoms in useful ways, such as nulling the polarizability of a transition to reduce the effects of stray fields [44].

On resonance, the effect is much more extreme and can cause the resonant energy level to split into two new levels that are separated

by the strength of the driving field. This phenomenon is known as the Autler-Townes effect [45]. The physics of the on-resonant case is dealt with in detail in Chapter 4.

2.4.1 The Floquet formalism

One approach to solve the time dependence of the problem is to use Floquet's theorem. Floquet's theorem states that for a Hamiltonian that is periodic in time with period T, $H(t) = H(t+T)$, the eigenfunctions, Ψ_κ, need not be periodic. However, they are of the form, $\Psi_\kappa(t) = e^{i\epsilon_\kappa t/\hbar}\Phi_\kappa(t)$. Here, $\Phi_\kappa(t)$ is the Floquet mode, a time-dependent superposition of the field-free basis states, and has period T, $\Phi_\kappa(t+T) = \Phi_\kappa(t)$.

Each Floquet mode has an associated time-independent quasienergy, ϵ_κ, which is not uniquely defined, but has values $\epsilon_{\kappa,q} = \epsilon_\kappa \pm q\hbar\omega_d$, where q is an integer and $\omega_d = 2\pi\nu_d = 2\pi/T$. In this context, the value of q represents the number of photons contributing to the mode [46].

Using this method, a time-periodic Hamiltonian can be rewritten in terms of the quasienergies and Floquet modes, i.e., $\mathcal{H}(t)\Phi_\kappa(t) = \epsilon_\kappa\Phi_\kappa(t)$. The solutions are the eigenvalues of the matrix of the Floquet Hamiltonian operator $\mathcal{H}(t) = H(t) - i\hbar\partial_t$. We will use the convention that calligraphic $\mathcal{H}$ represents a matrix in the time-independent Floquet basis.

The quasienergies ϵ_κ are not time-dependent, which means that solving the Floquet Hamiltonian at a given time gives the quasienergies at all times, making the problem time-independent.

The price to pay for losing this time dependence is that the once finite-dimensional state space becomes infinite-dimensional. Although the matrix $\mathcal{H}$ is infinite-dimensional, in practice, multiphoton interactions beyond a certain photon number do not influence the dynamics significantly, so the matrix can be truncated without loss of accuracy.

To transform from H to $\mathcal{H}$, the photon number states must be accounted for using an additional quantum number q, where $-\infty < q < \infty$.

$$\mathcal{H}_\mathrm{F} = \begin{pmatrix} \ddots & & & & \\ & H_{ind} - \hbar\omega\hat{I} & \hat{H}_\mu & 0 & \\ & \hat{H}_\mu^\dagger & H_{ind} & \hat{H}_\mu & \\ & 0 & \hat{H}_\mu^\dagger & H_{ind} + \hbar\omega\hat{I} & \\ & & & & \ddots \end{pmatrix} \tag{2.14}$$

where $\hat{H}_0$ corresponds to the time-independent Hamiltonian, and $\hat{V}_\omega$ is the time-periodic component.

The matrices on the main diagonal are modified at each q level with a diagonal $q\hbar\omega\hat{I}$ matrix. The larger state-space introduces an additional Floquet sideband eigenstate at each value of q separated in energy by $\hbar\omega$. Intuitively this can be seen as a dressed atom state space where the energy of both the atom and electric field are accounted for.

2.5 Numerical calculations of Rydberg state properties

In this section, the numerical methods employed to compute properties of triplet Rydberg states of helium in static and oscillating electric fields are explained. The code written for this purpose is archived on GitHub at https://github.com/jdrtommey/rydprops.

The general form of the Hamiltonian to be solved numerically for experiments performed in this thesis is

$$H = H_0 + H_s + H_\mu(t), \tag{2.15}$$

where H_0 is the field-free Hamiltonian, $\hat{H}_s = \hat{H}_\perp + \hat{H}_\parallel = F_x\hat{x} + F_z\hat{z}$ represents the static electric field in both a parallel and perpendicular direction, and $\hat{H}_\mu(t) = F_{osc}\cos(\omega_\mu t)\hat{z}$ is a linearly polarized microwave field.

The Hamiltonian is written in the $|n, \ell, m_\ell\rangle$ basis. In the presence of a non-zero H_μ, this basis is expanded to include the Floquet sidebands and becomes $|n, \ell, m_\ell, q\rangle$.

In general, the process to construct and diagonalize these Hamiltonians will be described for the $|n, \ell, m_\ell, q\rangle$ basis. However, when $F_{osc} = 0$ V/cm, only the $q = 0$ state is required, and the problem reduces to the single $q = 0$ block of the full Floquet Hamiltonian. The block form of the diagonal matrix is shown in Eq. 2.16.

$$\mathcal{H}_F = \begin{pmatrix} \ddots & \vdots & \vdots & \vdots & \vdots & \vdots & \iddots \\ \dots & \hat{H}_{ind} - 2\hbar\omega\hat{I} & \hat{H}_\mu & 0 & 0 & 0 & \dots \\ \dots & \hat{H}_\mu^\dagger & \hat{H}_{ind} - \hbar\omega\hat{I} & \hat{H}_\mu & 0 & 0 & \dots \\ \dots & 0 & \hat{H}_\mu^\dagger & \hat{H}_{ind} & \hat{H}_\mu & 0 & \dots \\ \dots & 0 & 0 & \hat{H}_\mu^\dagger & \hat{H}_{ind} + \hbar\omega\hat{I} & \hat{H}_\mu & \dots \\ \dots & 0 & 0 & 0 & \hat{H}_\mu^\dagger & \hat{H}_{ind} + 2\hbar\omega\hat{I} & \dots \\ \iddots & \vdots & \vdots & \vdots & \vdots & \vdots & \ddots \end{pmatrix} \begin{matrix} q = \dots \\ q = -2 \\ q = -1 \\ q = 0 \\ q = +1 \\ q = +2 \\ q = \dots \end{matrix} \tag{2.16}$$

Here, the sub-matrices illustrated by coloured blocks are in the $|n, \ell, m_\ell\rangle$ basis. The states are indexed by i and belong to state space S of size $|S|$, which is the sum over all included states.

To extend this space into the $|n, \ell, m_\ell, q\rangle$ basis, where $q \in \{-q_{\text{bands}}, \dots, q_{\text{bands}}\}$ denotes the number of additional bands, each state is mapped to the extended space by assigning a new index a' as

$$a' = a + (q + q_{\text{bands}})|S|. \tag{2.17}$$

This formula shifts the original index a by multiples of $|S|$ for each q-band, ensuring a unique mapping of states from the original space S to the extended space. In this way, the index i' of any state in the $|n, \ell, m_\ell, q\rangle$ basis can be identified.

The orange block matrices represent terms of the Hamiltonian for the time-independent interactions $H_{ind} = H_0 + H_s$. These matrices represent interactions within a single q level, thus elements in these blocks contain a Kronecker delta $\delta_{q',q}$ in the full representation.

The purple blocks represent the interactions with the microwave field. These elements couple states that are in adjacent q bands and therefore will contain the delta function $\delta_{q',q\pm1}$.

Since $\mathcal{H}_F$ is infinite-dimensional, a truncation must be performed at a reasonable number of q_{bands} sidebands. In general, the approach taken was to iteratively increase the number of sidebands q_{bands} until convergence in the energy eigenstates of interest was achieved.

The size of these Rydberg state matrices can quickly become very large. A space S consisting of all ℓ and m_ℓ up to a given n value contains

$$|S| = \sum_{\ell=0}^{n-1}(2\ell+1) = n^2 \tag{2.18}$$

states. In [47], the eigenenergies of the $n = 72$ circular Rydberg state ($|C_n\rangle = |n, n-1, n-1\rangle$) are computed, requiring 5 manifolds and a state space of $|S| = 31,555$. Diagonalizing such matrices is expensive, and in the case of the referenced study, retrieving the eigenvectors proved intractable when diagonalizing the dense matrix.

Optimizations can be performed using sparse matrices to increase the size of the state space $|S|$ being explored and to improve the speed at which the computations can be performed. Some such optimizations are discussed in Section 2.5.3.

2.5.1 Calculating the matrix elements

From inspecting Equation 2.16, each of the orange and purple block matrices needs only to be computed once, so that a large amount of computational complexity can be avoided. The components of each matrix can be solved in the $|n, \ell, m_\ell\rangle$ basis, and if $F_{osc} \neq 0$ and therefore $q_{\text{bands}} \neq 0$, they can be mapped to the $|n, \ell, m_\ell, q\rangle$ basis, by duplicating along the block off-diagonals following $\delta_{qq'}$ for time-independent elements.

The field-free Hamiltonian is diagonal with matrix elements

$$\langle n, \ell, m_\ell| \hat{H}_0 |n, \ell, m_\ell\rangle = \frac{-R_{\text{He}}}{(n-\delta_{n,\ell})^2}, \tag{2.19}$$

which follows directly from Equation 2.4.

The remaining time-independent terms due to the Stark shifts $\hat{H}_s = F_x\hat{x} + F_z\hat{z}$ can be solved by separating the integrals into radial and angular components. The interaction with the electric field in either direction is given by the matrix elements $\langle n', \ell', m'_\ell| z |n, \ell, m_\ell\rangle$ and $\langle n', \ell', m'_\ell| x |n, \ell, m_\ell\rangle$ respectively.

These terms are separated into radial and angular components using $z = r\cos\theta$ and $x = r\sin\theta\cos\phi$, resulting in matrix elements

$$\begin{aligned}\langle n', \ell', m'_\ell, q'| \mathcal{H}_{\text{ind}} |n, \ell, m_\ell, q\rangle = {} & eF_z \langle n', \ell'| r |n, \ell\rangle \langle \ell', m'_\ell| \cos\theta |\ell, m_\ell\rangle \delta_{q,q'}\delta_{m'_\ell,m_\ell} \\ & + eF_x \langle n', \ell'| r |n, \ell\rangle \langle \ell', m'_\ell| \sin\theta\cos\phi |\ell, m_\ell\rangle \delta_{q,q'}.\end{aligned} \tag{2.20}$$

The radial integrals are solved numerically using the Numerov method. The angular components can be computed analytically [48].

Accordingly, the total Hilbert space for the atom in the presence of the field is spanned by basis states of the form $|n, \ell, m_\ell, q\rangle$. In this Floquet basis, the diagonal elements of the resulting matrix $\mathcal{H}_0$ for the high Rydberg states in helium are

$$\langle n, \ell, m_\ell, q| \mathcal{H}_0 |n, \ell, m_\ell, q\rangle = -\frac{R_{\mathrm{He}} hc}{(n - \delta_{n,\ell})^2} + qh\nu_d, \tag{2.21}$$

where an additional energy term is present due to the number of photons of energy $h\nu_d$ in the mode.

H_μ is the interaction Hamiltonian with elements,

$$H_\mu = \frac{F_{osc}}{2} \langle n', \ell', m'_\ell| z |n, \ell, m_\ell\rangle .$$

The factor of $\frac{F_{osc}}{2}$ arises due to time-averaging of the field strength. It can also be seen that these matrix elements are the same as for the static electric field $H_\parallel$. Using Equation 2.17 and standard matrix slicing operations, the terms in the matrix $\mathcal{H}_\mu$ can be constructed without recomputing this interaction Hamiltonian.

2.5.2 Calculating transition strengths and linewidths

The transition strength may be calculated by taking the overlap between the ground state and an eigenstate of the total Hamiltonian. Written in the $|n, \ell, m_\ell, q\rangle$ basis, each eigenstate of H_{total} is a sum over the basis states:

$$|\psi\rangle = \sum_{n,\ell,m_\ell,q} c_{n,\ell,m_\ell,q} |n, \ell, m_\ell, q\rangle , \tag{2.22}$$

where $c_{n,\ell,m_\ell,q}$ is the coefficient (or amplitude) for the state $|n, \ell, m_\ell, q\rangle$.

The transition dipole moment $\mu_{fg} = e \langle g| r |\psi\rangle$ between $|\psi\rangle$ and a ground state is given by

$$\mu_{fg} = \sum_{n,\ell,m_\ell} c_{n_g,\ell_g,m_{\ell g},0} \langle g, 0|\mu|n_f, \ell_f, m_{\ell f}, 0\rangle \delta_{q_f,q_g=0}. \tag{2.23}$$

Only the $q = 0$ states are included in this calculation and $|g, 0\rangle$ is the groundstate . For the experiments performed in this thesis, the ground state is the 2p state. The transition dipole moment between the groundstate and any excited Rydberg state is therefore proportional to the amount of nS and nD character in each state.

The result of combining the eigenvalues for the states with the relative coupling strengths is a stick spectrum from the ground state via laser excitation. Plotting the relative magnitude of the transition dipole moment from the ground state for each state as a function of energy gives the excitation spectra. These simulations do not directly estimate the line-width of each transitions. This therefore results in a stick spectrum where each transition is infinitely thin.

In order to reproduce experimentally observed spectra, it is necessary to introduce an energy linewidth to each transition. This is achieved by convolving the stick spectrum with a Gaussian function to match the broadened lines seen in experiments. In the experiments

performed in this thesis, the linewidths of transitions are generally limited by the interaction time of the supersonic beam with the excitation lasers, and are around 30–45 MHz [49].

2.5.3 Efficiently calculating the eigenspectra

We have seen that the state space S can become very large. This can make retrieving the eigenvectors for all states in S very expensive. Additionally, only a small number of the states required in S are likely to be of experimental interest and within the frequency region accessible by the excitation laser.

Thus, a large number of the eigenvectors are made redundant. In order to diagonalize these matrices efficiently, sparse matrix techniques are used. This is efficient because very few of the states in the state space are directly coupled due to the selection rules of the interactions.

This can be seen using the example of a parallel electric interaction within a single n manifold. The selection rules $\Delta\ell = \pm 1$ and $\Delta m_\ell = 0$ apply, and within each ℓ manifold there are $2\ell + 1$ states. Each of these states only couples to a single state in an adjacent ℓ manifold, resulting in $2\ell + 1$ additional couplings.

The sum of all of these terms comes to $2\sum_{\ell=0}^{n-2}(2\ell+1) = 2(n-1)^2$, where the factor of 2 accounts for the transposed elements. This gives a percentage of non-zero elements in the matrix $H_\parallel$ of approximately

$$\text{Percentage of non-zero elements} = \frac{2(n-1)^2}{n^4} \times 100\%, \qquad (2.24)$$

checking this for $n = 50$ shows that only $\approx 0.08\%$ of the elements are non-zero for the $H_\parallel$ interaction matrix.

The calculations make use of the SciPy [50] wrapper around the ARPACK [51] routine. This routine allows for a subset of eigenvalues and eigenvectors to be found in the region of an estimated value.

As the field strength increases, states for which in zero field correspond to a basis state $|n, \ell, m_\ell\rangle_{\text{adi}}$ must be kept track of.

Computing the eigenenergy at each time-step would be computationally expensive. A solution is to instead precompute the eigenenergy for a range of electric fields and store these in a look-up table. This requires re-diagonalizing the Hamiltonian for a number of different field strengths. With increasing strength of external fields, the number of additional states which need to included in order to accurately compute the energy increases. All of the eigenenergies other than the state of interest are irrelevant in this case.

Additional tools were also written to adiabatically follow the state of interest as the strengths of external fields were increased. At each field-strength step, the eigenvalues and eigenvectors of the previous step are used as a starting point, to predict the eigenenergy at the next step of field strength. The eigenvalues are compared to ensure that the correct state is tracked, even through avoided crossings. This method ensures only a few eigenvalues and eigenvectors near the state of interest need to be calculated at each step.

3
Experimental methods

THE EXPERIMENTS performed in both parts of this thesis make use of pulsed supersonic beams of helium atoms. In this chapter we present the general experimental apparatus. A more detailed account of aspects of this experimental setup can be found in the Ph.D. thesis of Patrick Lancuba [52], who built the original apparatus.

3.1 Design of the apparatus

A schematic diagram of the experimental apparatus for the pulsed supersonic beams is shown in Figure 3.1.

A pulsed supersonic beam of helium atoms in the metastable $1s2s\,^3S_1$ level is generated in a dc electric discharge at the exit of a pulsed valve [53]. The beam, with a mean longitudinal speed of 2000 ± 50 m/s, passes through a skimmer with diameter of 2 mm before entering a region where an electric field is generated, to deflect and filter ions created in the discharge.

The atoms then enter a region defined by two copper electrodes, $P1$ and $P2$. These electrodes are rectangular plates measuring 100 mm in length and 70 mm in width. They can be aligned either parallel or at an angle to each other to produce homogeneous or inhomogeneous electric fields, respectively. The electrodes are mounted on insulating supports to allow for the application of voltages.

Then, within the region between the electrodes we photo-excite the Rydberg states. Two co-propagating UV and IR laser beams intersect the atomic beam. The UV laser is a frequency-doubled Toptica DL Pro laser, stabilised to $\lambda_{uv} = 388.975$ nm to drive the $1s2s\,^3S_1 \rightarrow 1s3p\,^3P_2$ transition. The UV laser power in the interaction region is approximately 8 mW. The IR laser is another Toptica DL Pro laser diode laser operating tunable frequency around 788 nm, with a power of approximately 1.5 W, which is necessary to saturate the transitions to Rydberg states.

Both lasers were stabilised via wavemeters. The IR laser is tuned in the region around 788 nm to drive $1s3p\,^3P_2 \rightarrow 1sns\,^3S_1/1snd\,^3D$ transitions, where n is the principal quantum number of the Rydberg state. Both laser beams are focused to a waist of approximately 100 μm at the interaction region. Following the Rydberg state photo-excitation experiments are performed by applying combinations of control pulses.

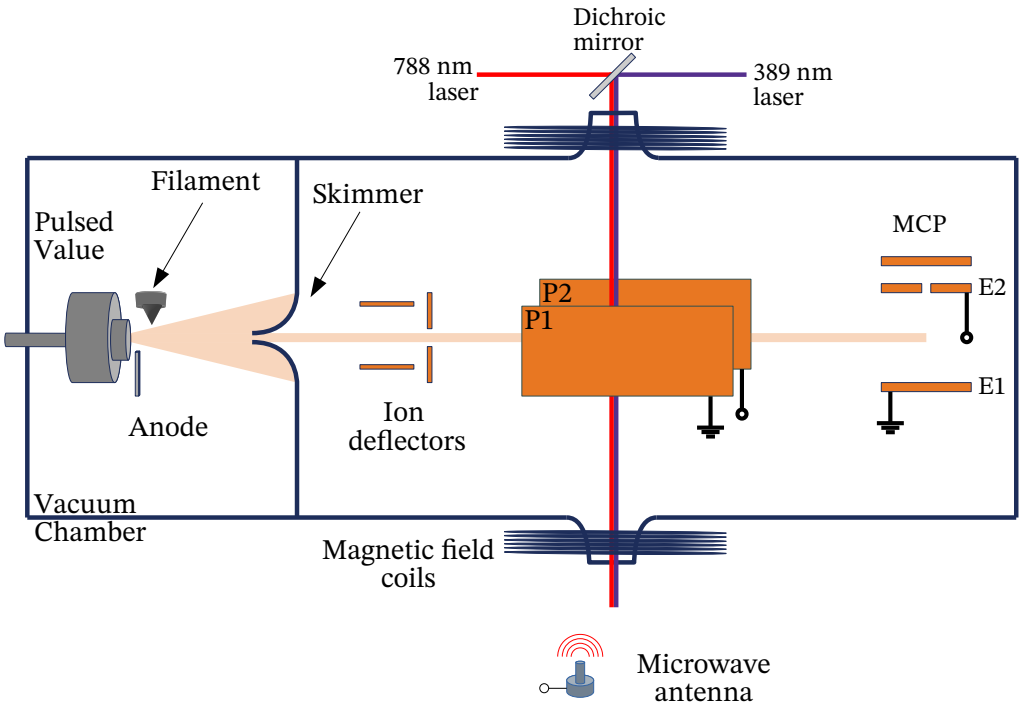

Figure 3.1: Schematic of the experimental apparatus used throughout this thesis with key sections labelled. A supersonic beam of metastable triplet Helium is created in a dc electric discharge at the exit of a pulsed valve. The atoms travel through a skimmer and ion deflector to collimate the beam. Excitation and manipulation of the Rydberg states is performed within the first pair of electrodes, referred to as $P1$ and $P2$. Within this region magnetic fields and microwave control pulses can be applied. State-selective electric field ionization is performed within the electrodes $E3$ and $E4$.

These can take the form of voltages applied across $P1$ and $P2$, microwave pulses applied either directly to the plates or via a microwave antenna. In this region, magnetic fields can be applied via current-carrying wires coiled around the vacuum chamber transverse to the beam direction.

After completion of the experimental scheme, the excited atoms travel from $P1$ to $P2$ and enter the detection region of the apparatus between the two parallel electrodes $E1$ and $E2$. When the atoms reach the detection region a pulsed voltage is applied between electrodes $E1$ and $E2$ to induce state-dependent ionization.

Electrode $E2$ has an aperture to allow the ions or electrons to pass through to the micro-channel plate (MCP) detector located behind it. The resulting electric field ionises the excited Rydberg atoms and accelerates them through an aperture in $E4$ to a micro-channel plate (MCP) detector.

3.2 Pulsed supersonic beams of helium

In the experiments pulsed supersonic beams of helium atoms with a repetition rate of 50 Hz were generated using an electromagnetic pulsed valve. The valve is operated at 50 Hz as a consequence of heating. In the limit where the mean free path of the atoms in the reservoir λ_0 is

much greater than the diameter of the reservoir opening D, the atoms collide more frequently.

These collisions lead to adiabatic cooling of all degrees of freedom, and the energy available to each atom is converted into kinetic energy in a directed flow [54], with the enthalpy mainly converted into a directed mass flow with large forward velocities and small velocity spreads. The translational temperature $T(L)$ as a function of the distance L from the exit of the valve can be expressed as [55]

$$T(L) = \frac{T_0}{1 + \frac{1}{2}(\gamma - 1)M(L)^2}, \tag{3.1}$$

where $M(L)$ is the Mach number and $\gamma = C_p/C_v$ is the ratio of the heat capacity at constant pressure to constant volume.

The Mach number takes the form,

$$M(L) = A\left(\frac{L}{D} - B\right)^{\gamma-1} - C\left(\frac{L}{D} - D\right)^{1-\gamma}, \tag{3.2}$$

where $A = 3.26$, $B = 0.075$, $C = 0.61$ and $\gamma = 5/3$ for a mono-atomic gas. Figure 3.2 shows the dependence of the Mach number M on the distance from the nozzle L.

The velocity distribution in the direction of propagation of the beam can be obtained as [55],

$$a' f_n(v) = N_n v^n e^{-(v-\bar{v}_z)^2/\xi}, \tag{3.3}$$

where $\xi = \sqrt{2k_bT(L)/m}$, N_n is a normalization factor, and the mean longitudinal velocity is given by $\bar{v}_z = M(L)\sqrt{\gamma k_b T(L)/m}$. This is shown in the inset of Figure 3.2.

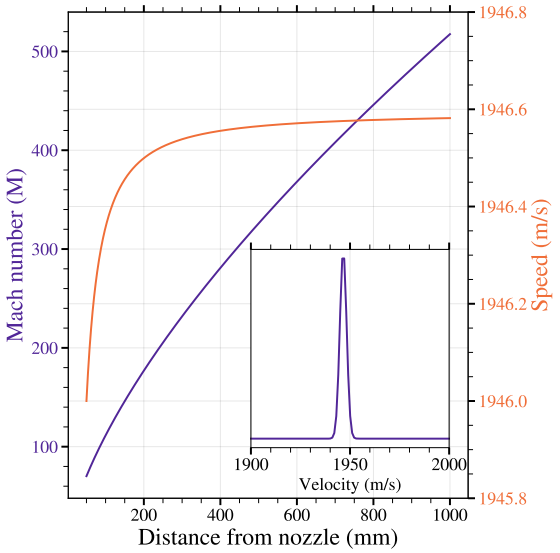

Figure 3.2: Parameters for the supersonic expansion in the experimental apparatus at temperature $T_0 = 365$ K. Inset: The velocity distribution at 600 mm from the nozzle.

With these equations, the velocity distribution in the experiments can be calculated. The experiments carried out in this thesis use a valve with a temperature $T_0 \approx 365$ K, with an exit aperture of $D = 0.5$ mm and a skimmer placed at a distance $L \approx 5$ cm. The skimmer has an opening diameter of 2 mm and collimates the supersonic beam.

This results in atomic beams with longitudinal velocity distributions of $V_z \approx 2000 \pm 50$ m/s. The velocity could be reduced by cooling the valve. This velocity distribution agrees with that observed experimentally using time-of-flight measurements in the apparatus [49].

3.3 Excitation to Rydberg States

In order to prepare Rydberg states via direct laser excitation, the helium atoms must first be excited to the metastable $1s2s\,^3S_1$ state. This is achieved via an electric discharge at the exit of the valve [53]. Electric discharge is generated by applying a dc voltage of +240 V to a metal tip located 1 mm away from the exit of the pulsed valve which is grounded. The tip is located 1 mm ahead of the valve in the longitudinal dimension and around 0.5 mm off the beam axis.

The metastable $1s2s\,^3S_1$ level has a lifetime of ≈ 8000 seconds, much longer than the ≈ 100 μs duration of the experiments so it can be considered as a effective ground state. The large electric fields required for the discharge can heat the beam and reduce the shot-to-shot stability. To allow for the discharge to be generated at low electric fields it is seeded with electrons from a heated tungsten filament.

The tungsten filament is heated by applying a current of 2.6 A, this causes the filament to emit electrons via thermionic emission. The emitted electrons help initiate the discharge by providing seed electrons for ionisation of the helium gas. The recombination of the generated plasma allows the metastable $1s2s\,^3S_1$ level to be populated.

Due to the selection rules of single-photon electric dipole transitions, only states with low angular momentum can be reached by direct excitation as $\ell' = \ell \pm 1$. The excitation scheme used in the experiments performed in this work with helium is shown in Figure 3.3. A two-colour and two-photon scheme is used to reach the Rydberg states.

In this scheme, atoms that start in the metastable $1s2s\,^3S_1$ level are excited to the $1s3p\,^3P_2$ state using a UV laser stabilised to $\lambda_{uv} = 388.975$ nm. A tunable IR laser around $\lambda \approx 788$ nm completes the scheme by exciting to $\ell' = 0, 2$ levels, $1s3p\,^3P_2 \rightarrow 1sns\,^3S_1/1snd\,^3D$.

The Stark shift, which was introduced in Sec. 2.3, is useful for exciting a wider range of Rydberg states by mixing the field-free eigenstates. The excitation scheme above can excite any Rydberg-Stark state which has nS or nD character.

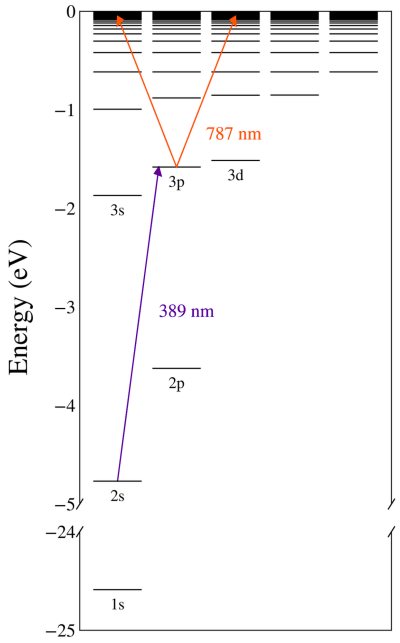

Figure 3.3: Excitation scheme from the metastable triplet helium to Rydberg states via a 2-photon UV/IR transition via the intermediate 3p state.

3.4 Manipulation of Rydberg States

The properties of Rydberg states can be finely tuned and controlled using external fields. In our experiments, we manipulate the Rydberg states within electrics P1 and P2 through the application of magnetic and microwave fields.

In our setup, the magnetic field is generated using circular coils placed on the outside of the vacuum chamber. The circular coils are mounted externally to the vacuum chamber, with their axes aligned parallel to the direction of the laser beams used for excitation.

We calibrated the system using a Hall probe, to quantify the magnetic field strength along the beam axis in the excitation region between P1 and P2. The magnetic field was measured to be $B_x = B_0 + \beta I$, where $B_0 = -0.25 \pm 0.25\,\mathrm{G}$ is the stray magnetic field, I is the applied current in the coils, and $\beta = -1.31 \pm 0.05\,\mathrm{G/A}$ is the proportionality factor.

Microwave fields are utilized to couple Rydberg states within the atom, enabling both the exploration of energy level structures in the presence of external microwave fields, and for coherent control in interferometry schemes. Two different techniques were used to apply microwave pulses.

The first used in the experiments in Part 1 employed capacitative coupling of the microwave generator directly to electrode P1. This setup generated a microwave field that is polarised along the direction of the plates. The strength and frequency of the microwave field can be precisely controlled by adjusting the voltage applied to the plates and tuning the microwave source, respectively.

In the interferometry experiments in Part 2, a horn antenna located outside the vacuum chamber was used to generate coherent pulses π and $\pi/2$. Again, the antenna was directed to generate microwaves polarised in the vertical direction as defined by P1 and P2.

3.5 Field ionisation of Rydberg states

Static electric fields can be used to alter the energy of Rydberg states and manipulate their properties. They also allow for a state-selective detection of individual Rydberg state populations, that is vital for the experiments described. In this detection process, if a large enough static electric field is applied, the valence electron is stripped away from the atom, where the applied field depends on the state.

It is possible to determine the internal state of the atom by applying an electric field between the ionisation threshold of the two states of interest and then collecting the ionised electrons. An intuitive picture of how the Rydberg state ionises can be made by observing the potential in which a valence electron resides when the combination of the central Coulomb potential and the external electric field are applied. This potential is shown in Figure 3.4.

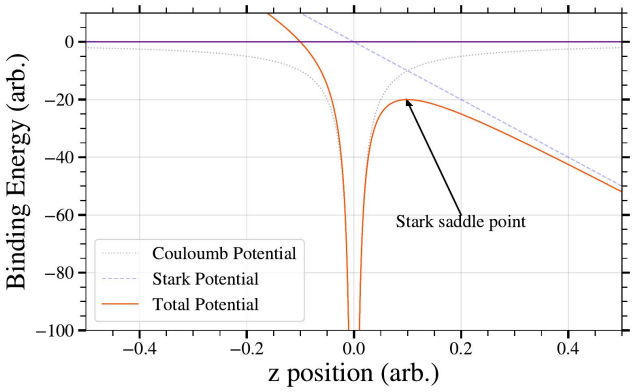

Figure 3.4: A schematic showing the combined potential energy of a Coulomb and linear potential. In grey, the original symmetric potential landscape and the applied Stark potential is shown, the addition of the field results in the combined potential in red. The saddle point shows the classical energy at which a state would ionize.

The asymmetry of this potential means the electron can only tunnel out of the potential barrier on one side of the atom. For this tunnelling to occur, the electron charge density must be localised near the saddle point of the potential. The ℓ-mixed Rydberg Stark states with negative Stark shifts lower their energy in the electric field, and have a more concentrated charge distribution near the saddle point.

On the other hand, the ℓ-mixed Rydberg-Stark states with positive Stark shifts have the opposite distribution of charge. The charge distribution is bunched up on the high potential side of the atom. With lower electron charge density near the saddle-point, these states will ionise in higher fields. This leads to varying rates of tunnel ionisation, that depends on internal details of the state.

In the classical picture, once the energy of the state crosses the saddle point, it will ionise. For a hydrogenic Rydberg-Stark state with a negative Stark shift, the field at which this occurs while accounting for its Stark shift is,

$$F_{\text{ion}} = \frac{2hcR}{ea_0 9n^4}. \tag{3.4}$$

On the other hand, in the quantum picture, there is no definite field in which a state is bound. This makes it possible for states whose energy is lower than the classical turning point to tunnel ionise. The classical equation still gives a good estimate of the field at which the outermost high-field-seeking Rydberg-Stark states will tunnel, this comes out to be at a rate of 10^8 s^{-1}.

The states on the other side of the manifold, the low-field-seeking states, will experience a similar tunnelling rate at approximately twice the field in Eq. 3.4. This equation gives a good estimate for the Rydberg Stark states ionisation in hydrogen.

The dynamics are more complicated in non-hydrogenic atoms due to the avoided crossings that start at the Inglis-Teller field. Even so, this classical approach gives a good enough indication of the magnitude of fields necessary and the concept remains the same. If the applied electric field is increased slowly, different states still show this ionisation for the different fields and therefore for non-hydrogenic atoms, the state-selective detection method is still valid.

3.5.1 Performing the state-selective measurement

Once ionised, the charged particles can be accelerated towards a microchannel plate detector (MCP). The MCP detector used in these experiments comprises an array of 106 miniature electron multiplier tubes organized in a 'chevron' configuration [56]. Each tube has a 10 μm diameter and 60:1 length-to-diameter ratio, with precise spacing and an applied voltage of +1 kV. This setup enhances electron multiplication, enabling significant signal amplification, and allows detection of the electrons and ions of specific Rydberg states by adjusting electrical potentials across the MCP plates [57].

The exact parameters depend on the Rydberg states being observed. For example, a potential difference of 295 V was applied between E1 and E2 to detect the $n = 105$ Rydberg states in the experiments of

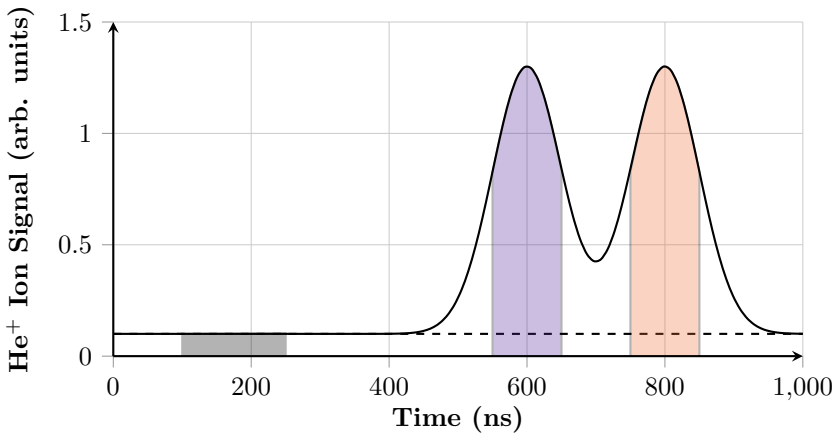

Figure 3.5: Time-of-flight signal of He^+ ions detected by the MCP. The ionising electric field is ramped over time, resulting in a state-dependent collection time. The total signal from a given state can be integrated from an oscilloscope trace. The trace can either be from a single experimental shot or averaged over a number of experimental runs. In this example, two integration windows (purple and orange) are placed in the time-windows in which two different Rydberg states are expected to be received. An additional background window (black) is recorded to be subtracted from these windows.

Chapter 4. A much larger potential difference of 2.4 kV was used to detector $n = 55/56$ states in the experiments performed in Chapter 6 and Chapter 7.

The voltage is applied to E1 with a rise time of approximately 800 ns. The timing of the voltage pulse is synchronised with the arrival of the Rydberg atoms in the detection region, typically occurring 70 μs after the excitation lasers.

By increasing the amplitude of the electric field, we selectively ionise Rydberg states with different principal quantum numbers n as a function of time. The ions or electrons produced by field ionisation are accelerated toward the MCP detector, where they multiples before hitting an anode and producing a measurable signal .

Figure 3.5 shows an idealised oscilloscope trace that demonstrates the state-selective measurement of Rydberg states. It represents a time-of-flight distribution of He+ ions after pulsed electric field ionisation. Integration windows are placed in time windows, where a state or multiple states ionise.

The raw data can correspond to either a single or multiple oscilloscope traces. Using a LabView program, described in Ref [52], these windows can be set and the raw data integrated. To perform this integration of the signal, multiple time windows are integrated.

The black window in Figure 3.5 is a background measurement in a region where no Rydberg ions are detected. After subtracting this background from the recorded oscilloscope trace, the signal within the other windows can be integrated.

This chapter summarises the techniques used for the creation, manipulation, and measurement of Rydberg states for the experiments performed in both parts of this thesis. These experiments deviate where the microwave pulses are applied, and the techniques used here. In the later chapters we will go on to describe these.

Part I

Ultra-strong driving of high-n Rydberg states

4
Ultra-strong driving of high-n Rydberg states

THIS CHAPTER describes experiments observing coherent Rydberg atom microwave field interactions in the ultra-strong driving regime. The resulting experimental data are in excellent quantitative agreement with the results of numerical calculations of the energy level structure, and the spectral intensities for the atom in a microwave field. These calculations make use of Floquet methods (Section 2.4.1), and we compare this approach with simpler models that use the two-level and rotating-wave approximations.

A two-level atom under the influence of a resonant or near resonant oscillating electric field is a useful starting model to understand the dynamics of atoms driven by oscillating electric fields. The solution to the resulting time-dependent hamiltonian can be simplified under certain conditions, to provide simpler models to describe the effects.

In this chapter, we solve for this problem, and the implications for the population dynamics and energy level spectrum will be discussed. These calculations are performed both with and without (in other words, going beyond) a simplifying assumption called the rotating wave approximation (RWA). We introduce the RWA and its connection to, and representation in, the Floquet formalism will be made.

This work is original and has been published in [58]. The contents of this section have been adapted and extended from this publication.

4.1 A two level atom in a near-resonant field

The time-dependent Hamiltonian for a two-level atom driven by a linearly polarised electric field is composed of two parts given,

$$H(t) = H_0 + H_{\text{int}}(t). \tag{4.1}$$

The free Hamiltonian for the two level system H_0 can be written in terms of the Pauli-z σ_z matrix as,

$$H_0 = \frac{\hbar\omega_0}{2}\sigma_z. \tag{4.2}$$

The energy difference between the two states is $\hbar\omega_0$, and we suggestively label the two states as $|g\rangle$ and $|e\rangle$. The interaction Hamiltonian $H_{\text{int}}(t)$ is the transition dipole between the two states,

$$H_{\text{int}} = -d \cdot E(t), \tag{4.3}$$

where the electric field is monochromatic and expressed as $E(t) = F_{\text{osc}} \cos(\omega t)$. The dipole operator is given by $d = ez$. For simplicity both the dipole and electric field can both be assumed to be polarized along the $\hat{z}$ axis.

The dipole operator can cause transitions between the two states and can be represented by raising and lowering operators $\sigma_{\pm}$ defined as $\sigma_+ = |e\rangle\langle g|$ and $\sigma_- = |g\rangle\langle e|$ as,

$$H_{\text{int}}(t) = \hbar\Omega_0(\sigma_+ + \sigma_-)\cos(\omega t), \tag{4.4}$$

where $\Omega_0 = \frac{-d \cdot F_{\text{osc}}}{2\hbar}$ is the Rabi frequency for the transition and ω is the driving frequency.

4.1.1 Dynamics of a driven two level system in the rotating wave approximation

The time evolution follows how the population dynamics as a function of time are affected by the ratio of Rabi frequency Ω_0 to transition frequency ω_0. This is numerically integrated and the plot is shown in Figure 4.1 for $\Omega_0 = A\omega_0$, where $A = 0.01, 0.1, 1.0$.

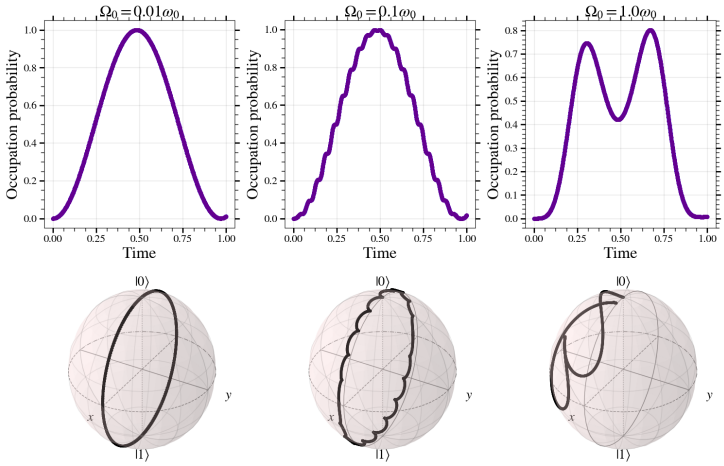

Figure 4.1: Time evolution of a two level atom in a resonant electric field for an initial state $|\psi(t=0)\rangle = |0\rangle$. Shown for three values of coupling strength Ω_0 at different percentages of the transition frequency ω_0. The time is normalised for a full oscillation between $|0\rangle$ and $|1\rangle$. In the case where $\Omega_0 = 0.01\omega_0$ the dynamics are a smooth oscillation between the two states. This corresponds to the regime in which the rotating wave approximation can be applied without loss of accuracy in the dynamics. In the other two cases corrections due the neglected terms in the RWA start to impact the dynamics.

The three plots show the time evolution of a state initialised as $\psi(0) = |0\rangle$. The time evolutions are normalised to the time it takes to complete a full oscillation from $|0\rangle \to |1\rangle \to |0\rangle$. This amount of time is related to the Rabi frequency, $T = \frac{2\pi}{\Omega_0}$.

When the Rabi frequency is of the same order of magnitude as the transition $\Omega_0 \approx \omega_0$, the evolution on the Bloch sphere shows oscillations about both the $\hat{z}$ and $\hat{y}$ axes. With the strength of the oscillation about $\hat{z}$ becoming more influential as the strength of Ω_0 increases.

In the case where $\Omega_0 \ll \omega_0$, here this occurs where $A = 0.01$, the influence of the oscillations about $\hat{z}$ is diminished. This leads to a simpler dynamics being observed, a pure oscillation driving population transfer between the two basis states. In this regime the rotating wave approximation (RWA) applies, and Figure 4.1 provides an intuition of how this assumption manifests.

The standard approach for applying the RWA to Equation 4.4 is frame rotating at the transition frequency ω_0, via the unitary $U(t) =$

$\exp\{iH_0t/\hbar\} = \exp\{i\frac{\omega_0}{2}\sigma_z t\}$ [59]. In doing so the interaction Hamiltonian is transformed as,

$$H_{\text{int}'} = \frac{\hbar\Omega_0}{2}(\sigma_+ e^{i(\omega_0+\omega)t} + \sigma_- e^{-i(\omega_0+\omega)t} + \sigma_+ e^{i(\omega_0-\omega)t} + \sigma_- e^{-i(\omega_0-\omega)t}) \tag{4.5}$$

where the identity $\cos(\omega t) = \frac{1}{2}\left(e^{i\omega t} + e^{-i\omega t}\right)$ has been applied. The terms

$$\sigma_+ e^{i(\omega_0+\omega)t} \quad \text{and} \quad \sigma_- e^{-i(\omega_0+\omega)t}$$

are fast oscillating terms (counter-rotating terms).

We can argue that since $\omega_0+\omega$ is much larger than the characteristic time scale of the system, these terms oscillate very quickly and average out to zero over time. Meanwhile, the terms,

$$\sigma_+ e^{i(\omega_0-\omega)t} \quad \text{and} \quad \sigma_- e^{-i(\omega_0-\omega)t}$$

are slow oscillating (co-rotating terms), because $\omega_0 - \omega$ is small when ω is close to ω_0 (near resonance). Thus, the RWA approximation amounts to keeping just these co-rotating terms, resulting in the Hamiltonian,

$$H_{\text{int}}^{\text{RWA}} = \frac{\hbar\Omega_0}{2}(\sigma_+ e^{i(\omega_0-\omega)t} \quad + \sigma_- e^{-i(\omega_0-\omega)t}). \tag{4.6}$$

In this chapter we investigate the implications of keeping both the full and approximated Hamiltonians on the energy-level spectrum of the driven atom.

4.1.2 Autler-Townes splitting and Bloch-Siegert shifts

In the Floquet picture the time-dependent Hamiltonian Eq. 4.1 is converted into an infinite dimensional Hamiltonian via methods detailed in Sec. 2.4.1. This produces the distribution of eigenstates shown in Fig. 4.2, where the different side-bands, q, are plotted along the x-axis.

The Hamiltonian has couplings between states that differ in side-band order by one. This leads to any single basis state being coupled to an infinite number of states in the non-RWA system. The problem may be simplified using perturbation theory under the assumption that only coupling to the state nearest in energy is important. The coupling which remains under these conditions is between $|g, q\rangle \rightarrow |e, q-1\rangle$ states, i.e., the term where a photon is absorbed by a ground-state atom promoting the atom into an excited state.

This can also be understood on an intuitive level. The coupling from $|g, q\rangle \rightarrow |e, q+1\rangle$, is where both the atom and the field gain energy, and $|e, q\rangle \rightarrow |g, q-1\rangle$ is where both the atom and the field lose energy, both violate energy conservation. Therefore, by the Heisenberg uncertainty principle these interactions can only be allowed for short time periods.

The resulting Hamiltonian is a infinite series of 2-dimensional subspaces that are simpler solved. The Hamiltonian for each pair of decoupled states is,

$$H/\hbar = \begin{pmatrix} -\frac{\Delta}{2} & \Omega_0 \\ \Omega_0 & \frac{\Delta}{2} \end{pmatrix}.$$

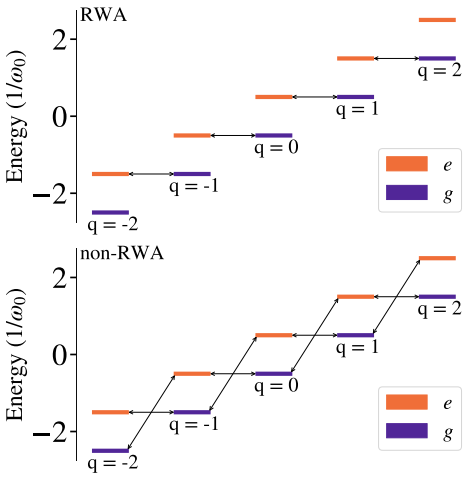

Figure 4.2: Energy-level structure for a driven two-level system in the Floquet picture of dressed atomic states, computed with and without the RWA. (RWA) Only the dominant first-order perturbation theory coupling for each state is shown. This results in an infinite series of de-coupled sub-systems. (non-RWA) All couplings are included resulting in a infinitely coupled system of dressed-states.

The solutions to these are superpositions of the $|g, q\rangle$ and $|e, q-1\rangle$ states.

In resonance ($\Delta = 0$), the solutions are two states given by $|\psi\rangle = \frac{1}{\sqrt{2}}(|g, q\rangle \pm |e, q-1\rangle)$, with eigenenergies equally spaced at,

$$E_\lambda/\hbar = \pm\frac{\Omega_0}{2}. \tag{4.7}$$

These eigenstates contain an equal mixture of the two atomic states and their energies are separated by the Rabi frequency. As the Rabi frequency is linear in the strength of the applied electric field this provides a direct method to measure the magnitude of electric fields.

In the context of spectroscopy, this splitting of eigenenergies is termed the Autler-Townes splitting [45], and in a fluorescence spectrum it appears as three peaks known as the Mollow triplet [60]. By measuring the Autler-Townes splitting of a pair of coupled levels, the value of Ω_0 can be directly measured, and then from Eq. 4.7 the electric field strength can be determined.

The effects of the ignored fast rotating terms can cause deviations from this idealised behaviour at larger coupling strengths. The interaction of the fully coupled system leads to deviations from this model of Autler-Townes peaks showing a linear splitting with electric field strength.

The perturbative correction to the model due to the non-energy-conserving virtual couplings is called the Bloch-Siegert shift [61]. This shifts the resonance condition for the system due to the neglected terms in the RWA Hamiltonian. The correction takes the form,

$$\delta_{bs} = \frac{\Omega_0^2}{4(\omega_0 + \omega)}. \tag{4.8}$$

The Bloch-Siegert shift and the AC-Stark shift are both shifts in the energy of the states, but have different causes. The AC-Stark shift is present even within the RWA, whereas the Bloch-Siegert shift is caused by the non-energy conserving terms ignored by the RWA. This shift can be observed as a slight deviation from linearity in the Autler-Townes splitting as a function of electric field strength.

We can specify some approximate regimes of the dynamics of a driven two-level atom based on Ω_0 and ω_0. In *the weak-driving regime*, $\Omega_0 \ll \omega_0$ and the RWA is a accurate representation of the system dynamics. *The strong-driving regime* ranges from where the Autler-Townes splitting is wider than the line-width of the transitions up-to where the RWA corrected by the perturbative Bloch-Siegert shift can explain the dynamics.

Then finally, we have *the ultra-strong driving* regime, where $\Omega_0 \geq \omega_0$. Here the perturbative approach fails, and the coupling between the atom and the field is strong, thus requiring a more complex description of the dynamics.

4.1.3 Applications for ultra-strong driving of Rydberg states

Before we present the results for the ultra-strong driving regime, we detail some applications that follows this exposition going beyond RWA.

The direct link between Autler-Townes splitting and coupling strength, Ω, makes quasi-two-level systems ideal electric field sensors. Rydberg atoms contain transitions in the RF and MW frequency ranges, which possess large electric dipole transition moments, making excellent microwave field sensors [62].

The large transition dipoles also mean that relatively weak electric fields lead to coupling strengths for which the RWA may no longer provide an accurate description of the dynamics. Therefore, an understanding of strong-field interactions is essential in determining the limits of the dynamic range of sensors realized using this technique [63].

Strong coherent interactions of atoms with electromagnetic fields are also of interest in areas other than sensing. In quantum computing, resonant fields are routinely used to prepare quantum states via Rabi flopping. Fast state preparation requires the use of stronger fields; thus, they eventually approach the regime in which the RWA breaks down [64].

Experiments extending to the few or single-photon regimes in superconducting circuits have led to realizations of the ultra-strong coupling regime of the quantum Rabi model, which is of interest to quantum information processing and for probing unexplored regimes of QED [65].

The use of strong off-resonant dressing fields have been investigated as a method to *polarizability-null* both low- and high-angular momentum Rydberg states, to decrease their sensitivity to stray static electric fields [66]. Microwave-based decelerators and traps operating in the strong driving regime [67] are of interest for the preparation of cold samples of Rydberg atoms and molecules.

4.2 Ultra-strong driving of high n Rydberg states

In these experiments investigating the ultra-strong driving regime of an atom interacting with a microwave field, we use low-ℓ Rydberg states in helium with principal quantum number $n = 105$. These states are ideal for this purpose because the quantum defects lead to the s and p states being isolated from the manifold of Rydberg-Stark states.

Furthermore, the exaggerated scaling of Rydberg state properties allow for strong transition dipole couplings between states with small transition frequencies. Consequently, a Rabi frequency equal to the transition frequency, $\Omega_0 \approx \omega_0$, is achievable at small electric field magnitudes. The scaling of these properties is shown in Figure. 4.3.

The $n = 105$ manifold has desirable properties for this type of experiment. The transition between the $\ell = 0$ and $\ell = 1$ levels at $n = 105$ is at $\omega_0 = 2\pi \times 1.304$ GHz, with a transition dipole moment of $d = e\,\langle 105, 1, 0|\, z\, |105, 0, 0\rangle = 8965.70\ ea_0$. This results in a Rabi frequency, $\Omega_0 = \frac{E_0 d}{\hbar}$, at fields on the order of 0.1 V/cm, approaching the transition frequency $\Omega_0 \approx \omega_0$.

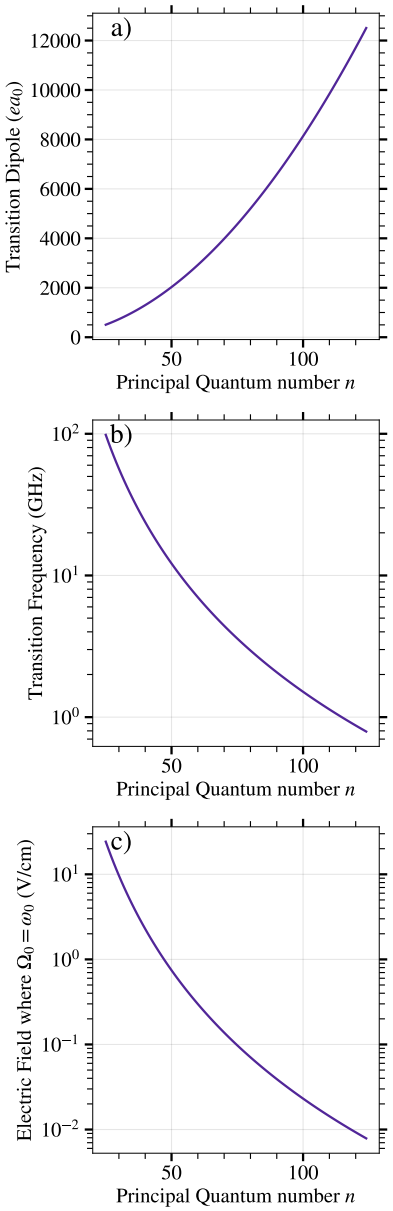

Figure 4.3: Figure showing the scaling of the transition dipole moment (a) and transition frequency (b) between $|n, 0, 0\rangle$ and $|n, 1, 0\rangle$ states, i.e., s and p states of the same n manifold in triplet Rydberg helium. c) shows the electric field strength F_{osc} required to achieve the ultra-strong driving regime where the Rabi frequency matches the transition frequency, $\Omega_0 = \omega_0$, for a resonant driving field.

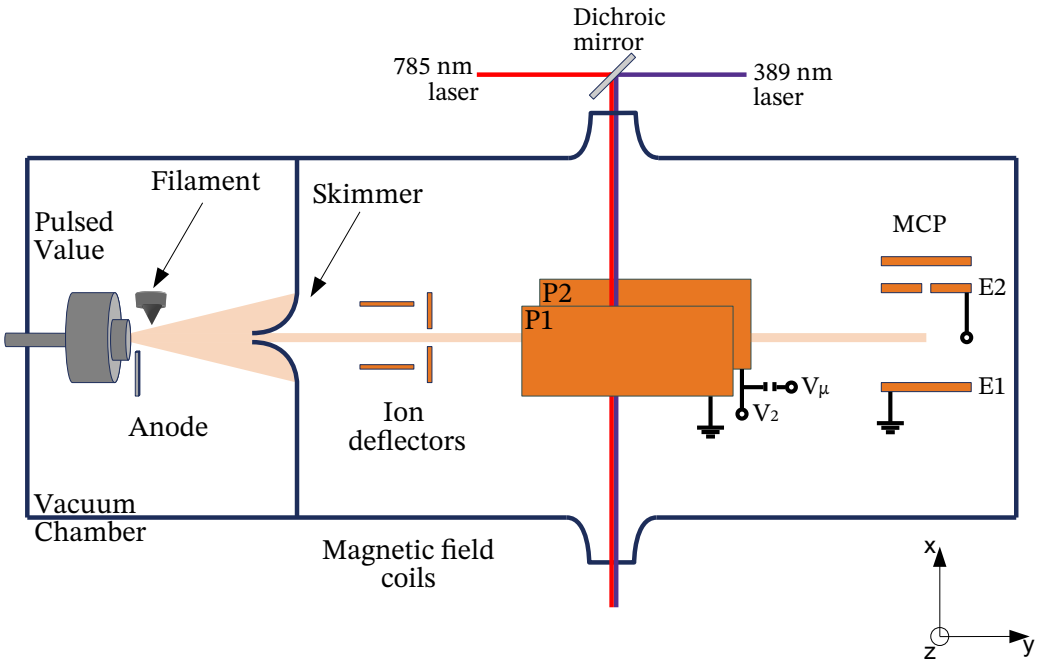

Figure 4.4: Schematic of the apparatus used in the experiments to study the effect of ultra-strong driving of a Rydberg transition in triplet helium. A pulsed supersonic beam was generated at the exit of a pulsed valve. This beam was then collimated by a skimmer. Rydberg photoexcitation by a 2 photon UV/IR transition took place between copper plates P1 and P2 under the influence of a microwave field applied directly to the plate P2, resonant with the $|105,0,0\rangle \rightarrow |105,1,0\rangle$ transition. The excited atoms are directed to the region between plates E1 and E2 for detection by pulsed electric field ionisation. This figure has been modified from [58]

4.2.1 Experimental procedure

A schematic diagram of the experimental apparatus is shown in Fig 4.4. A pulsed supersonic beam of helium atoms in the meta-stable $1s2s\,^3S_1$ level was generated in a dc electric discharge at the exit of a pulsed valve [53]. The beam with a mean longitudinal speed of 2000 ± 50 m/s, passed through a skimmer with a 2 mm diameter before entering a region where an electric field was generated to deflect and filter ions created in the discharge.

The atoms then entered a region defined by two parallel 70×105 mm copper plates, P1 and P2, separated by 13 mm in the z dimension. In this region, two co-propagating UV and IR laser beams intersected the atomic beam. The UV laser was stabilised to $\lambda_{uv} = 388.975$nm to drive the $1s2s\,^3S_1 \rightarrow 1s3p\,^3P_2$ transition. The IR laser was tuned in the range from 785.1669 to 785.1710 nm to drive the $1s3p\,^3P_2 \rightarrow 1s105s\,^3S_1/1s105d\,^3D$ transitions, and probe effects of the microwave field to the energy-level structure of the atom [68].

IR laser photo-excitation spectra recorded in the experiment allowed for probing of the Autler-Townes splitting [45] of the $1s3p\,^3P_2 \rightarrow 1s105s\,^3S_1$ transition in the presence of a 1.280 GHz microwave field tuned close to resonance to the $1s105s\,^3S_1 \rightarrow 1s105p\,^3P$ transition at 1.304 GHz. This particular microwave frequency was chosen to exploit

a resonance in the microwave circuit between the signal generator and electrodes in the apparatus. The microwaves were applied directly to the plate P2 via a capacitative coupling. This is in contrast to the later experiments in which a microwave antenna placed outside the chamber was used as shown in Figure 3.1

Following Rydberg state photo-excitation, the excited atoms traveled out between P1 and P2 and into the detection region between E1 and E2. During this 65 μs period of free flight, the microwave source was operated in pulsed mode to minimize losses by multi-photon microwave ionization. It was switched on 10 μs before the velocity class of those atoms selected for detection reached the photo-excitation lasers, then switched off 10 μs later.

Unless stated otherwise, for all experiments static offset potentials of $V_2 = \pm 12.5$ mV were applied to P1 and P2 to compensate stray electric fields in the z direction between these electrodes. When the atoms reached the detection region, a pulsed voltage of +295 V was applied to electrode E1, while E2 was maintained at 0 V. The resulting electric field ionized the excited Rydberg atoms and accelerated the ions through an aperture in E2 to a micro-channel plate (MCP) detector.

4.3 Results

We present results where the effects of ultra-strong microwave driving on the triplet Rydberg states in helium with $n = 105$ were investigated. The first set of experiments were performed in the regime for which $\Omega \ll \omega_0$, to calibrate the microwave field intensity in the excitation region of the apparatus. This was extended to the regime in which $\Omega \approx \omega_0$ and over a more extensive spectral range to investigate the breakdown of the two-level approximation, and the breakdown of the rotating wave approximation (RWA) in this system.

The results of all experiments performed were compared to the results of calculations carried out using the Floquet methods described in Sec. 2.4.1. The weak spin-orbit couplings in high-n Rydberg states scales as n^{-3} and give rise to energy level splittings of < 100 kHz for the Rydberg states with $n = 105$ studied here [49]. This means the Schrödinger equation associated with this Hamiltonian can be solved for in a $|n, \ell, m_q\rangle$ basis.

4.3.1 Microwave field strength calibration

Rydberg states are used as microscopic antennae for low-frequency electromagnetic fields [63]. This sensitivity is exploited in this first set of experiments to calibrate the 1.280 GHz microwave field strength in the photo-excitation region of the apparatus.

The Autler-Townes splitting of the $1s3p\,^3P_2 \rightarrow 1s105s\,^3S_1$ transition upon weak microwave driving, i.e., when $\Omega \simeq 40$ MHz $\ll \omega_0 = 2\pi \times$ 1.304 GHz was measured. In this regime the atom–microwave-field interaction can be described within the RWA. The relationship between

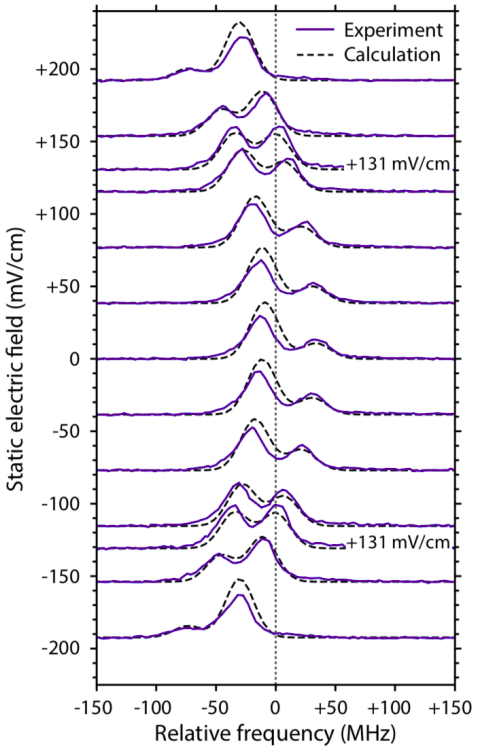

Figure 4.5: Measured (continuous curves) and calculated (dashed curves) spectra of the $1s3p\,^3P_2 \rightarrow 1s105s\,^3S_1$ transition in the presence of a 1.280 GHz microwave field. The spectra were recorded for a range of dc electric fields as indicated on the vertical axis. Figure taken from [58]

the Autler-Townes splitting and microwave field strength is given by the generalised Rabi frequency $\Omega = \sqrt{\Omega_0^2 + \Delta^2}$.

Measurements of this Autler-Townes splitting for a fixed value of $F_{\rm osc}$ are displayed in Fig 4.5. The relative frequency on the horizontal axis in this figure is displayed with respect to the zero-field $1s3p\,^3P_1 \rightarrow 1s105s\,^3S_1$ transition frequency.

In recording the data in Fig. 4.5, a resonance in the microwave circuitry at 1.280 GHz, which lies 24 MHz below ν_0, was used to enhance the microwave field strength in the laser photo-excitation region. Because of this detuning, the laser spectrum of the transition to the Autler-Townes split ($1s105s\,^3S_1$) level in zero dc electric field seen in the middle of Fig. 4.5 exhibits an asymmetric intensity distribution. The relative amplitude of the peaks depends on the detuning, Δ. Since $\Delta < 0$, the lower frequency Autler-Townes component has more S-character and therefore a higher spectral intensity.

To study the effects of detuning the microwave field from the 105s→105p atomic transition frequency, the measurements were also performed in a range of applied dc electric fields. As the dc offset electric field was adjusted, the 105s→105p transition undergoes a quadratic Stark shift. This causes the atomic transition to move through resonance with the fixed-frequency microwave field.

The resonance condition, for which $\Delta = 0$, occurs for $F_z = 131$ mV/cm. This can be seen from the corresponding spectra of the Autler-Townes splitting indicated in Fig 4.5. As $|F_z|$ approaches 131 mV/cm in these data, the spectral intensity distribution of the Autler-Townes components becomes increasingly symmetric as the applied dc field approaches this value.

The two spectral features have equal intensity when $|F_z| = 131$ mV/cm while for larger values of $|F_z|$ the detuning Δ is positive, and the asymmetric spectral intensities of the Autler-Townes peaks invert. Under these conditions, the higher frequency components exhibit greater S-character and hence intensity in the spectra.

The experimental data in Fig. 4.5 are compared to the results of numerical calculations (indicated by the dashed curves). These calculations rely on the methods described in Sec. 2.4.1 with a basis of states for which $n = 105$, $0 \leq \ell \leq 6$, $-\ell \leq m_\ell \leq \ell$ and $-5 \leq q \leq 5$, and for which the only free parameter was a single scaling factor used to convert the output of the microwave source to $F_{\rm osc}$.

Thus by performing a global fit to all of the experimental data in Fig. 4.5, the field strength at the position of the atoms in the experiment was determined to be 3.1 ± 0.5 mV/cm. This field corresponds to a microwave intensity in the laser photo-excitation region of the apparatus of 1.3×10^{-8} Wcm^{-2} and was generated when the output power of the microwave source was -26.5 dBm (2.2 μW).

4.3.2 Ultra-strong microwave driving

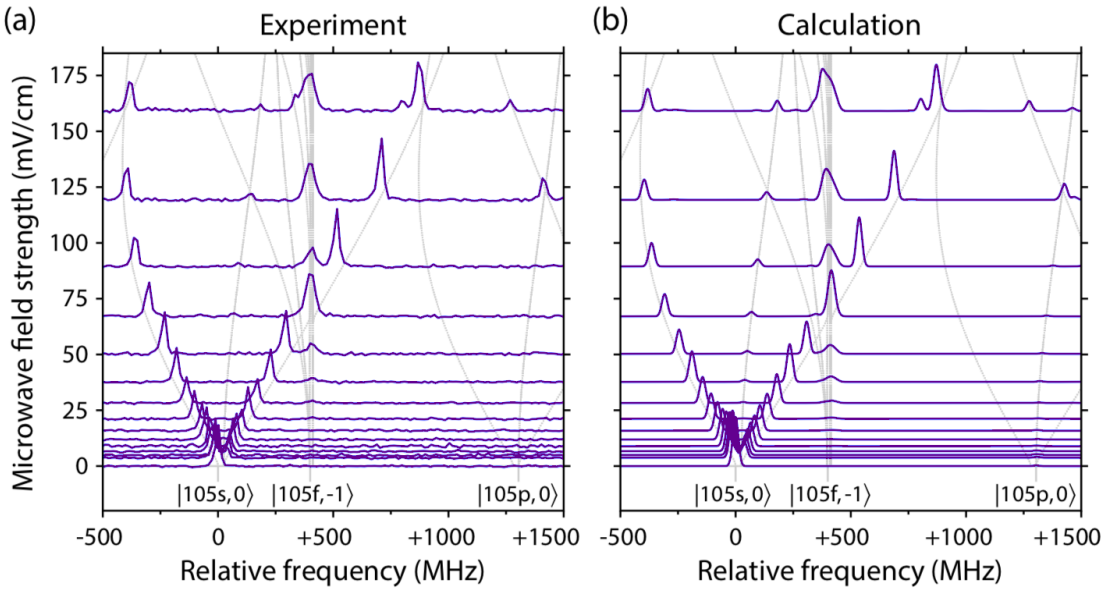

Figure 4.6: (a) Experimentally recorded, and (b) calculated spectra of transitions from the 1s3p ^{3}P$_2$ intermediate level to Rydberg states with ns and nd character in the presence of a $\nu_{\rm d} = 1.280$ GHz microwave field. The microwave field strength for which each spectrum was recorded is indicated by the vertical offset in each case. The thin grey curves in both panels represent the calculated Floquet quasi-energy level structure in the presence of the microwave field. Figure taken from [58]

Laser spectra recorded for microwave source output powers from -26.5 dBm to +9 dBm, hence microwave field strengths, $F_{\rm osc}$, in the photo-excitation region of 3.1 to 150 mV/cm are displayed in Fig 4.6(a). For the weakest microwave fields employed, the asymmetric intensity distribution of the Autler-Townes components of the transition to the 1s105s ^{3}S$_1$ level is clearly seen close to the zero frequency detuning. This can also be seen in the results of calculations performed for the corresponding microwave field strengths in Fig. 4.6(b).

To aid in the interpretation of the experimental data, the calculated energy-level structure indicted by the thin grey curves in Fig. 4.6(b) are also overlaid on the experimental data in Fig. 4.6(a). As the microwave

field strength is increased towards 50 mV/cm, the separation between the two Autler-Townes components, which corresponds to the Rabi frequency, Ω, increases approximately linearly.

Close to 50 mV/cm, an additional feature appears, indicated by the broad vertical grey bar, at a relative frequency of +400 MHz. This spectral feature is detuned by -ν_d from the interval between the $1s3p\,^3P_2$ level and the $1s105d\,^3D$ levels.

For values of F_{osc} greater than 50 mV/cm in Fig. 4.6(a), the field-dependent change in the Autler-Townes component of the transition to the $1s105s^3S_1$ level (that is shifted to negative relative frequency) deviates from a linear dependence on the microwave field strength. Other spectral features also appear in these higher microwave fields, e.g., additional peaks can be seen at +1250 MHz. These additional features correspond to the transition to the $1s105d\,^3D$ levels, which undergo an ac stark shift in the microwave field.

In general there is very good quantitative agreement between the experimental data and the results of the calculations over the full range of microwave field strengths seen in Fig. 4.6. These simulations required a larger basis than those in Fig. 4.5 and contained all states for which $103 \leq n \leq 107$, $0 \leq \ell \leq 8$, $-\ell \leq m_\ell \leq \ell$ and $-10 \leq q \leq 10$. Discrepancies occur between the calculations and the experimental data for the highest values of F_{osc}.

To identify the origin of the discrepancies, test calculations were performed with larger computational bases and the effects of the diamagnetic interaction of the atoms with the microwave field included. These did not yield an improved agreement between the experimental and calculated data. It is concluded that a reduction in the spectral purity of the microwave field at high operating powers was the most likely cause of the observed discrepancies.

4.4 Analysis

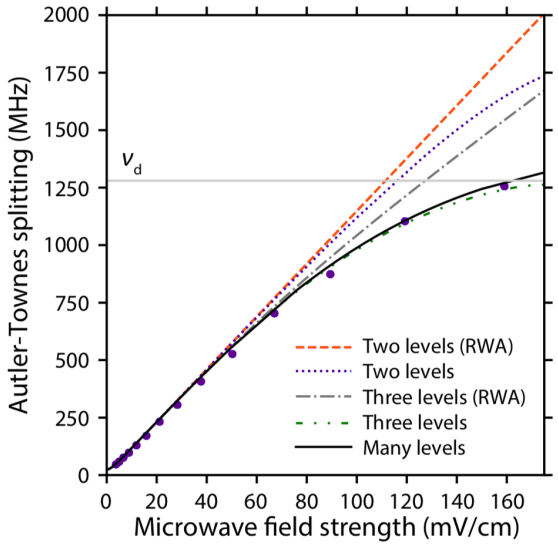

Figure 4.7: Dependence of the Autler-Townes splitting of the $1s3p\,^3P_2 \rightarrow 1s105s\,^3S_1$ transition on the strength of the 1.280 GHz microwave field. The splittings determined from the experimental data in Fig. 4.6 are indicated by blue points. Figure taken from Ref. [58].

The Autler-Townes splittings of the spectra shown in Fig. 4.6 aid in evaluating ranges of validity of simplified models of the atom–microwave-field interaction. It is seen that the Autler-Townes model is applicable for a two-level system within the RWA, however as seen in Fig. 4.6(b) levels other than the $|105\mathrm{s}\rangle$ and $|105\mathrm{p}\rangle$ states must contribute to the spectra particularly for higher values of F_{osc}.

An assessment of the applicability of the RWA and few-level approximations in simplifying the description of the Rydberg-atom–microwave-field couplings can be made from an analysis of the Autler-Townes splitting of the transition to the $|105\mathrm{s}\rangle$ state.

Comparisons between the experimentally measured $1\mathrm{s}105\mathrm{s}\,{}^3\mathrm{S}_1 \rightarrow 1\mathrm{s}105\mathrm{p}\,{}^3\mathrm{P}$ Rabi frequencies, determined from the Autler-Townes splitting of the $1\mathrm{s}3\mathrm{p}\,{}^3\mathrm{P}_2 \rightarrow 1\mathrm{s}105\mathrm{s}\,{}^3\mathrm{S}_1$ transition are displayed in Fig. 4.7 as blue dots, under-laid are theoretical models of either two- or three-level systems with and without the RWA.

The three-level model includes the $105d$ state. This state has a quantum defect of $\delta_{105,2} = 0.00289$ and frequency $\nu_d = 1676.7$ MHz relative to the $105s$ level. The $105p \rightarrow 105s$ transition dipole moment is $d_{p,d} = 8497.37\ ea_0$.

The energy levels for this three-level system in the Floquet picture are shown in Fig. 4.8. When all couplings are included, the system is complicated and requires an infinite number of states to fully compute the result of the couplings. By including only the dominant coupling between $105s \leftrightarrow 105p$ and the dominant coupling between $105p \leftrightarrow 105d$ states, the system can be reduced to a set of decoupled three-level Hamiltonians. In the weakest fields this can be justified by considering the detuning of each level.

Consider the $|105p, q = 0\rangle$ level, coupled to the $|105s, q = \pm 1\rangle$ and $|105d, q = \pm 1\rangle$ states. First order perturbation theory shows that,

$$|105p, q = 0\rangle = \Sigma_{n=s,d}\Sigma_{q=\pm 1}\frac{d_{n,p}}{E_n - E_p + q\hbar\omega_0}. \tag{4.9}$$

The transition dipole moments associated with the couplings are similar at $d_{s,p} = 8965.69\ ea_0$ and $d_{p,d} = 8497.37\ ea_0$. The detuning of each side-band determines the relative weight of the perturbation.

The state with the smallest detuning is the $|105s, q = +1\rangle$ level, which is only detuned by $2\pi \times -24$ MHz. This is the level that is included in the RWA model. The next nearest state is the $|105d, q = -1\rangle$ level, which is detuned by $2\pi \times -908$ MHz. The other two coupled levels are detuned by $2\pi \times 1652$ MHz, $2\pi \times -2584$ MHz these are the $|105d, q + 1\rangle$ and $|105s, q - 1\rangle$ levels respectively.

Under the assumption that only the first two couplings have an impact on the dynamics, each $|105p, q\rangle$ state is coupled to $|105s, q + 1\rangle$ and $|105d, q - 1\rangle$ states. These couplings are shown in Fig. 4.8 RWA), indicating that each state is only coupled to two other states. In analogy with the two-level system, this is considered the three-level RWA model for the analysis of the experiment. This is due to only the energy conserving terms where the absorption/emission of a photon is paired with the energy conserving transition in the atom.

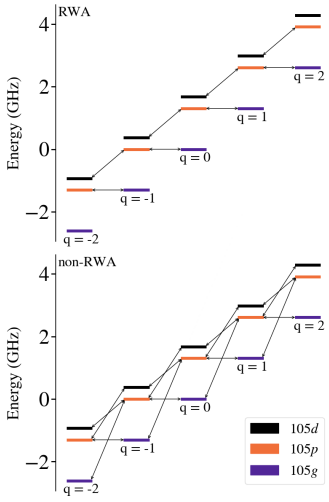

Figure 4.8: Energy level structure for a driven three level system, consisting of the 105s, 105p and 105d states of helium with $m_\ell = 0$. The dressed states are shown in the Floquet picture with the q quantum number representing the relative number of photons in the resonant microwave field. non-RWA) Only the dominant first order perturbation theory coupling for each state is shown. These correspond the the energy-conserving interactions analogous to those shown in Figure 4.2. RWA) All couplings are indicted by arrows.

Name	**States included**
Two-Level RWA	$\left\|105s, q=0\right\rangle, \left\|105p, q=-1\right\rangle$
Two-level	$\left\|105s\right\rangle, \left\|105p\right\rangle$ with $-10 \leq q \leq 10$
Three-Level RWA	$\left\|105s, q=0\right\rangle, \left\|105p, q=-1\right\rangle$ and $\left\|105d, q=-2\right\rangle$
Three-Level	$\left\|105s\right\rangle, \left\|105p\right\rangle$ and $\left\|105d\right\rangle$ with $-10 \leq q \leq 10$
Many-Level	$103 \leq n \leq 107$, $0 \leq \ell \leq 8$, $-\ell \leq m_\ell \leq \ell$ and $-10 \leq q \leq 10$.

Table 4.1: Models used for comparison of Autler-Townes splitting.

The Autler-Townes splittings in five different models are shown in Fig. 4.7. These five models and the states they include are described in Table. 4.1. In the weak driving regime, i.e., for microwave field strengths below $F_{\text{osc}} \approx 50$ mV/cm (Rabi frequencies $\lesssim \omega_0/2$), the approximately linear increase in the observed Autler-Townes splitting as the microwave field strength is increased, suggests that the RWA and two-level approximations remain valid. Beyond $F_{\text{osc}} \approx 50$ mV/cm, the two-level RWA model begins to deviate from the experimental data.

The Autler-Townes splittings and hence the Rabi frequency obtained from these three-level models remain in good qualitative agreement with the experimental data up to $F_{\text{osc}} \simeq 80$ mV/cm. For field strengths beyond this, the three-level RWA model that predicts a linear increase in the Autler-Townes splitting, breaks down, while the experimental data begins to converge toward a splitting $\Omega/2\pi = \nu_{\text{d}}$. However, the non-RWA calculations do reflect the observed splitting up to the final measured data point, and only deviates from the full calculation at the highest microwave field strengths.

A notable difference that can be seen between the RWA and non-RWA models is the saturation of the Autler-Townes splitting. The eigenenergies of the states surrounding the $\left|105s, q=0\right\rangle$ state are shown as a function of F_{osc} for the two and three level models in Fig. 4.9.

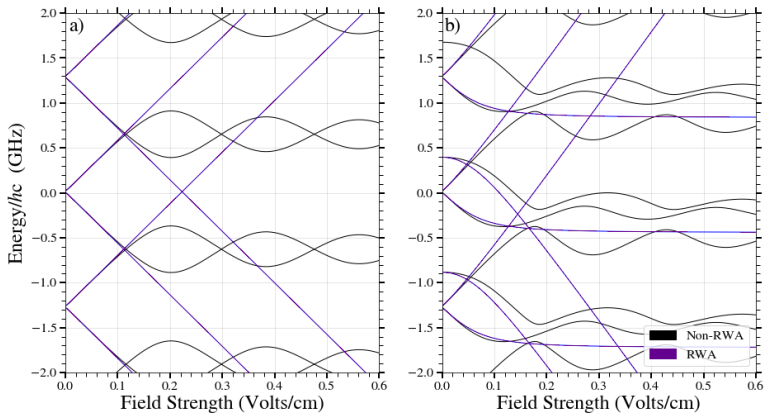

Figure 4.9: Energy level structure of models consisting of $n = 105$ states in helium. a) Two level model and b) three level model.

In the non-RWA models at high powers, side-bands which meet result in avoided crossings. Under ultra-strong driving, these avoided crossings lead to an energy-level structure dominated by integer multiples of the drive frequency. The RWA decouples the levels that undergo these avoided crossings.

The neglected coupling means that instead of undergoing avoided crossings, the energy levels continue to diverge as they cross states of other side-bands. The saturation of the Autler-Townes peaks seen in the experimental data is therefore concluded to be a signature of the breakdown of the RWA.

From the data in Fig. 4.7 it can be seen that the two-level approximation is valid up to the regime in which $\Omega/2\pi \simeq 0.5\nu_{\rm d}$. In this strong driving regime, it is possible to investigate the role of the Bloch-Siegert shift in the atomic resonance frequency on the measured Rabi frequency [61], [69].

This Bloch-Siegert shift represents a higher-order correction to the transition frequency of a pure two-level system that occurs under strong resonant driving. To identify corrections from the Bloch-Siegert shift in the experimental data in Fig. 4.6, calculations were performed to determine the non-RWA contributions to the Autler-Townes splitting in the two-level system.

The results of this calculation are shown in Fig. 4.10. In this figure, the energy-level splitting calculated within the RWA is subtracted from the results of each calculation. Hence, for all driving field strengths, the change in the Autler-Townes splitting obtained for the pure two-level system in the RWA is zero (dashed line).

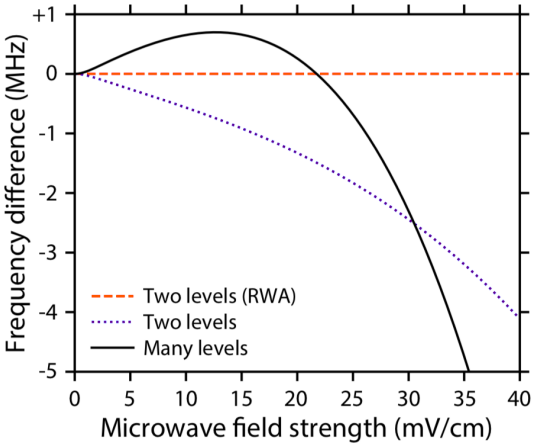

Figure 4.10: Calculated deviation of the Autler-Townes splitting in weak microwave fields from that obtained within the RWA shown as a dotted orange curve. The dotted purple curve shows the results for a two level system including terms ignored in the RWA, obtained numerically with $-10 \leq q \leq 10$. The black solid curve shows the expected shift including additional Rydberg states.

The difference in the Autler-Townes splitting obtained for a pure two-level system that includes interactions beyond the RWA is indicated by the dotted line. From this it can be inferred that the Rabi frequency, and hence the Autler-Townes splitting, should decrease from that predicted by the RWA when the Bloch-Siegert shift becomes significant.

However, it can be seen from the continuous black curve in Fig. 4.10 that in the calculations performed by determining the eigenvalues of the complete multi-level Floquet Hamiltonian with $-10 \leq q \leq 10$, the Autler-Townes splitting is observed to increase in weak fields up to 15 mV/cm. This is similar to the observations Ref. [70], where the asymmetry of Autler-Townes peaks was used to determine the resonant frequency of an ultra-strongly driven quantum well.

In this work, ac-Stark shifts arising from the off-resonant coupling to

a third level were found to be dominant over the Bloch-Siegert shift. In the case of interest here, we conclude that under the conditions for which the measurements reported were performed, the two-level approximation breaks down before the RWA does, masking the effect of the Bloch-Siegert shift.

4.5 Applications for microwave deceleration and trapping

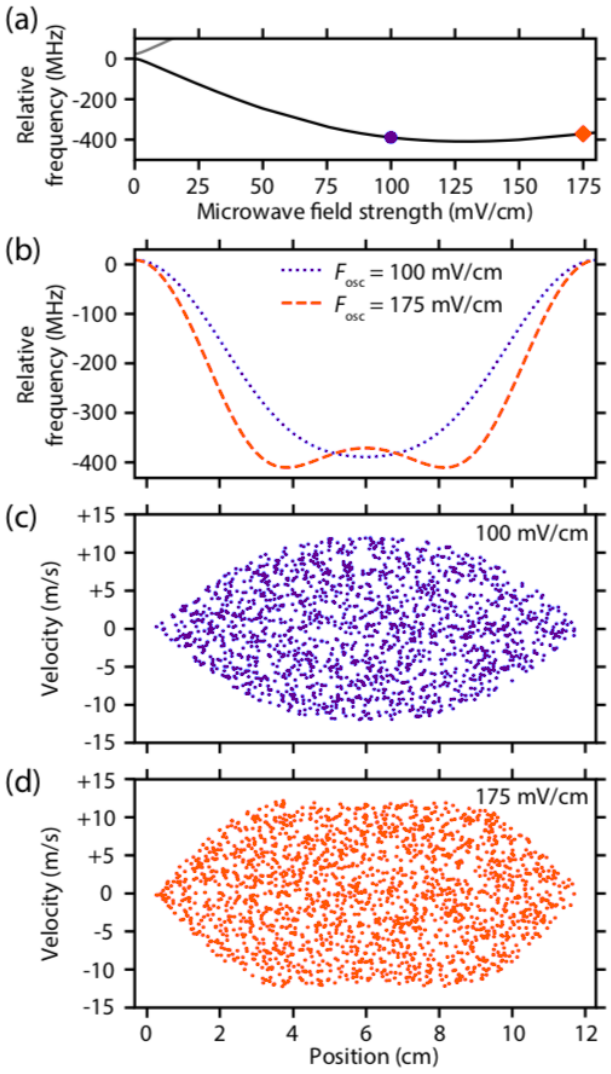

Figure 4.11: (a) Energy level shift of the triplet $|105s\rangle$ state of He in the presence of a 1.280 GHz microwave field. (b) Corresponding potential energy distribution for this atom near the 0.10 V/cm (dashed curve) or 0.175 V/cm (dotted curve) intensity maximum of a single node of this field. (c) and (d) Phase space acceptance of a trap based on the two potentials in (b).

The ultra-strong Rydberg-atom-microwave-field interactions reported here can be exploited in the realization of microwave decelerators and traps for cold Rydberg atoms and molecules. Such devices are of particular interest in hybrid cavity QED experiments with atoms in circular Rydberg states and superconducting microwave circuits[30], [71], and in experiments with cold Rydberg positronium atoms.

This approach to deceleration and trapping takes advantage of the force on an atom or molecule in a spatially inhomogeneous microwave field, $\mathbf{f} = -\nabla W$, where W is the potential energy of the atom in the field. Forces of this kind accelerate samples with positive (negative)

energy shifts in the presence of the microwave field towards regions of low (high) field strength. The corresponding states are then referred to as low-field-seeking [LFS] (high-field-seeking [HFS]).

From the data in Fig. 4.6 the LFS or HFS character of a particular field-free energy level can be inferred, e.g., the $1s105s\,^3S_1$ level in the presence of a strong near-resonant microwave field, can be selected by the appropriate choice of the detuning of the microwave field from resonance. Accordingly, this approach to decelerating and trapping Rydberg atoms and molecules is particularly versatile and applicable to a wide range of states, including non-degenerate states, which are purely HFS in static electric fields, i.e., low ℓ Rydberg states in non-hydrogenic atoms and molecules, or circular states.

Microwave decelerators have recently been implemented for ground-state polar molecules [67]. In these devices, the field distribution in a cylindrical microwave resonator is used and detuned below resonance to prepare and decelerate HFS ammonia molecules. To determine the phase space acceptance and optimal mode of operation of a decelerator for He atoms in the very high n Rydberg states considered here, numerical particle trajectory calculations for a microwave trap based on the parameters of the experiments reported in Sec. 4.3.1 were performed.

As in Sec. 4.3.1, the detuning of -24 MHz of the microwave field from the atomic transition frequency determined that atoms prepared in the $|105s\rangle$ state were HFS. The adiabatic evolution of the resulting driven $1s105s\,^3S_1$ level in the applied microwave field is shown in Fig. 4.11(a). Detuning selection plays an important role in negating non-adiabatic population transfer when atoms traverse regions of low field strength.

In a resonant field, these states would be degenerate, and a significant population could change state in the region of zero microwave field strength and then be ejected from a trap. As a result, control over the microwave frequency provides both the ability to choose which free-field state is addressed and also provides a method to protect this selected state from non-adiabatic losses.

Fig. 4.11(b) shows the potential energy of a He atom in the $|105s\rangle$ state over the full length of the trap, i.e., for a half wavelength of the standing microwave field, for the two maximum field strengths highlighted by the points in Fig. 4.11(a). The blue dotted line corresponds to a maximum field strength of 0.10 V/cm; in this situation, the trap has a single minimum located at its center where the field amplitude is greatest. The dashed red curve corresponds to a maximum field strength of 0.175 V/cm for which the state has gone through an avoided crossing and become LFS (see Fig. 4.11(a)). This results in a trap for which two minima form, located on either side of the center.

This non-monotonic evolution of the atomic state energy allows for tunable trap geometries using only the amplitude of the field. The phase space acceptance of these two traps are shown in Fig. 4.11(c) and Fig. 4.11(d), respectively. The maximum speed of the atoms which can be trapped in these traps is ~ 10 m/s, which corresponds to a translational temperature of 10 mK. The depth of the trap is directly related to the energy shift of the state in the microwave field. This represents

the maximum kinetic energy that an atom can have without escaping from the trap. Additional calculations (not shown) indicate that for the $|50s\rangle$ and $|50p\rangle$ states, the frequency shift of the corresponding turning point is $\simeq$ 4 GHz for $\nu_{\rm d}$ = 12.15 GHz with $F_{\rm osc} \simeq$ 5V/cm, giving a trap depth of around 300 mK.

4.6 Conclusions

We have observed coherent Rydberg-atom–microwave-field interactions in the ultrastrong-driving regime for which $\Omega \sim \nu_0$. The experimental data are in excellent quantitative agreement with the results of numerical calculations of the energy-level structure and spectral intensities of the atom dressed by the microwave field. These were performed using Floquet methods and comparisons were made with simplified models.

These simpler models within the two-level and rotating-wave approximations demonstrate that for the Rydberg states used in the experiments, these approximations are valid provided $\Omega \lesssim 0.5\nu_0$. The results presented are of importance for applications of Rydberg atoms in the detection and precise calibration of microwave fields.

The thorough understanding of the energy-level structure of high Rydberg states in the ultrastrong-driving regime obtained in this work has allowed an evaluation of microwave trapping schemes for the confinement of cold Rydberg atoms and molecules. The trap depths that are expected to be achieved in such devices, based on the parameters of the experiments reported here, are appropriate for applications in hybrid quantum information processing and the preparation of cold samples of Rydberg atoms and molecules.

Part II

Interferometry with Rydberg states

5
Interferometers and Rydberg atom interferometry

5.1 Origins of atom interferometry

Over the past 150 years, numerous types of interferometers have been developed. Examples like the Mach-Zehnder interferometer, split a single wave source into two physically separated paths, which are then brought back together. The measurement of the relative phase $\delta\phi$ between the two paths contains information about differences in their lengths or the media through which they propagate. Others, such as Young's double-slit experiment, split a single wavefront into multiple point sources. The specifics vary depending on the type of wave involved and the quantity being observed, but fundamentally, these interferometers convert phase differences into measurable quantities.

The use of interference as a scientific tool originates from studies on the nature of light. This enduring question preoccupied many great thinkers throughout the Classical, Islamic Golden, and Renaissance ages. For centuries, the general consensus was that light consisted of particles. However, in the 17^{th} century, Young's demonstration of the interference of light [72] provided strong evidence that light behaves as a wave. Further proof was provided by Fresnel, who unified Young's findings with Huygens' wave theory of light.

Accepting light as a wave necessitated the existence of a medium through which it propagates, analogous to how water waves propagate through water and sound waves through air. This hypothetical medium, called the *luminiferous aether*, was theorized to permeate the entire universe. However, the properties of the aether and how it interacted with moving bodies remained open questions in the second half of the 19^{th} century.

Interferometry was the key tool for probing the aether. If light waves travelled through the aether, then the Earth's motion through the aether would affect the speed of light in different directions, leading to measurable phase differences in an interferometer. Fizeau was the first to design such an experiment in 1851, using light propagation in moving water [73]. Later, in the 1880s, Michelson and Morley pioneered highly precise interferometers using a rotating design. Their experiments found no difference in the speed of light due to Earth's motion through the aether, ultimately disproving its existence and setting the stage for tests of special relativity [74].

Around this time, physics was undergoing a major upheaval, with the classical intuition being challenged by new experimental findings. Key developments included Planck's introduction of quantized energy levels to explain black-body radiation [75] and Einstein's proposal of light quanta (photons) to explain the photoelectric effect [76]. These ideas led to the formulation of quantum mechanics and the acceptance of wave-particle duality.

In 1924, de Broglie postulated the wave-like nature of matter, introducing the concept that particles have an associated wavelength, now known as the de Broglie wavelength [77]. This wavelength is given by

$$\lambda = \frac{h}{p}, \tag{5.1}$$

where h is Planck's constant and p is the momentum of the particle. This groundbreaking idea established that particles exhibit wave properties, showing their de Broglie wavelengths are inversely proportional to their momentum.

Soon after this conjecture, experimental evidence of matter-wave behaviour emerged. In 1927, Davisson and Germer observed the diffraction of electrons scattered off nickel crystals [78], and independently, Thomson observed electron diffraction through a celluloid film [79]. These experiments confirmed the wave nature of particles and marked the beginning of matter-wave interferometry.

These techniques eventually led to the development of the electron biprism [80] in the 1950s, enabling the recreation of Young's double-slit experiment with electrons [81]. This also allowed for tests of quantum mechanical effects such as the Aharonov-Bohm effect [82] via electron wave interference [83], [84].

In parallel, the development of interferometry with atoms was progressing. In 1922, Stern and Gerlach performed an experiment demonstrating that the angular momentum of atoms is quantized [85]. In their experiment, a beam of silver atoms was passed through an inhomogeneous magnetic field, resulting in the deflection of the atoms based on their magnetic moments, as illustrated in Figure 5.1.

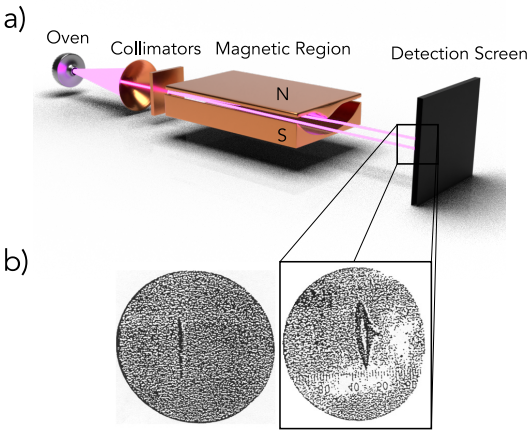

Figure 5.1: The experiment performed by Stern and Gerlach in 1922 to deflect silver atoms via an inhomogeneous magnetic field. (a) shows a schematic of the experiment, and (b) shows the results taken from [85]; the splitting of the beam (right) was the first demonstration of the quantization of the magnetic moment, specifically probing the spin angular momentum of electrons (spin-$\frac{1}{2}$ particles) within the atoms.

This experiment provided direct evidence of the quantization of angular momentum, specifically the electron's spin angular momentum.

According to classical physics, the magnetic moment of an atom could take any orientation, and so, one would expect a continuous distribution of deflections. However, the observed discrete splitting of the atomic beam confirmed that the magnetic moment, and thus angular momentum, is quantized.

Rabi modified this apparatus in 1938 [86]. Rabi realized that an oscillating magnetic field on resonance could induce transitions between different magnetic sublevels m_ℓ in a coherent manner [87]. Applying this additional oscillating field in the Stern-Gerlach apparatus, he developed a method to measure transition frequencies between quantized energy levels. This forms the basis of magnetic resonance spectroscopy, and remains relevant for present-day atom-based interferometers.

Ramsey further refined this technique by splitting the interaction with the oscillating magnetic field into two separate regions [88]. By separating the interaction regions, an interferometer was formed where the frequency of the oscillating field acted as a reference clock against the atomic transition frequency. This method greatly increased the precision of spectroscopic measurements and is known today as Ramsey interferometry.

An alternative perspective on the Ramsey interferometer is to compare it with the Mach-Zehnder interferometer. While the Mach-Zehnder interferometer uses beam splitters to separate and recombine two paths in real space, the Ramsey interferometer uses oscillating fields to separate and recombine paths in the internal quantum state space of the atom, effectively forming an interferometer in the spin-$\frac{1}{2}$ Hilbert space.

Serge Haroche utilized the Ramsey technique to perform experiments probing the interaction between light and matter [89]. These experiments used highly excited Rydberg states of atoms with transitions in the microwave frequency range. By passing beams of these atoms through high-Q microwave resonators configured to produce a Ramsey interferometer, the few-photon [90] and single-photon regimes could be explored.

Performing interferometry with atoms is appealing because their de Broglie wavelengths are significantly shorter than those of photons in optical interferometry. Shorter wavelengths correspond to higher momentum particles, which can lead to increased sensitivity to certain physical effects. Specifically, the phase shift accumulated in an interferometer scales inversely with the de Broglie wavelength. Therefore, using atoms with shorter de Broglie wavelengths allows the interferometer to probe smaller spatial scales and detect finer variations in potentials or inertial forces.

Furthermore, atoms are massive particles, inherently sensitive to inertial forces such as accelerations and rotations, as well as gravitational potentials. This sensitivity enables atom interferometers to perform precise measurements of inertial effects, making them invaluable in applications like gravimetry, seismology, and inertial navigation [91], [92]. The ability to measure gravitational acceleration with high accuracy has profound implications for geophysics and the detection of gravitational anomalies.

Another significant advantage is the ability to coherently manipulate the internal states of atoms. Atoms possess rich internal structures with discrete energy levels that can be precisely controlled using electromagnetic fields, such as lasers and microwaves. This control allows for the creation of superposition states, and ability to impart controlled momentum transfer allowing the implementation of sophisticated interferometry schemes that probe fundamental quantum phenomena [93]. The manipulation of internal states enhances the versatility of atom interferometers, enabling them to measure a wide range of physical effects.

Atom interferometers can be configured to operate in different regimes, providing versatility in measurement capabilities. External-state interferometers manipulate the atomic motion, making them highly sensitive to inertial effects, while internal-state interferometers focus on the internal quantum states, allowing for precise measurements of energy differences due to external fields. Mixed interferometers combine both approaches for simultaneous sensitivity to multiple effects [94]. This flexibility enables atom interferometers to be tailored to specific measurement objectives across various scientific disciplines.

In summary, the inherent properties of atoms, including their short de Broglie wavelengths, mass, and internal structures, confer significant advantages in interferometry. These advantages enhance phase sensitivity, enable precise measurements of inertial and gravitational effects, and allow for versatile configurations tailored to specific measurement needs.

5.2 Types of atom interferometry

Since the pioneering experiments of the 1990s, advancements in atom cooling and trapping have increased interferometer interrogation times and phase sensitivities. Matter-wave interferometers, which exploit the wave nature of atoms, are sensitive to the trajectory of spatially separated wave packets. Because atoms are massive particles, they are well suited for use as gravimeters and accelerometers. More recently, there has been a shift in focus toward translating these experiments from the laboratory to practical real-world applications [95].

In this section, we discuss the broad categories of atom interferometers, categorizing interferometers based on how they manipulate atomic states and what physical effects they measure. We distinguish between external-state, internal-state, and mixed (external and internal) atom interferometers.

5.2.1 External-state atom interferometers

External-state atom interferometers manipulate the atomic wave packets in real space by altering their external degrees of freedom—such as position and momentum—*without changing their internal energy states*. By focusing solely on the external paths of the atoms, these

interferometers become inherently sensitive to inertial effects like acceleration and rotation. This sensitivity arises because inertial forces directly influence the atoms' trajectories, leading to measurable phase shifts when the paths are recombined.

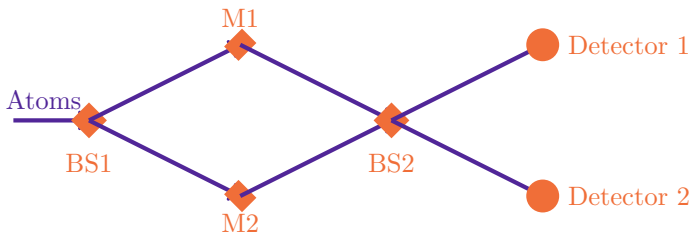

Figure 5.2: Abstract external-State Atom Interferometer: Atoms are split into spatially separate paths using beam splitters and mirrors. The paths recombine before detection.

In these interferometers, laser pulses act as beam splitters and mirrors, employing mechanisms like *Bragg diffraction* to impart momentum to the atoms through photon recoil while keeping their internal states unchanged [96], [97]. Bragg pulses coherently scatter the atoms, changing their momentum without altering their internal energy levels. This selective manipulation allows the atoms to accumulate phase differences based solely due to external influences along their paths, effectively exposing them to inertial effects.

A prominent example is the Mach-Zehnder interferometer implemented with Bragg pulses. In this setup, atoms undergo a sequence of laser pulses. First a $\pi/2$ pulse to coherently split the atomic wave packet into two spatially separate paths, then a π pulse to redirect (or "mirror") the paths, and a final $\pi/2$ pulse to recombine them—all achieved without changing the internal state of the atoms. Since the internal states remain unchanged throughout this process, any observed phase shift upon recombination is attributed entirely to differences in the external paths caused by inertial forces like gravity or acceleration.

The phase shift $\Delta\phi$ due to an acceleration a is given by:

$$\Delta\phi = 2k_{\text{eff}}\, a\, T^2 \tag{5.2}$$

where k_{eff} is the effective wave vector of the Bragg pulses, and T is the time between pulses. This quadratic dependence on time makes external-state interferometers exceptionally sensitive to inertial forces. By manipulating only the external degrees of freedom, these interferometers maximize their exposure to inertial effects, enabling precise measurements of external forces acting on the atoms during their free evolution.

External-state atom interferometers using Bragg diffraction have achieved remarkable sensitivities. Ground-state matter-wave interferometers with interrogation times on the order of seconds have reached nanogravity (ng) sensitivities in laboratory settings [91], [98]. Such high sensitivity is crucial for applications in precision measurements of gravity, rotational sensing for navigation systems, and tests of fundamental physics.

By exclusively altering the external paths and keeping the internal states unchanged, external-state atom interferometers effectively couple to inertial effects. This characteristic distinguishes them from other types of interferometers and highlights their unique capability to probe inertial forces with high precision.

5.2.2 Internal-state atom interferometers

Figure 5.3: Internal-state atom interferometer: Atoms remain in the same spatial path but transition between internal states using coherent pulses. The phase difference accumulates due to energy differences between states.

Internal-state atom interferometers rely on manipulating the internal quantum states of atoms without significantly altering their external motion. These interferometers are sensitive to energy differences between internal states, which can arise from interactions with electromagnetic fields or other perturbations. The Ramsey interferometer is a classic example of this type.

In a Ramsey interferometer [88], two coherent oscillating fields drive transitions between internal states, creating a superposition. The phase difference accumulates due to energy differences during the free evolution between pulses. This phase difference is then mapped onto measurable populations in the internal states upon application of the second pulse.

Internal-state interferometers are ideal for precision spectroscopy and measurements of energy shifts due to interactions with fields. They form the basis of atomic clocks, where the precise measurement of the transition frequency between two internal states of an atom is used as reference to define the second [99]. For instance, caesium atomic clocks utilize the hyperfine splitting of the ground state of caesium-133 atoms to maintain precise time standards [100].

Serge Haroche's experiments with Rydberg atoms in microwave cavities [89] are a notable example of internal-state interferometry. By using highly excited states and precise control over the interaction with single photons, these experiments explored fundamental aspects of quantum electrodynamics and quantum information. The ability to control and measure the quantum states of Rydberg atoms allowed for the demonstration of quantum entanglement and the observation of decoherence processes at the quantum level.

Moreover, internal-state interferometers have been employed to study fundamental physics, such as tests of quantum electrodynamics, measurements of atomic polarizabilities, and investigations of parity violation [101]. The sensitivity to internal energy shifts makes these interferometers powerful tools for probing interactions that affect the atomic energy levels.

Advancements in laser technology and cooling techniques have sig-

nificantly enhanced the capabilities of internal-state interferometers. Developments in laser stabilization and narrow-linewidth lasers have improved the coherence times and spectral resolution achievable in these systems [102]. Additionally, the use of ultracold atoms trapped in optical lattices has minimized Doppler and recoil effects, leading to optical lattice clocks with unprecedented precision [103].

Applications of internal-state interferometers extend beyond timekeeping. They are employed in precision measurements of fundamental constants, such as the fine-structure constant and the electron-to-proton mass ratio [104]. Furthermore, they serve as sensitive probes for detecting minute external fields, making them valuable in fields like magnetometry and gravitational sensing [105].

5.2.3 Mixed atom interferometers

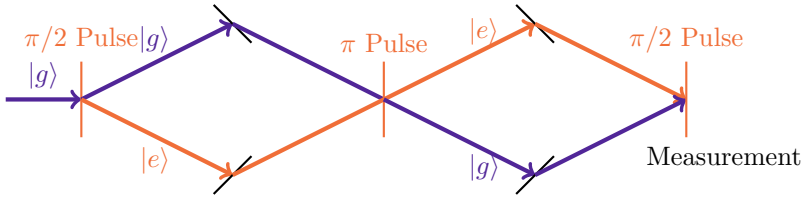

Figure 5.4: Mixed atom interferometer: Atoms undergo both spatial splitting and internal state transitions, combining the sensitivities of external and internal interferometers.

Mixed atom interferometers combine both internal and external state manipulations. They involve transitions between internal states accompanied by momentum transfers, allowing simultaneous sensitivity to both potential energy differences and inertial effects. The Ramsey-Bordé interferometer is a prominent example of this type.

The Ramsey-Bordé interferometer [94], [106] utilizes four traveling-wave laser pulses to manipulate the atoms. The laser pulses drive two-photon Raman transitions between internal states, imparting momentum kicks to the atoms due to photon recoil. This creates spatially separated wave packets in different internal states.

In the Ramsey-Bordé interferometer, the accumulated phase difference includes contributions from both the internal state energies and the external motion of the atoms. The interferometer is sensitive to both inertial effects and energy shifts due to interactions with external fields. This hybrid approach enables versatile measurements, allowing the interferometer to probe effects that purely internal or external interferometers cannot.

For example, the phase shift in a Ramsey-Bordé interferometer due to acceleration is given by [94]

$$\Delta\phi = (k_1 + k_2)aT^2, \tag{5.3}$$

where k_1 and k_2 are the wave vectors of the two photons involved in the Raman transition, a is the acceleration, and T is the time between pulses. The interferometer is also sensitive to energy differences between the internal states, which can be affected by external fields.

Advancements in cooling and trapping techniques have enabled the use of ultracold atoms in these interferometers, increasing interrogation

times and enhancing sensitivity. Bose-Einstein condensates (BECs) have been utilized to achieve high-contrast interference patterns [107].

In mixed atom interferometers, the coupling of internal state transitions with momentum transfer allows inertial effects to be read out from the internal state phases. When atoms undergo transitions between internal states while receiving momentum kicks, any inertial forces acting on the atoms during their propagation cause phase shifts that are imprinted onto the internal state populations. This contrasts with external-state interferometers, where inertial effects are measured through changes in the external paths without altering internal states.

In the Ramsey-Bordé interferometer, the final populations of the internal states after recombination depend on the accumulated phase difference, which includes contributions from both the internal energy differences and the inertial effects experienced due to the atoms' motion. Therefore, by measuring the internal state populations, one can infer both the inertial effects and any potential energy shifts affecting the internal states.

This dual sensitivity enhances the interferometer's versatility. While external-state interferometers are primarily sensitive to inertial effects like acceleration and rotation, and internal-state interferometers are sensitive to energy differences due to interactions with external fields, mixed interferometers can simultaneously probe both types of effects. This makes them powerful tools for precision measurements, such as tests of fundamental constants, measurements of gravitational acceleration, and exploration of quantum electrodynamics effects.

Mixed atom interferometers have been employed in various precision measurement experiments. For example, they have been used to measure the fine-structure constant [108] and to test the equivalence principle [109]. Advancements in laser technology and cooling techniques have facilitated the use of ultracold atoms and Bose-Einstein condensates in these interferometers, leading to longer interrogation times and improved coherence [110]. The ability to manipulate both internal and external degrees of freedom provides greater control over the interferometric processes, enhancing sensitivity and enabling new experimental possibilities.

5.3 Rydberg atom interferometry

Rydberg atoms, characterized by their high principal quantum numbers, possess large electric dipole moments and polarizabilities. These properties make them highly sensitive to electric fields and suitable for exploring new regimes in matter-wave interferometry.

Serge Haroche and colleagues pioneered the use of Rydberg atoms in internal-state interferometry [89]. In their experiments, beams of Rydberg atoms interacted with high-Q microwave cavities, forming a Ramsey interferometer. The atoms underwent transitions between Rydberg states induced by microwave fields, allowing for precise manipulation and measurement of their internal quantum states. This internal-state Ramsey interferometry enabled the exploration of fun-

damental quantum phenomena, such as the interaction between light and matter at the single-photon level [90].

Building upon these foundations, researchers have investigated the coupling between the internal states of Rydberg atoms and their external motion. The large electric dipole moments of Rydberg atoms lead to significant state-dependent forces when they are subjected to inhomogeneous electric fields. In such fields, different internal states experience different accelerations due to the spatial variation of the potential energy associated with the Stark effect. This mechanism is analogous to the Stern-Gerlach effect, where particles with magnetic moments are deflected by inhomogeneous magnetic fields based on their spin states.

The use of state-dependent accelerations introduces a coupling between the internal and external degrees of freedom of the atoms. This coupling allows for the implementation of interferometry schemes where the phase accumulation depends on both internal state dynamics and external motion. Specifically, when Rydberg atoms traverse an inhomogeneous electric field, the differential accelerations between states lead to spatially separated paths, enabling the observation of interference effects that are sensitive to both internal state transitions and external forces.

However, practical implementations of such interferometers with neutral atoms have historically faced challenges, notably the Humpty-Dumpty effect [111]. This effect refers to the difficulty in maintaining coherence due to the dispersion of atomic wave packets under inhomogeneous forces. The spatial separation of the internal states can lead to which-path information becoming accessible to the environment, resulting in decoherence and the degradation of interference patterns.

Modern experimental techniques have addressed these challenges by utilizing precise control over electric fields and employing methods to preserve coherence. Palmer and Hogan here at UCL have recently demonstrated matter-wave interferometers using electric field gradients acting on highly excited Rydberg states of helium [41]. They performed a half-loop interferometer experiment using circular Rydberg states, where the primary phase shifts were due to the Stark effect rather than inertial effects. Although non-adiabatic transition losses limited the experiment, their work demonstrated the feasibility of using Rydberg atoms and electric fields to manipulate atomic trajectories in interferometry schemes.

In subsequent experiments, that are detailed in Chapter 6, we replicated the interferometry scheme of Palmer and Hogan using low angular momentum (ℓ) Rydberg states instead of circular states. By employing low-ℓ states, we managed to overcome the non-adiabatic transition losses that previously limited the coherence of the interferometer. The low-ℓ states experience different Stark shifts and forces compared to circular states, allowing for improved control over state-dependent accelerations.

Despite successfully mitigating non-adiabatic losses, the experiment was limited by dephasing across the atomic beam due to residual in-

homogeneities in the electric field and variations in atomic velocities. This dephasing led to a reduction in the contrast of the interference fringes, highlighting the need for precise control over both the atomic ensemble and the external fields.

The coupling between internal and external degrees of freedom in Rydberg atom interferometry opens avenues for creating interferometers sensitive to both inertial effects and internal state dynamics. In Chapter 7, we explore interferometry schemes that exploit this coupling via the motional Stark shift. The motional Stark shift arises when atoms move through an electric field, leading to velocity-dependent energy shifts in the internal states. By designing interferometry sequences that utilize these shifts, we can create interferometers that are sensitive to both inertial forces (through external motion) and potential energy differences (through internal state transitions).

This approach allows us to probe effects that are inaccessible to ground-state atom interferometers or traditional internal-state interferometers. By carefully controlling the electric fields and the interferometry sequence, we can achieve precise measurements while mitigating the effects of environmental noise and decoherence. Understanding the interplay between internal and external dynamics in Rydberg atoms is crucial for advancing the capabilities of atom interferometry and exploring fundamental quantum phenomena.

5.4 Modelling a Rydberg-atom interferometer

5.4.1 Atom interferometers near the classical limit

Matter-wave interferometry differs fundamentally from optical interferometry due to the quantum nature of atoms, which exhibit both wave-like and particle-like properties. Calculations of the phase difference in a matter-wave interferometer is more complex because multiple contributing factors must be considered, such as kinetic and potential energies, and interactions with external fields.

In optical interferometry, the phase difference $\Delta\phi$ between two paths is directly related to the optical path length difference ΔL and the refractive index n by $\Delta\phi = kn\Delta L$, where $k = 2\pi/\lambda$ is the wave number of the light with wavelength λ. In matter-wave interferometry, however, the phase difference arises from the difference in action S along the paths, given by the integral of the Lagrangian $\mathcal{L}$:

$$S = \int_{t_0}^{t_f} \mathcal{L}(x, \dot{x}, t)\, dt, \tag{5.4}$$

where t_0 and t_f are the initial and final times of the interferometry sequence, x is the position, and $\dot{x}$ is the velocity of the atom.

Different techniques for calculating the difference in action between paths include Wigner function methods [112] and representation-free approaches based on the Feynman path integral [113]. In this thesis, we adopt a semi-classical approach based on the Feynman path integral. This is valid when the action satisfies $S \gg \hbar$, where $\hbar$ is the reduced Planck constant.

In the semi-classical approximation, the evolution of the atomic wave packet is determined by the expectation values of position $\langle \hat{x} \rangle$ and momentum $\langle \hat{p} \rangle$, which follow classical trajectories. The time evolution of these expectation values is governed by Ehrenfest's theorem:

$$\begin{aligned} \frac{d}{dt}\langle \hat{x} \rangle &= \frac{\langle \hat{p} \rangle}{m}, \\ \frac{d}{dt}\langle \hat{p} \rangle &= -\left\langle \frac{\partial \hat{H}}{\partial \hat{x}} \right\rangle, \end{aligned} \tag{5.5}$$

where m is the mass of the atom, $\hat{H}(\hat{x}, \hat{p}, t)$ is the Hamiltonian operator, and the angle brackets denote expectation values.

These equations are analogous to Hamilton's equations in classical mechanics, describing the motion of a classical particle under the influence of a potential. This approximation holds when variations in the Hamiltonian are small over the spatial extent of the atomic wave packet, ensuring that all components acquire the same phase shift within the experimental sensitivity.

The semi-classical approach remains valid even for interferometers with macroscopic arm separations (up to half a meter) and long interrogation times (on the order of seconds) [98]. Within this approximation, the total phase difference $\Delta\phi$ acquired in an interferometer can be expressed as the sum of three terms [114]:

$$\Delta\phi = \phi_{\text{laser}} + \phi_{\text{prop}} + \phi_{\text{sep}}. \tag{5.6}$$

The term ϕ_{laser} is the phase difference acquired due to interactions with the control pulses. This phase is significant in optical interferometers where lasers with wavelengths in the 400–800 nm range act as rulers, but it is negligible in our microwave-driven Rydberg interferometer, because the wavelengths involved are much larger than the spatial separations of the atomic states.

The propagation phase ϕ_{prop} contains the difference in action between the two arms of the interferometer. It is given by:

$$\phi_{\text{prop}} = \frac{1}{\hbar}\left(S_1 - S_2\right) = \frac{1}{\hbar}\left(\int_{t_0}^{t_f} \mathcal{L}_1(t)\, dt - \int_{t_0}^{t_f} \mathcal{L}_2(t)\, dt\right), \tag{5.7}$$

where the subscripts 1 and 2 label the two arms of the interferometer, and $\mathcal{L}_i(t)$ is the Lagrangian for arm i, defined as:

$$\mathcal{L}_i(t) = \frac{1}{2} m \langle \dot{x}_i(t) \rangle^2 - W_i(t). \tag{5.8}$$

Here, $\langle \dot{x}_i(t) \rangle$ is the velocity along arm i, and $W_i(t)$ is the potential energy, which may depend on the internal state $|n_i, \ell_i, m_{\ell_i}\rangle$ and position $\langle x_i(t) \rangle$. The potential energy $W_i(t)$ includes any Stark or Zeeman shifts due to electromagnetic fields at the atom's location.

The separation phase ϕ_{sep} is proportional to the separation between the two arms at the time of the final beam splitter and is given by:

$$\phi_{\text{sep}} = \frac{1}{\hbar}\left(\frac{\langle p_1(t_f) \rangle + \langle p_2(t_f) \rangle}{2}\right)\left(\langle x_2(t_f) \rangle - \langle x_1(t_f) \rangle\right). \tag{5.9}$$

This phase term disappears for a closed-loop interferometer where the paths recombine perfectly at the final beam splitter ($\langle x_1(t_f)\rangle = \langle x_2(t_f)\rangle$). However, it must be considered in interferometers where the paths do not fully recombine, such as the half-loop interferometer discussed in Chapter 6.

5.4.2 Ramsey-Hahn Rydberg atom interferometry

The experiments in Chapters 6 and 7 utilize a Ramsey-Hahn type interferometry scheme with Rydberg atoms. In this scheme, two Rydberg states $|n_1\rangle$ and $|n_2\rangle$ form a pseudo-spin system manipulated using resonant microwave pulses. In all interferometric experiments demonstrated in this thesis the $|56s\rangle$ and $|57s\rangle$ states are used. Time-dependent static electric fields are applied which modify the internal energies of the states and may induce forces. In total three microwave pulses with durations $\pi/2$, π and $\pi/2$ are applied to coherently control the atom.

At time $t = 0$, considered to be immediately after a first $\pi/2$ pulse, an atom in the interferometer is in the state,

$$|\psi(t=0)\rangle \quad = \quad \frac{1}{\sqrt{2}}\big[|n_1(0)\rangle|p_1(0)\rangle + |n_2(0)\rangle|p_2(0)\rangle\big], \qquad (5.10)$$

where $|n_i(t)\rangle$ and $|p_i(t)\rangle$ represent the internal Rydberg state with principal quantum number n, and the external momentum state in arm i, respectively. After a time t', the state of the atom evolves to

$$|\psi(t=t')\rangle = \frac{1}{\sqrt{2}}\big[\mathrm{e}^{-i\phi_1(t')}|n_1(t')\rangle|p_1(t')\rangle + \mathrm{e}^{-i\phi_2(t')}|n_2(t')\rangle|p_2(t')\rangle\big], \qquad (5.11)$$

where ϕ_i is the phase accumulated in arm i and is given by $\phi_i = \int_0^{t'} \mathcal{L}_i(t,n)dt$, where the Lagrangian is a function of the internal state of the arm.

At time $t = t_\pi$, the internal Rydberg-state population is inverted upon the application of a π rotation on the Bloch sphere.

$$n_1(t) \quad = \quad \begin{cases} 56, & 0 \le t < t_\pi + T_\pi/2 \\ \\ 57, & t_\pi + T_\pi/2 \le t < t_\mathrm{f}, \end{cases}$$

and

$$n_2(t) \quad = \quad \begin{cases} 57, & 0 \le t < t_\pi + T_\pi/2 \\ \\ 56, & t_\pi + T_\pi/2 \le t < t_\mathrm{f}. \end{cases}$$

After the application of the second electric field pulse, the interferometry sequence is completed at time $t = t_\mathrm{f}$, with a final $\pi/2$ rotation of the internal Rydberg state population on the Bloch sphere. This final $\pi/2$ pulse leads to a superposition of each internal Rydberg state with each of the final momentum states such that

$$\begin{aligned} |\psi(t=t_\mathrm{f})\rangle \quad = \quad & \frac{1}{2}\Big\{\mathrm{e}^{-i\phi_1(t_\mathrm{f})}\left[|56\rangle + |57\rangle\right]|p_1(t_\mathrm{f})\rangle + \ldots \\ & \mathrm{e}^{-i\phi_2(t_\mathrm{f})}\left[|56\rangle - |57\rangle\right]|p_2(t_\mathrm{f})\rangle\Big\}. \end{aligned} \qquad (5.12)$$

Rydberg state-selective detection, implemented in the experiments by pulsed electric field ionization, was realised in the calculations by the application of the measurement operator $\hat{M} = |n\rangle\langle n| \otimes \mathbb{I}$, where $\mathbb{I}$ is the identity over momentum states.

The probability of finding the atom in state $|56s\rangle$ is given by:

$$P_{56s} = |\langle 56s|\psi(t = t_f)\rangle|^2 = \frac{1}{2}\left[1 + \cos\left(\Delta\phi\right)\right]. \tag{5.13}$$

Similarly, the probability of finding it in state $|57s\rangle$ is:

$$P_{57s} = |\langle 57s|\psi(t = t_f)\rangle|^2 = \frac{1}{2}\left[1 - \cos\left(\Delta\phi\right)\right]. \tag{5.14}$$

Here we have $\Delta\phi_{\mathrm{tot}}(t_{\mathrm{f}}) = \phi_2(t_{\mathrm{f}}) - \phi_1(t_{\mathrm{f}}) + \phi_{\mathrm{rm}}$, which is the total phase difference between the two arms, making sure to include the separation phase. The contrast C reflects the spatial overlap of the wavepackets in each arm of the interferometer at time t_{f}, i.e., $\langle p_1(t_{\mathrm{f}})|p_2(t_{\mathrm{f}})\rangle$.

$$C = \left|\left\langle \psi^{(1)}_{\mathrm{spatial}}(t_f)\middle|\psi^{(2)}_{\mathrm{spatial}}(t_f)\right\rangle\right|. \tag{5.15}$$

In our semi-classical approach, we assume $C = 1$. More comprehensive treatments that include the effects of wave packet overlap can be found in the literature [115].

In the following chapters we present results of investigations of Rydberg state interferometry, and we make use of these calculation tools.

6
Longitudinal Stern-Gerlach interferometry with low-ℓ Rydberg states

THIS CHAPTER presents results in investigations of Rydberg state interferometry with helium atoms in low-ℓ Rydberg states. This original work is published in [116]. The contents of this section have been adapted and extended from this publication.

6.1 Background

For atoms or molecules prepared in coherent superpositions of Rydberg states with different static electric dipole moments, or static electric dipole polarizabilities, the methods of Rydberg-Stark deceleration can be exploited to generate coherent superpositions of momentum states for Rydberg state interferometry. This type of electric Rydberg-atom interferometry was first demonstrated for atoms prepared in coherent superpositions of circular Rydberg states [41].

Circular Rydberg states have long fluorescence lifetimes, and pairs of circular states that differ in their value of the principal quantum number n, by 1 can act as quasi-two-level systems with long coherence times and strong single-photon electric dipole transitions at microwave frequencies. However, the non-adiabatic evolution of these states in the fast-pulsed electric fields applied for interferometry imposes limitations on the achievable displacement of the momentum components for which interference fringes can be observed.

This chapter presents results of experiments in which these limitations are circumvented through the use of atoms in superpositions of low-ℓ states. This has allowed for the observation of the coherent evolution of atomic momentum components with displacements of up to 0.75 nm, i.e., ~ 5 times larger than in previous experiments with circular Rydberg states. This provides evidence for the viability of matter-wave interferometery with Rydberg states.

The dimensions of the atoms used in these experiments, as given by the spatial extent of the Rydberg electron charge distribution, are ~ 500 nm. These exhibit induced electric dipole moments of up to 9450 D. These large dimensions and electric dipole moments offer opportunities for tests of quantum mechanics through studies of decoherence and wave-function collapse.

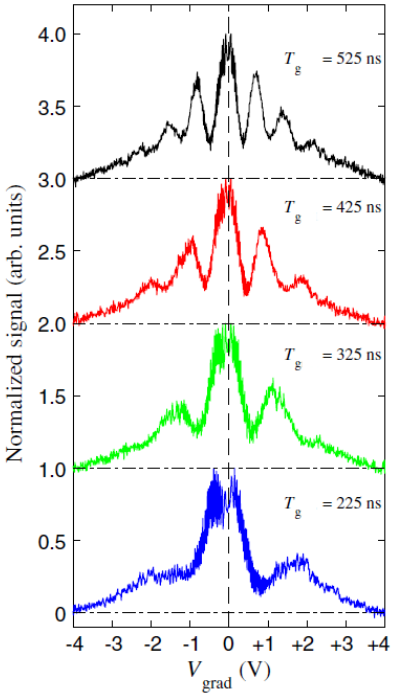

Figure 6.1: Interference fringes obtained in Stern-Gerlach type interferometery experiments with circular Rydberg states of triplet helium. The primary loss of signal as the voltage is increased is from non-adiabatic losses. The figure shows the loss of population as the time τ_g to ramp up the voltage to V_{grad} is decreased. Experiments in this section aim to overcome these non-adiabatic losses by using low-ℓ Rydberg states. Figure taken from [41].

These experiments implement a half-loop scheme in which the momentum states are coherently split, but are not fully brought back together. The idealised case of this is shown in Figure 6.2. The two paths return to the same velocity at the end of the scheme, but with a constant separation. This configuration limits the sensitivity of the interferometer to inertial forces due to the separation phase cancelling the phase accumulated by the kinetic energy [117][114]. The phases seen in our scheme are instead primarily the result of the Stark phases accumulated by the atoms as they pass through the region of inhomogenous electric field.

The experiments explore the challenges associated with performing matter-wave interferometery in supersonic beams of Rydberg states. These challenges include, maintaining coherence between superpositions of Rydberg states in the presence of force generating electric-field gradients, and understanding and controlling the de-phasing across a beam of atoms due to the finite temperature of the beam and inhomogeneities in the apparatus. Understanding and mitigating such challenges will be required to eventually implement a full-loop scheme where the spatial path of the two arms are recombined.

The realisation of such a closed full-loop interferometer would allow for sensitivity to inertial effects via the Kennard phase [118]. This phase is accumulated due to the acceleration of the atomic paths and is strongly dependent on the period of time, $\Delta\phi \propto T^3$, over which the interferometry scheme is implemented [115], [119].

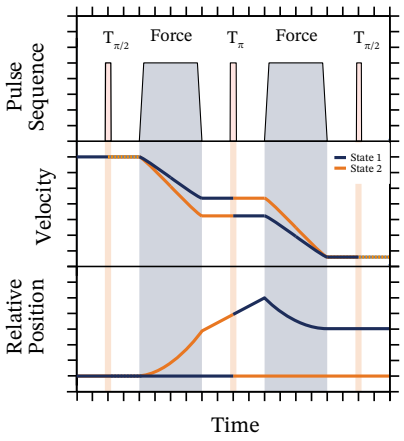

Figure 6.2: Idealised half-loop Stern-Gerlach type interferometer. Two periods of constant acceleration separated by a pulse π. This configuration results in the two paths travelling at the same velocity but with a constant separation.

6.2 Experimental procedure

A schematic diagram of the experimental apparatus is shown in Fig 6.3(a).

The excitation and interferometry region occur between a pair of copper electrodes labelled E1 and E2 in Figure 6.3(a). These electrodes were 70 mm wide and 105 mm long in the dimensions x and z, respectively, and orientated in a wedge configuration that increases linearly along the beam path. At the end closest to (furthest from) the skimmer, they were separated in the y dimension by 11.5 mm (29.7 mm).

Between E1 and E2 the atoms were excited to the 1s56s ^{3}S$_1$ ($|56s\rangle$) Rydberg level using the 1s2s ^{3}S$_1$ $\rightarrow$ 1s3p ^{3}P$_2$ $\rightarrow$ 1s56s ^{3}S$_1$ two-color two-photon laser photoexcitation scheme [68]. This was driven by co-propagating CW laser radiation at wavelengths of $\lambda_{\mathrm{UV}} = 388.975$ nm and $\lambda_{\mathrm{IR}} = 786.736$ nm for each step, respectively.

After laser photoexcitation, the Rydberg atoms were subjected to a $\pi/2{-}\pi{-}\pi/2$ Hahn-echo sequence of microwave pulses which coherently transferred population between the $|56s\rangle$ and 1s57s ^{3}S$_1$ ($|57s\rangle$) levels. The $|56s\rangle \rightarrow |57s\rangle$ transition was driven on resonance as a single-colour two-photon transition at a microwave frequency of $\omega_{56s\,57s}/2 = 2\pi \times 18.530\,975$ GHz. In the time intervals between the microwave pulses, pulsed voltages were applied to E1 to generate spatially inhomogeneous electric fields at the position of the atoms and exert state-dependent forces on them.

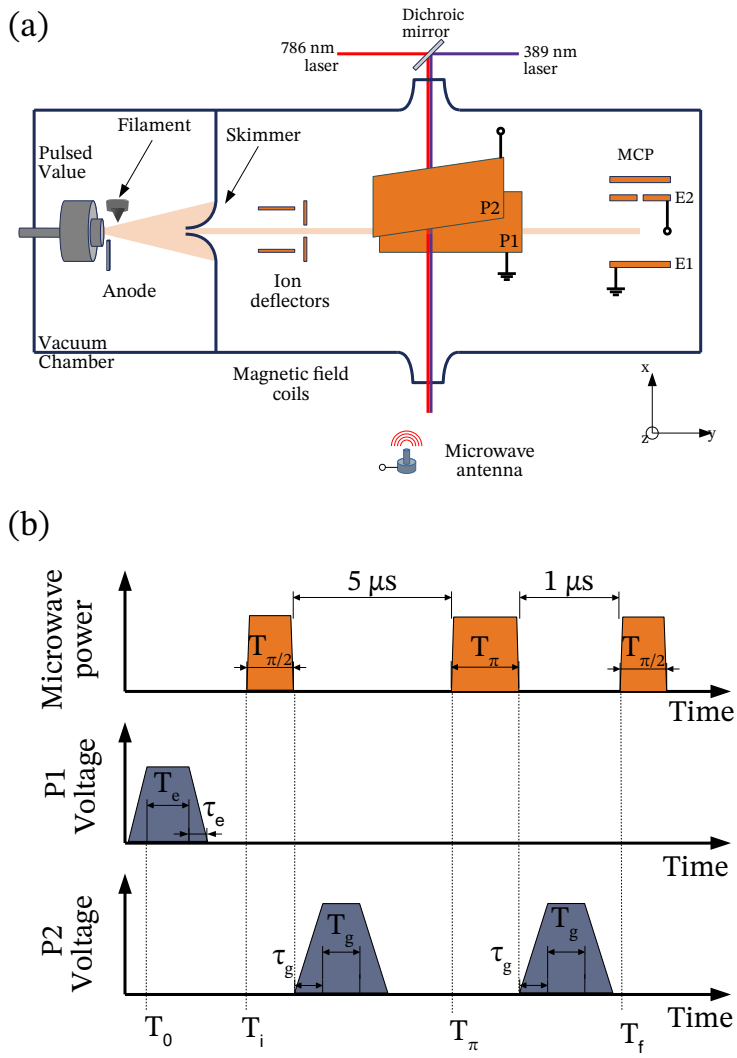

Figure 6.3: (a) Schematic of the experimental apparatus showing the wedge shaped plates in the longitudinal direction of the beam. (b) Sequence of microwave and voltage pulses applied to perform electric Rydberg-atom interferometry.

The complete sequence of microwave and voltage pulses employed in the experiments is depicted in Figure 6.3(b). At the time t_0, a pulsed potential was applied to E2 to tune the atoms into resonance with the frequency-stabilised laser beams and populated the $|56s\rangle$ level. This pulsed potential had a rise time $\tau_e = 370$ ns and was maintained at its maximal amplitude for a time T_e during which the atoms were excited.

The value of T_e determined the spatial extent of the ensemble of Rydberg atoms excited in the z dimension. T_e was set to either 800 or 1800 ns, such that the excited ensemble was prepared with a length in the y dimension of $\sim v_0 T_e \simeq 1.6$ or $\simeq 3.6$ mm, respectively. This gave a controllable parameter to test the effect of dephasing on the interference fringes.

To implement the interferometry scheme, at time $t_0 + t_d$, where $t_d \simeq 2400$ ns, a first $\pi/2$ pulse of microwave radiation, tuned to resonance with the two-photon $|56s\rangle \rightarrow |57s\rangle$ transition, was applied for a time

$T_{\pi/2} \simeq 150$ ns. Following the application of this first $\pi/2$ pulse, to prepare the atoms in an equal amplitude coherent superposition of Rydberg states, a first electric-field gradient pulse was generated at the position of the atoms by applying a pulsed potential with amplitude V_{grad} to E2.

This pulsed potential had rise and fall times $\tau_{\mathrm{g}} = 130$ ns, and a duration T_{g}. After V_{grad} was switched back to 0 V, the π pulse in the Hahn-echo sequence was applied at the time $t_0 + t_{\mathrm{d}} + T_{\pi/2} + 5000$ ns. This pulse had a duration $T_\pi \simeq 2T_{\pi/2}$ and was followed by a second electric-field gradient pulse with identical values of V_{grad}, τ_{g} and T_{g} to the first. A final $\pi/2$ microwave pulse was applied 1000 ns after the π pulse to complete the interferometry sequence.

In ideal conditions, the microwave pulses would be equally spaced rather than the asymmetric 5 μs and 1 μs that were used in the experiment. This would allow for a better cancellation of spurious phases due to stray fields. However, the purity of the microwave field constrained the positions within the wedge where a good coherence of the Rabi pulses could be achieved. Furthermore, the primary aim of this experiment of proving the coherence of low-ℓ Rydberg states for interferometery schemes the purity of the Rabi pulses was prioritised.

After applying the final $\pi/2$ microwave pulse, the atoms travelled for ~ 60 μs to the detection region in the apparatus between E3 and E4. A slowly-rising pulsed potential was then applied to E3, while E4 was maintained at 0 V to generate a time-dependent electric field that ionised the Rydberg atoms. The resulting electrons were collected on an MCP detector.

6.3 Numerical model

To model the experiments presented in this chapter, we perform numerical simulations using the semi-classical approach outlined above. The simulations aim to capture the dephasing across the atomic beam. This is achieved by simultaneously simulating a bunch of atoms and calculating the averaged probability across the bunch.

The simulation begins with the initialization of an ensemble of atoms, with position and velocity distributions matching those of the experimental atomic beam. The initial positions $y(t_i)$ and velocities $\dot{y}(t_i)$ are sampled from probability distributions representing the spatial and momentum spreads. The velocities are sampled from a Gaussian distribution where $\dot{y}(t_i) = 2000 \pm 50$ m/s.

The propagation distance of the atoms during the excitation time T_{e} was significant, i.e., ($v_0\, T_{\mathrm{e}} > 1$ mm), compared to the waist of the focused laser beams used for Rydberg state photoexcitation (~ 100 μm FWHM). So, the initial longitudinal position of each atom at the time $t = T_{\mathrm{i}}$ of the first $\pi/2$ microwave pulse of the interferometry sequence was generated by random sampling from a uniform distribution of excitation times between $t = 0$ and $t = T_{\mathrm{e}}$.

This gave $y(t_i) = y_{\mathrm{laser}} + \dot{y}(t_i - t_e)$. Here t_e is the excitation time of the atom and is sampled from a uniform distribution between $0 <$

ℓ	$\delta_{56\ell}$	$\delta_{57\ell}$
0	0.296 6669	0.296 6665
1	0.068 3553	0.068 3554
2	0.002 8896	0.002 8897
3	0.000 4469	0.000 4469
4	0.000 1269	0.000 1269
5	0.000 0486	0.000 0486
6	0.000 0230	0.000 0230

Table 6.1: Quantum defects, $\delta_{n\ell}$, of the triplet Rydberg states in helium with $n = 56$ and 57. The defects are calculated from theoretical terms using a Ritz expansion [120]. These theoretical defects in Helium are in excellent agreement with experimental observations [49].

$t < T_e$. The position of the laser within the wedge is given by $y_{\text{laser}} = 3.5 \pm 0.5$ cm.

At time t_i, each atom is prepared in the initial Rydberg state $\frac{1}{\sqrt{2}}(|56s\rangle + |57s\rangle)$. The time evolution is simulated over discrete time steps δt using the Runge-Kutta algorithm. At each time step, we compute the forces acting on the atoms, and phases due to external electric fields. The force on an atom in internal state $|n_i\rangle$ is given by:

$$F_{n_i}(t) = -\frac{\partial}{\partial y} W_{n_i}\left(y_i(t), t\right), \tag{6.1}$$

where W_{n_i} is the state dependent potential energy for state $n_i = 56s/57s$, and $\frac{\partial}{\partial y} W_{n_i}$ is the spatial gradient of the potential energy.

In the wedge-shaped electrode structure used to generate the inhomogeneous electric fields here [see Figure 6.3(a)], the electric field, $E(y,t)$, on the axis of propagation of the atomic beam is

$$E(t,y) = \frac{V(t)}{d(y)} + \mathcal{F}(y - y_{\text{cancel}}) \tag{6.2}$$

where $V(t)$ is the applied voltage and $d(y)$ is the separation of the plates at the location of the atom. $\mathcal{F}(y - y_{\text{cancel}}$ represents a residual position-dependent stray electric field in the apparatus. This stray field is included to account for the stray fields due to the electrode surfaces.

The $|56s\rangle$ and $|57s\rangle$ states used in the experiments have fluorescence lifetimes in excess of 130 μs, The electric dipole polarizabilities, and more generally, the complete Stark shifts of these levels, which were used in all interferometry calculations, were obtained from the eigenvalues of the Hamiltonian matrix for the atom in the presence of an electric field as shown in Figure 6.4. The Hamiltonian was diagonalised at 1000 field strengths between 0 and 2.9 V/cm and stored in a lookup table to be linearly interpolated in the simulations. The quantum defects for the triplet states with $\ell \leq 6$ are given in Table 6.1.

The positions and velocities are updated according to,

$$\begin{aligned} \dot{y}_i(t+\delta t) &= \dot{y}_i(t) + \frac{F_{n_i}(t)}{m}\delta t, \\ y_i(t+\delta t) &= y_i(t) + \dot{y}_i(t)\delta t. \end{aligned} \tag{6.3}$$

Where the force in the y direction is updated at each time step from the potential energy of each state. The index i accounts for the two paths through the interferometer.

The propagation phase $\phi_i(t)$ is updated at each time step using the Lagrangian:

$$\phi_i(t+\delta t) = \phi_i(t) + \frac{1}{\hbar}\left(\frac{1}{2}m\dot{y}_i(t)^2 - W_n(t)\,(y_i(t),t)\right)\delta t. \qquad (6.4)$$

The effects of the microwave pulses are applied at the appropriate times (t_π, t_f) by updating the internal states and swapping the indices of the potentials and forces accordingly.

To account for experimental averaging, the simulation is performed over 200 atoms with initial conditions sampled from the random distributions. Variations in initial positions, velocities, and field fluctuations lead to phase dispersion, which can reduce the contrast of the interference fringes. The probabilities $P_{|56s\rangle}$ and $P_{|57s\rangle}$ are averaged over the ensemble to obtain the expected measurement outcomes.

Several assumptions are inherent in the simulations. The semi-classical approximation assumes that the atomic wave packets remain localized, and quantum dispersion effects are negligible. Decoherence mechanisms such as collisions or spontaneous emission are neglected. Control pulses are assumed to be instantaneous and perfect unless experimental imperfections are explicitly modelled. The gravitational effects may be negligible compared to electromagnetic forces and are thus ignored.

6.4 Results

With the interferometer apparatus and pulse sequence optimised as described, pairs of electric field gradient pulses with equal rise and fall times of $\tau_g = 130$ ns, and equal duration of $T_g = 72$ ns were generated by applying pulsed potentials to E1 [see Figure 6.3(a)]. By adjusting the amplitudes, V_{grad}, of these pulses interference fringes could be observed via observation of the population of the $|57s\rangle$ state.

The continuous purple curve in Figure 6.5(a) shows the results of such a measurement. The interference fringes seen in this figure reflect the change in the total phase difference between the interferometer arms, $\Delta\phi_{\text{tot}}(t_f)$, as V_{grad} was adjusted. The reduction in the period of the fringes as $|V_{\text{grad}}|$ increases is a consequence of the quadratic Stark shifts of the $|56s\rangle$ and $|57s\rangle$ states.

For all values of V_{grad} in this figure, the electric field experienced by the atoms remained below the Inglis-Teller field in which the $|57s\rangle$ state crosses the manifolds of ℓ-mixed hydrogenic Stark states in Figure 6.4. Up to ~ 15 interference fringes are observed for values of $V_{\text{grad}} < 0$.

For previous experiments performed with circular Rydberg states [41], non-adiabatic transitions between internal states caused by the fast switching of the gradient fields limited maximal atomic wavepacket displacements, before being limited by population loss. These non-adiabatic dynamics led to a loss of population, and hence a loss of signal, from the quasi-two-level system composed of the pair of circular states as the value of $|V_{\text{grad}}|$ was increased.

It is evident from the convergence of the $|57s\rangle$ population in Figure 6.5(a) toward 0.5 for values of $|V_{\text{grad}}|$ close to 4.25 V that these

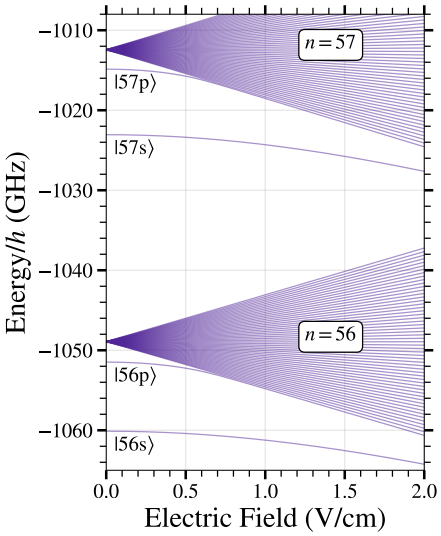

Figure 6.4: Energy level structure of the triplet Rydberg states in helium with $n = 56$ and 57.

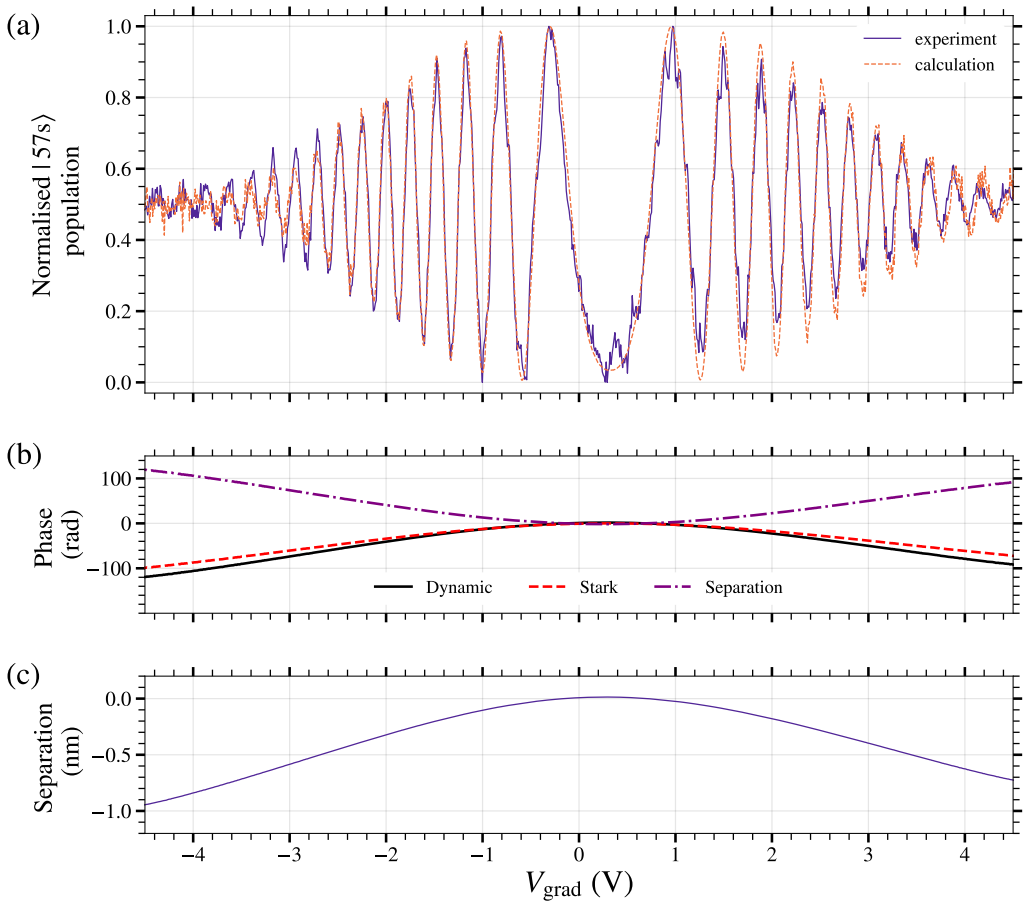

Figure 6.5: (a) Measured (continuous curve) and calculated (dashed curve) Rydberg-atom interference pattern for $T_{\mathrm{g}} = 72$ ns and $\tau_{\mathrm{g}} = 130$ ns. The parameter V_{grad} indicated on the horizontal axis represents the amplitude of the pulsed potentials applied to electrode E1 to generate the pulsed electric field gradients in the interferometer (see text for details). (b) The calculated dynamic, $\Delta\phi_{\mathrm{dynamic}}(t_{\mathrm{f}})$, (continuous black curve), Stark, $\Delta\phi_{\mathrm{Stark}}(t_{\mathrm{f}})$, (dashed orange curve), and separation, $\Delta\phi_{\mathrm{separation}}(t_{\mathrm{f}})$, (dash-dotted purple curve) phase differences at the interferometer output that contribute to the interference pattern in (a). (c) The corresponding calculated spatial separation between the classical paths of least action at the interferometer output.

non-adiabatic losses do not occur in the present experiments. This is because the $|ns\rangle$ Rydberg states remain energetically isolated from all other higher-ℓ Rydberg states over the full range of electric fields experienced by the atoms during the interferometry sequence.

The contrast decreases at higher values of $|V_{\mathrm{grad}}|$, and the mechanism leading to this is dispersion in the phase across a beam of atoms, not population loss from the $|56\rangle$ and $|57\rangle$ states. Comparison of the interferogram in Figure 6.5(a) with the results of the calculations demonstrates this. This decoherence directly reflects the phase space properties of the ensemble of Rydberg atoms, i.e., the longitudinal velocity spread and the spatial extent in the y dimension.

To account for the offset of the centroid of the interferogram to $V_{\mathrm{grad}} \simeq +0.4$ V, the residual stray electric field, $\mathcal{F}(z)$ in Equation 6.2, is required to have a non zero gradient. The cancellation of the average stray field in the experiment is not commensurate with the minimisation of the field gradient, to which the Rydberg-atom interferometer is sensitive. The calculated interference pattern in Figure 6.5(a) was

obtained by fitting a stray electric field gradient of $d\mathcal{F}_{stray}/dz = -22.5$ mV/cm^2.

This stray field gradient is the cause of the more rapid phase accumulation for $V_{grad} < 0$ than for $V_{grad} > 0$ in the experimental data. The individual contributions from the dynamic, Stark and separation phase differences to $\Delta\phi_{tot}(t_f)$ in the calculated interferogram are displayed in Figure 6.5(b).

The dynamic phase accumulated due to the kinetic energy of the two paths perfectly cancels with the separation introduced to account for the semi-classical model used to describe the half-loop interferometer. The remaining phase is therefore the Stark phase accumulated as the atoms are exposed to different electric fields during each of the two force pulses.

Microwave spectroscopy of Rydberg-Rydberg transitions allows for a confirmation of the magnitude of the stray field gradient. The longitudinal profile of the stray field was determined by performing this at selected times after the laser photoexcitation. These spectra of the two-photon $|56s\rangle \rightarrow |57s\rangle$ transition were recorded using single pulses of microwave radiation with durations of 2 μs and are displayed in Figure 6.6.

The absolute transition frequencies in these measurements are affected by Doppler shifts in the fast-moving pulsed supersonic beam, on the order of +100 kHz. However, across this set of spectra, the measured two-photon transition frequency shifts by $\sim +60$ kHz. The $|56s\rangle \rightarrow |57s\rangle$ transition exhibits a quadratic Stark shift toward lower frequency with increasing electric field strength.

The observed shift toward higher transition frequencies at later times after laser photoexcitation indicates that the uncompensated stray electric field between E1 and E2 reduces toward the end of these electrodes closest to the detection region. At that end, the separation between the electrodes in the y-dimension is greatest, and the atoms are furthest from the electrode surfaces and the source of residual stray fields [121], [122].

Comparison of the experimentally measured transition frequencies in Figure 6.6 with the calculated Stark shifts of the $|56s\rangle$ and $|57s\rangle$ states yielded a mean residual uncompensated stray field gradient between E1 and E2, on the axis of propagation of the atomic beam, of $d\mathcal{F}_{stray}/dz \simeq -20 \pm 5$ mV/cm^2. This is consistent with the residual gradient of -22.5 mV/cm^2 obtained by comparing the measured and calculated interference patterns in Figure 6.5.

In performing the numerical simulations of our experiments, our primary objective was not to produce precise quantitative predictions of the interference patterns. Instead, the simulations were designed to explore the impact of dephasing mechanisms on the observed interference fringes, particularly at higher voltages where dephasing effects become more pronounced.

To achieve this, we fitted the simulations to the experimental data presented in the main figure (Figure 6.5), where dephasing is minimal at low values of V_{grad} and the coherence of the atomic ensem-

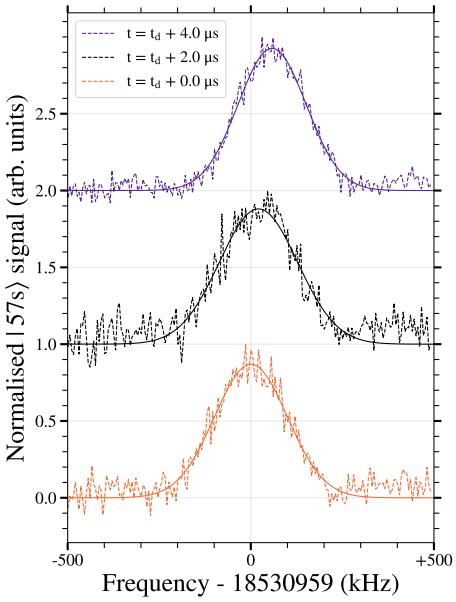

Figure 6.6: Microwave spectra of the two photon $|56s\rangle \rightarrow |57s\rangle$ transition recorded at times t_d, $t_d + 2.0$ μs, and $t_d + 4.0$ μs after laser photoexcitation, to probe residual uncompensated stray electric field gradients over a distance of $\sim$ 8 mm along the axis of propagation of the atomic beam between E1 and E2.

ble is well maintained. By adjusting parameters within their experimental uncertainties—such as the residual stray electric field gradient $\mathrm{d}\mathcal{F}_{\mathrm{stray}}/\mathrm{d}y$, the initial longitudinal velocity spread Δv_y, and the spatial extent of the Rydberg atom ensemble $L\mathrm{Ry}$—we obtained a good agreement between the simulations and the experimental data at low voltages in Figure 6.5. These parameters were set to $\dot{y} = 2000 \pm 50, \mathrm{m/s}$, $y_{\mathrm{laser}} = 35 \pm 5, \mathrm{mm}$, $\mathrm{d}\mathcal{F}_{\mathrm{stray}}/\mathrm{d}y = -20 \pm 5, \mathrm{mV/cm}^2$, and $\mathcal{F}0 = y\mathrm{laser} \pm 1, \mathrm{mm}$.

With these parameters established and kept fixed, we then varied experimental parameters such as the excitation time T_e and the electric field gradient pulse duration T_g to see how well the simulations captured the dephasing effects observed in the subsequent experiments. By maintaining the same simulation parameters, we could directly assess the influence of these experimental variations on the coherence properties of the interferometer.

The next section presents these experiments, where we systematically adjusted T_e and T_g to investigate their impact on interference fringe contrast. Comparing the experimental results with the simulations using the fixed parameters allowed us to observe how dephasing arising from factors such as the increased spatial extent of the atomic ensemble and prolonged exposure to inhomogeneous electric fields affects the interference patterns.

This approach provides valuable insights into the coherence properties of the interferometer and the dominant sources of decoherence. By focusing on how well the simulations capture the dephasing under varying experimental conditions, we can better understand the limitations of the current interferometer setup and identify avenues for improving its performance in future experiments, without relying on exact predictions of the experimental outcomes at all voltage levels.

6.4.1 Dephasing experiments

The effect of the spatial extent of the ensemble of Rydberg atoms in the y dimension on the coherence length was investigated by adjusting the value of T_e, the laser photoexcitation pulse duration. An interferogram recorded for $T_\mathrm{e} = 800$ ns, i.e., with $L_\mathrm{Ry} \simeq 1.6$ mm, and values of $V_\mathrm{grad} \geq 0$ is displayed in Figure 6.7(a). This experiment uses the same set of parameters as Figure 6.5.

The experiment in Figure 6.7(b) was recorded with a longer photoexcitation pulse of $T_\mathrm{e} = 1\,800$ ns, i.e., with $L_\mathrm{Ry} \simeq 3.6$ mm. It is otherwise identical to Figure 6.7(a). It can be seen that for the longer bunch of atoms the contrast of the interference fringes reduces more rapidly as the value of V_grad increases, indicating a reduction in the longitudinal coherence length.

The reduction in the contrast of the interference fringes is also apparent in the results of the calculations. This is a consequence of the dependence of the electric field between E1 and E2 on the position in the y dimension, and the effect this has on the Stark phase differences within the ensemble of excited atoms.

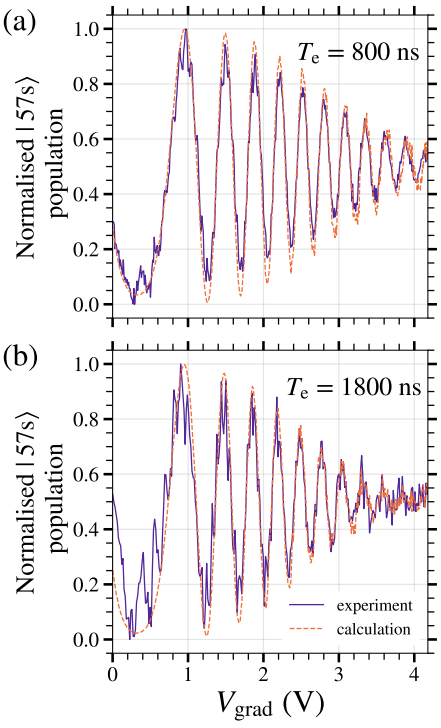

Figure 6.7: Measured (continuous purple curves) and calculated (dashed orange curves) Rydberg atom interference patterns recorded for $T_\mathrm{g} = 72$ ns, $\tau_\mathrm{g} = 130$ ns and values of $V_\mathrm{grad} \geq 0$ after laser photoexcitation of (a) a short, $L_\mathrm{Ry} \simeq 1.6$ mm, ensemble of Rydberg atoms when $T_\mathrm{e} = 800$ ns, and (b) along, $L_\mathrm{Ry} \simeq 3.6$ mm, ensemble of Rydberg atoms when $T_\mathrm{e} = 1800$ ns.

The inhomogeneity of the electric field leads to different Stark shifts and forces on atoms at the front and back of the excited ensemble. Thus the range of values of $\Delta\phi_{\rm tot}(t_{\rm f})$ accumulated across the ensemble is increased for a longer initial distribution of atoms, and increased dephasing ensues.

The rapid fluctuations, with a periodicity of ~ 0.1 V, seen across the interference pattern in Figure 6.7(b) is attributed to the spatial inhomogeneity of the microwave field and the effect this has on the fidelity of the microwave pulses across the ensemble of Rydberg atoms. Because of the inhomogeneity of this field in the y dimension, ideal $\pi/2$ and π pulses can only be implemented for compact ensembles of excited atoms that are well localized at the time of the application of each pulse.

By increasing the spatial extent of the ensemble of Rydberg atoms, the set of microwave pulses used no longer yielded ideal $\pi/2$ and π rotations on the Bloch sphere for every atom. This results in a beating effect in the final Rydberg-state population superimposed on the primary interference fringes.

Further information on decoherence in the interferometer was obtained by performing experiments with electric field gradient pulses with a fixed amplitude but increasing duration. These measurements, presented in Figure 6.8, provide insight into the increased exposure of the atoms to the interferometer's electric fields.

For these measurements, $T_{\rm e} = 800\ ns$, and data was recorded for $V_{\rm grad} = 2$ and 1 V. The results are displayed in Figure 6.8(a) and (b), respectively. The dependence of the contrast of the interference fringes in Figure 6.8 on the value of $T_{\rm g}$ is similar to that observed in the calculations.

The calculations performed do not account for decoherence that depends on the value of $V_{\rm grad}$, i.e., decoherence arising from electric field noise. The more strongly polarized atoms in Figure 6.8(a) with $V_{\rm grad} = 2$ V may be more sensitive than those in Figure 6.8(b). This suggests that decoherence caused by laboratory electric field noise does not significantly impact the performance of the interferometer over the time-scales, and for the fields and field gradients used in these experiments.

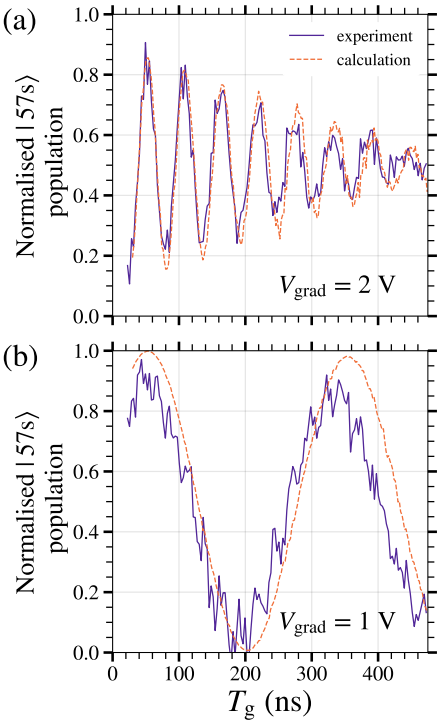

Figure 6.8: Measured (continuous blue curves) and calculated (dashed red curves) Rydberg-atom interference patterns recorded by adjusting the electric field gradient pulse duration $T_{\rm g}$, for $\tau_{\rm g} = 130$ ns, and (a) $V_{\rm grad} = 2$ V, and (b) $V_{\rm grad} = 1$ V. In each case $T_{\rm e} = 800$ ns.

6.5 Conclusions

We have performed electric Rydberg-atom interferometry with helium atoms prepared in coherent superpositions of the 1s56s,^{3}S$_1$ and 1s57s,^{3}S$_1$ low-ℓ Rydberg states. This work demonstrates a advancement over previous experiments employing circular Rydberg states, where non-adiabatic internal state dynamics led to substantial population loss and limited the achievable spatial separations of the atomic wavepackets. By utilizing low-ℓ states, we have minimized such non-adiabatic losses, allowing for the observation of interference fringes at larger momentum displacements—up to a maximal spatial separation of approximately 0.75 nm between the atomic momentum components.

A key focus of these experiments was to understand the dephasing mechanisms across the atomic beam that lead to decoherence in Rydberg-atom interferometry. Through careful comparison of experimental results with numerical simulations, we have identified that stray electric field gradients and inhomogeneities in the initial phase space distribution of the atoms are primary contributors to the degradation of interference fringe contrast due to dephasing. By investigating the effects of the spatial extent of the Rydberg atom ensemble and the duration and amplitude of the applied electric field gradients, we have gained valuable insights into how to control and mitigate these dephasing effects.

Understanding and overcoming these sources of decoherence is crucial for the development of high-fidelity matter-wave interferometers using Rydberg atoms. The improvements demonstrated here, particularly in minimizing non-adiabatic losses and characterising dephasing mechanisms, represent important steps towards the realization of a full-loop interferometer with Rydberg atoms. Such a full-loop interferometer would enable the recombination of spatially separated atomic paths, making the interferometer sensitive to inertial effects through the Kennard phase and enhancing its applicability for precision measurements.

Future work could focus on implementing strategies to further reduce stray electric field gradients, such as designing electrode configurations that keep the atoms further away from surfaces, and employing transverse geometries to exploit lower velocity spreads in the force-exerting direction. These enhancements could lead to greater control over phase dispersion across the atomic ensemble, improving the coherence length of the interferometer.

Ultimately, the ability to perform matter-wave interferometry with Rydberg atoms in a full-loop configuration opens up exciting possibilities for fundamental physics experiments. For example, measuring the acceleration of Rydberg atoms in Earth's gravitational field could provide new insights into quantum gravity effects. Extending these techniques to work with Rydberg positronium atoms could enable tests of antimatter gravity, probing fundamental symmetries in nature.

In summary, our experiments have advanced the understanding of dephasing in Rydberg-atom interferometry and demonstrated significant improvements over prior approaches using circular Rydberg states. These developments pave the way toward the realisation of full-loop matter-wave interferometers with Rydberg atoms, which show great promise for future precision measurements and fundamental tests of quantum mechanics.

7
Sensing motional-Stark phases via Rydberg states

This work is original and has not yet been published.

7.1 Background

The experiments of the previous chapter demonstrated the feasibility of implementing a full-loop Stern-Gerlach interferometer with low-ℓ Rydberg states. The dispersive nature of the dynamic kinetic and Stark phases present the next challenges that would need to be controlled for the practical implementation of such an interferometer.

Each atom in the excited bunch will have a different initial velocity; thus, even if all atoms experience the same forces, they will not experience the same phase shifts. This would make controlling the dispersive nature of a hot beam challenging. Additionally, the large sensitivity to electromagnetic fields makes any inhomogeneities within the interferometer lead to dispersive effects across the beam of Rydberg states.

This chapter presents a different approach using a different phase term arising from the motional-Stark effect. It is shown that this phase can be non-dispersive in certain configurations of external electric and magnetic fields.

The phase arises from the motion of the electric dipole through a magnetic field. In this configuration, there is a coupling between the internal dynamics and the external motion of the center-of-mass (COM) of the atom. The large electric dipole moments unique to Rydberg states make exploiting this phase possible in a way that is not realistic with ground-states of atoms.

In this chapter, we describe an experiment to coherently measure the motional-Stark phase in Rydberg. We comment on how, under specific configurations of electromagnetic potentials, the motional-Stark phase can be identified with the He–McKellar–Wilkens (HMW) geometric phase, which is a close analogue of the more famous Aharonov–Bohm phase.

The sequence of electric pulses used is identical to those in Chapter 6 except for the inversion of a voltage pulse and the presence of a homogeneous magnetic phase. This inversion has opposite effects on the static and motional Stark phases. It causes the static Stark phase to cancel but doubles the motional-Stark phase. Finally, we discuss

potential applications of this phase including a description of an interferometery sequence that could be sensitive to inertial effects without velocity dispersion.

7.2 The motional-Stark effect

The interaction of systems of particles with static electric and magnetic fields can lead to complex interactions between the center-of-mass motion of the system and their internal dynamics [123]. The interaction between the system of particles and the electromagnetic fields can modify the momentum of the particles in interesting ways.

For electrically neutral systems, all components of the pseudomomentum commute. This condition allows the system to be *pseudo-separated*. In effect, the Schrödinger equation can be reduced over only the internal coordinates, but with a parametric dependence on the eigenvalue of the *pseudo-momentum*, $\mathbf{K} = \mathbf{P} - \frac{|e|}{c}\mathbf{B} \times \mathbf{r}$ where $\mathbf{B}$ is the magnetic field, $\mathbf{r}$ is the vector between the particles and represents the dipole, and $\mathbf{P}$ is the canonical momentum.

For a neutral-atom this allows for the same solutions to the Hamiltonian as discussed in Chapter 2, except an additional term where the external motional introduces a Stark potential. In this way, the external motion of the system of particles and the internal dynamics become coupled. Exploiting this coupling to use an internal state interferometer to extract information about the external motion is the focus of this chapter.

The term that couples the internal and external dynamics is an effective electric field that is proportional to the pseudo-momentum, where the electric field experienced by the particles is

$$\mathbf{E}_{\text{tot}} = \mathbf{E} + \frac{\hbar}{Mc}\mathbf{K} \times \mathbf{B}. \tag{7.1}$$

Here $\mathbf{E}_{\text{tot}}$ is the total electric field, $\mathbf{E}$ is the external electric field and M is the mass of the dipole. This is the origin of the *motional-Stark effect*, first identified by Lamb [124] for a hydrogen atom moving in a magnetic field. This leads to the interpretation of the motional-Stark effect as being due to an additional electric field experienced by the atom in the rest frame of the COM, and hence a modified Stark shift.

7.2.1 Motional-Stark phase in crossed electric and magnetic fields

The energy shift due to the motional-Stark effect will induce a phase shift in the atom. These phases have some interesting and unique properties compared to the dynamic phases discussed in Chapter 6.

As shown previously, an atom moving in a magnetic field experiences an additional electric field due to the cross product of its velocity vector and the magnetic field, $\mathbf{E}_{\text{total}} = \mathbf{E} + \mathbf{v} \times \mathbf{B}$. The general Lagrangian for an induced electric dipole moving in external fields is given by,

$$\mathcal{L} = \frac{m}{2}\mathbf{v}^2 - \alpha\left(\mathbf{E} + \mathbf{v} \times \mathbf{B}\right)^2, \tag{7.2}$$

where the state is assumed to have a quadratic induced polarisability α, an assumption which holds for low-ℓ Rydberg states in small electric fields far below the Inglis-Teller limit.

Consider a static crossed configuration of electric and magnetic fields. The directions of the electric and magnetic fields can be taken along the $\hat{z}$ and $\hat{x}$ axes, respectively, i.e., $\mathbf{E} = (0, 0, E_z)$ and $\mathbf{B} = (B_x, 0, 0)$. To simplify the algebra, the particle is assumed to travel perpendicular to both fields, that is, $\mathbf{v} = (0, v_y, 0)$. The Lagrangian may therefore be expanded such that

$$\begin{aligned}\mathcal{L} &= \frac{m}{2}v_y^2 - \alpha\left(E_z + v_y B_x\right)^2 \\ &= \frac{m}{2}v_y^2 - \alpha\left(E_z^2 + v_y^2 B_x^2 + 2E_z v_y B_z\right) \\ &= \left(\frac{m}{2} - \alpha B_x^2\right)v_y^2 - \alpha\left(|E_z|^2 + 2E_z v_y B_x\right).\end{aligned} \tag{7.3}$$

This can be viewed as the Lagrangian for a particle with a modified mass $m' = m - 2\alpha B_y^2$, where for realistic parameters of the magnetic field, the change in mass is negligible.

For example, the $56s$ state of helium, which has a mass of 4.002 amu, has polarisability $\alpha = 2.179\,\mathrm{GHz/(V/cm)^2}$. Even in a magnetic field of 100 G, this results in a mass modified by 10^{-6} amu. The next term in the Lagrangian is the static Stark energy shift, $\alpha|E_z|^2$. This phase term is independent of the orientation of the dipole with respect to $\hat{x}$. The final term in the Lagrangian is relevant to the motional-Stark phase,

$$\mathcal{L}_{\mathrm{mS}} = -2\alpha E_z v_y B_x. \tag{7.4}$$

This is the phase term due to the motional-Stark effect. Firstly, it is proportional to the sign of E_z. Reversing the direction of the electric field will reverse the direction of the dipole and therefore the phase. Secondly, the term in the Lagrangian is proportional to the velocity v_y. This dependence results in an interesting property that can be seen by integrating the phase with respect to time. The resulting phase is proportional to the distance travelled along the $\hat{y}$ direction.

$$\begin{aligned}\phi_{\mathrm{mS}} &= \int_0^t \frac{-2\alpha E_x B_y}{\hbar} v_y\, dt \\ &= \int_0^y \frac{-2\alpha E_x B_y}{\hbar}\, dy \\ &= \frac{-2\alpha E_x B_y L}{\hbar},\end{aligned} \tag{7.5}$$

where $L = \int_0^t v_y dt$ is the total distance the atom travels in the crossed fields. The time dependence can be absorbed within an integral over a distance, which hints at the underlying geometric nature of this phase.

The properties of this phase within our apparatus will contrast with the static Stark phase. This can be seen by considering the idealised case in which an atom flies into a region defined by two plates of length L within which there is a crossed configuration of electric and magnetic fields. The static Stark phase will be proportional to the amount of time that the atom spends within the plates.

In the ideal case, this will result in a phase $\phi_{\text{stark}} = -\alpha E_z^2 t = -\alpha E_z^2 \frac{L}{v_y}$, where t is the time taken to traverse the plates. This is dispersive as a slower atom will take longer to traverse and in doing so acquire a larger phase as it spends more time with an electric field induced energy shift. The motional Stark phase however only has a dependence on the length of the region of crossed fields, and therefore no matter what speed an atom traverses the region it will acquire the same phase making it non-dispersive in velocity.

7.3 Scheme for measuring centre-of-mass velocity via the motional-Stark phase

As seen so far, the motional-Stark phase has a different structure to the static-Stark phase. These differences can be used to isolate the motional-Stark phase in an experiment using the same Ramsey-Hahn sequence of microwave and voltage pulses as performed in Chapter 6. The only difference being the need to invert one of the applied voltage pulses, thus creating a region of homogeneous electric field to cause the cancellation of the static-Stark phase.

The static Stark effect is given by $W = \alpha|E|^2$, i.e., it is only dependent on the magnitude and not the direction of the electric field. The motional-Stark effect is coupled to the direction of the electric field as this determines the direction of the induced dipole $\mathbf{d} = 2\alpha\mathbf{E}$. Inverting the direction of the applied electric field will result in reversing the sign of the motional-Stark phase but not the static Stark phase. The two arms will acquire identical static Stark phases, but non-identical motional-Stark phases.

This results in a total phase shift which is coupled to the velocity of the atom. From Equation 7.5, the motional-Stark phase acquired by a dipole in our configuration of electric and magnetic fields is proportional to the distance it travels in the y direction, $y = v_y t_p$, where v_y is the velocity in the y direction and t_d is the duration of the dipole inducing electric pulse.

The phase acquired by an atom during a period in the Ramsey-Hahn scheme, that is for states with polarisability μ_i is,

$$\phi_i = \frac{1}{\hbar}\left[\left(\frac{m}{2} - \alpha_i B_x^2\right) v_y^2 T - \alpha_i \left(E_z^2 T + 2E_z v_y B_x T\right)\right] \tag{7.6}$$

In the period after the π pulse the internal state will have changed resulting in a new polarisability α_j. The electric field direction can change direction, this is indicated by $\pm$ where $+$ corresponds to the voltage pulses both being positive and $-$ corresponds to the second pulse being negative. The resulting total phase in the arm for each case is given by,

$$\begin{aligned}\phi_{i\to j,\pm} = &\frac{1}{\hbar}\left[\left(\frac{m}{2} - \alpha_i B_x^2\right) v_y^2 T - \alpha_i \left(E_z^2 T + 2E_z v_y B_x T\right)\right] \\ &+\frac{1}{\hbar}\left[\left(\frac{m}{2} - \alpha_j B_x^2\right) v_y^2 T - \alpha_j \left(E_z^2 T \pm 2E_z v_y B_x T\right)\right].\end{aligned} \tag{7.7}$$

In the other arm of the interferometer the atom begins with α_j that swaps to α_i after the π pulse. The total phase at the end of the interferometery sequence in the second arm is $\phi_{j\to i,\pm}$. The total phase difference between the two arms will therefore be $\delta\phi = \phi_{i\to j,\pm} - \phi_{j\to i,\pm}$. From inspecting the form of the phase difference both the kinetic energy terms and the static Stark terms will cancel out leaving only,

$$\delta\phi_{\pm} = \frac{1}{\hbar}\left[(\alpha_j - \alpha_i)(2E_z v_y B_x T) \mp (\alpha_j - \alpha_i)(2E_z v_y B_x T)\right]. \tag{7.8}$$

If the two voltage pulses are oriented in the same direction the motional Stark phases will cancel. If the two voltage pulses are oriented in opposite directions the total motional-Stark phase will sum and result in,

$$\delta\phi_{-} = \frac{1}{\hbar} 4(\alpha_j - \alpha_i) E_z v_y B_x T. \tag{7.9}$$

The phase difference is proportional to the difference between the two states polarisabilities and the centre-of-mass velocity of the atom. In essence, this interferometric scheme acts as a 'speed camera' for the atom, using the coupling between the internal and external degrees of freedom to imprint a phase due to the external motion onto an internal state interferometer.

Conceptually this scheme is sensitive to inertial accelerations without requiring the generation of large forces to split the atoms into seperate paths. The basic idea can be seen in a thought experiment where an atom is placed motionless in crossed electric and magnetic fields. If there is an acceleration g and one waits a time T_{wait} before starting the interferometric sequence, then the average speed of the center-of-mass motion will be $v_0 + gT_{\text{wait}}$ at the start of the interferometer. By performing the interferometer as a function of wait-time, the effects of the acceleration would lead to an observable shift in the phase.

7.4 Connection to the He–McKellar–Wilkens phase

Geometric phases play a fundamental role in quantum mechanics, they concern the phase evolution of a system that arises solely from its geometrical properties in parameter space, independent of the dynamical evolution. This concept extends beyond the traditional dynamical phases associated with energy evolution, offering deeper insights into the topological and geometric nature of quantum systems.

7.4.1 Geometric phases

Quantum systems can acquire a geometric phase when its parameters are varied cyclically and adiabatically, causing the system to traverse a closed loop in parameter space. Unlike dynamical phases, which depend on the energy and time, geometric phases depend only on the path taken through the parameter space and the geometry of that path.

The most well-known example of a geometric phase is the Berry phase, introduced by Michael Berry in 1984. The Berry phase arises when a quantum system remains in its instantaneous eigenstate while its Hamiltonian is varied slowly around a closed loop. Mathematically, the Berry phase γ is given by the integral of the Berry connection $\mathcal{A}$ around the closed path C:

$$\gamma = \oint_C \mathcal{A} \cdot d\mathbf{R}, \tag{7.10}$$

where $\mathcal{A} = i\langle\psi(\mathbf{R})|\nabla_{\mathbf{R}}|\psi(\mathbf{R})\rangle$ and $\mathbf{R}$ represents the set of parameters defining the Hamiltonian.

7.4.2 The Aharonov–Bohm phase

A quintessential example of a geometric phase is the Aharonov–Bohm (AB) phase, predicted by Yakir Aharonov and David Bohm in 1959 [82]. The AB phase demonstrates that even in regions where the electromagnetic fields are zero, the potentials themselves can influence the quantum phase of charged particles.

Consider a charged particle, such as an electron, moving in a region devoid of both electric and magnetic fields ($\mathbf{E} = \mathbf{B} = 0$). Suppose there exists a magnetic flux Φ confined within a solenoid that the electron encircles. Although the electron does not experience a local magnetic field, the presence of the vector potential $\mathbf{A}$ outside the solenoid imparts a phase shift to the electron's wavefunction. The AB phase ϕ_{AB} is given by:

$$\phi_{\text{AB}} = \frac{e}{\hbar c} \oint_C \mathbf{A} \cdot d\mathbf{r} = \frac{e\Phi}{\hbar c}, \tag{7.11}$$

where the integral is taken around a closed loop C encircling the solenoid. This phase shift has been experimentally verified and underscores the physical significance of electromagnetic potentials in quantum mechanics, independent of the fields.

The Aharonov-Bohm phase is not the only geometric phase associated with moving particles. Soon after it was identified the Aharonov-Casher phase was theorized. This is the phase acquired by a magnetic dipole moving in an electric field. When the magnetic dipole takes a closed path around a charged wire, within specific geometric considerations (that is the particle moves so that the wire exerts no force), it can acquire a path and velocity independent phase.

The Aharonov-Casher effect was first shown in 1989 by neutron interferometry [126]. The velocity independence of the phase was verified in an atomic beam experiment in 1993 [127] using Ramsey interferometry within a modified geometry, where the atom effectively passes one way around the wire in a superposition of states with different magnetic dipole moments.

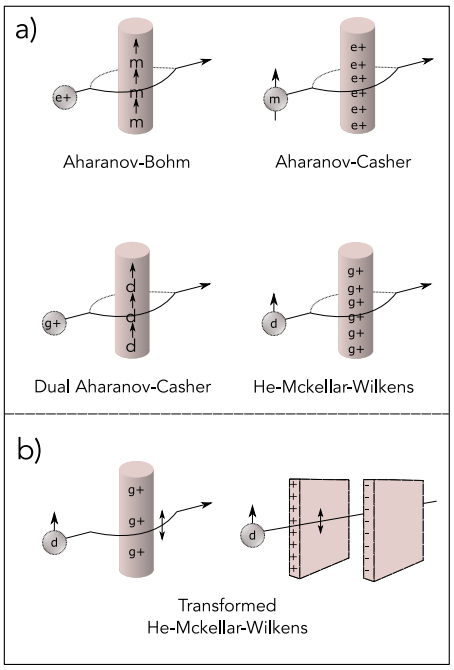

Figure 7.1: (a) Schematic showing four possible configurations to observe topological phases using electromagnetic charges and dipoles. Here, e is an electric charge, m is a magnetic dipole, g is a magnetic monopole, and d is an electric dipole. (b) Transformations of the He–McKellar–Wilkens case to account for magnetic monopoles being non-physical. Figure adapted from Ref. [125].

7.4.3 The He–McKellar–Wilkens Phase

The He–McKellar–Wilkens (HMW) phase is a geometric phase that serves as the electromagnetic dual to the Aharonov–Bohm phase and

Aharonov-Casher phases. While the AB phase arises from the interaction of a charged particle with an electromagnetic potential, and the AC phase from a magnetic dipole around a line of electric charge, the HMW phase emerges from the interaction of a neutral particle possessing a permanent electric dipole moment with magnetic monopoles.

A key difference between the HMW/AC phases and the AB phase is that while the AB phase occurs in a region without electromagnetic fields, the HMW/AC phases occur via a direction interaction between the particle and the fields. The configuration of these fields is such that they do not exert a net force on the particle, ensuring that the particle's trajectory remains unaffected by classical forces. Instead, the particle acquires a purely geometric phase.

The HMW phase is given by,

$$\phi_{\mathrm{HMW}} = \frac{1}{\hbar c^2} \oint_C (\mathbf{d} \times \mathbf{B}) \cdot d\mathbf{r}, \tag{7.12}$$

where the integrand has an identical form to that of the motional-Stark phase identified previous. In fact this connection was quickly identified [125]. The HMW phase is motivated out of considerations of electromagnetic duality from previously identified geometric phases, but physically it is the result of the motional-Stark effect. Although a phase due to the motional-Stark effect is present in any situation where an electric dipole moves through a magnetic field, the conditions required to replicate the HMW require a number of conditions on the electromagnetic potentials.

7.4.4 Experimental schemes to measure the HMW phase

Despite the absence of magnetic monopoles, experimental schemes have been proposed and implemented to measure the HMW phase by engineering specific electromagnetic field configurations that emulate the necessary line of magnetic monopole [128].

The first suggested scheme is that of Wilkens [129] in which atoms are polarised by an electric field and subjected to different magnetic fields on the two arms. The suggestion was to use a pierced sheet of ferromagnetic material. The technical difficulty of implementing this set-up resulted in this never being explored experimentally, but highlighted the feasibility of constructing the necessary field conditions.

Wei et. al. [130] suggested a set-up in which an atom interferometer is used where the two paths pass either side of a charged wire. The charged wire will induce opposite electric dipoles in the two arms and create the necessary HMW phase in the presence of a common homogenous magnetic field.

The first experimental realisation of the HMW was conducted in an experimental apparatus that took inspiration from the method of Wei et. al., and used a Mach-Zehnder interferometer. A supersonic beam of lithium atoms with a velocity of $\langle v \rangle \approx 1065$ m/s are Bragg diffracted and pass either side of a grounded septum to produce regions with opposite polarisation in the two paths [131]. This experiment produced phase shifts ϕ_{HMW} on the order of milliradians.

The authors of this study comment on how convenient it would be to use a Ramsey style interferometer [128] as it common in measurements of the Aharonov-Casher phase [127]. The difficulty with such a measurement for the HMW case is the lack of quasi-degenerate states with opposite electric dipole moment in ground-states. A method for detecting the HMW phase using excited hydrogen-like states was proposed by [125] using the quasi-degenerate $n = 2$ excited states of hydrogen.

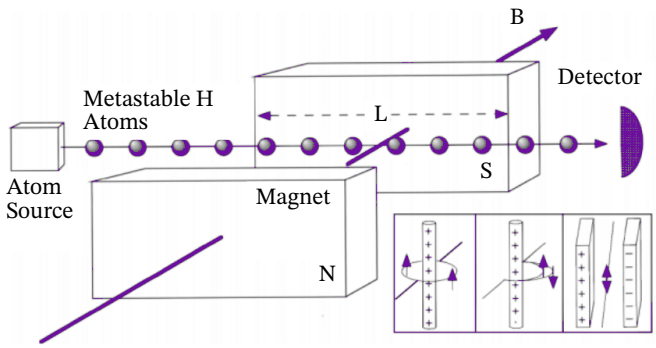

Figure 7.2: Adapted from Ref. [125]. Scheme proposed by Dowling et. al. to measure the HMW phase via Stark quenching in a metastable excited beam of Hydrogen. The inset figure shows a series of transformations that allows for the non-physical magnetic monopole field to be replaced by a constant magnetic field between two poles. The experiment in this chapter can be seen to make a similar transformation in order to measure the HMW phase.

In this scheme the magnetic field produced by a line of monopoles is replaced by a constant magnetic field. The HMW phase acquired is related to the length of the region of magnetic field, L, and given by $\phi_{\text{HMW}} = \frac{dBL}{\hbar c}$, and the dipole of the states used is given by $d = 3a_0 e$, where a_0 is the Bohr radius.

This is the same transform employed by Sangster et. al [127] in measuring the AC phase. Inset to the figure shows the steps of the transformation. The dipole moving each side of the magnetic field with the same dipole can be replaced by it traversing the same path but in opposite dipole states. The circular path along a magnetic field line can then be replaced by a linear path through a region of homogenous magnetic field. In this way the exotic conditions that demand a magnetic field generated by a line of magnetic monopoles, can be replaced by a conventional magnetic field, that can be produced by a pair of bar magnets or by a pair of Helmholtz coils.

This scheme requires hydrogen-like states which can be prepared in quasi-degenerate superpositions of opposite dipole. Our experiments use low-ℓ Rydberg states with non-zero quantum defects isolating them from the degenerate manifold of Rydberg states. A connection can be made between the two set-ups and it is possible to view our scheme, via an additional transformation, as a measurement of the difference in HMW phase of two states. The process to make this transformation is shown in Figure 7.3.

The diagram on the left hand side shows the conventional set-up of dipoles traversing a line of magnetic monopoles. In the first part of the scheme the atom traverses the monopoles in a state with dipole $d = d_{57}$. The paths then cross over and traverse an identical line of

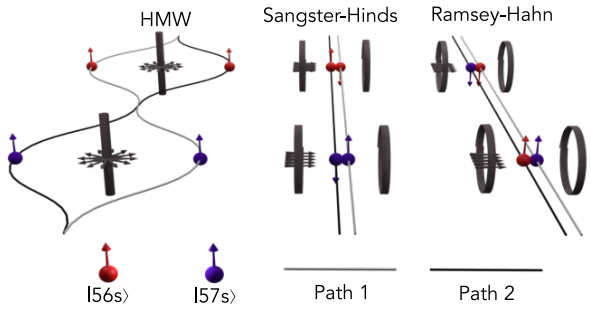

Figure 7.3: Schematic showing the transformation used in the experiment to observe motional-Stark phases. The paths of the two arms are indicated by different coloured lines. (a) Shows the paths taken by an atom in the idealized HMW configuration assuming the existence of magnetic monopoles. The atom traverses a line of monopoles in one orientation with a dipole moment $\hat{d}_1$. The atom then traverses the same region of magnetic field except now in a state with a different dipole moment $\hat{d}_2$. The total phase is given by $\phi_{\mathrm{mS}}(\hat{d}_1) - \phi_{\mathrm{mS}}(\hat{d}_2)$ due to the paths crossing over, resulting in the difference of the motional-Stark phases. In (b), the configuration is mapped to account for the non-existence of magnetic monopoles. (c) Shows the configuration used in the experiment, in which the order of the paths is swapped, and so the two arms traverse the same region of space except both arms have their dipole moments oriented in the same direction at the same time.

magnetic monopoles but with each arm passing the opposite side of the monopoles. The result of this will be a phase difference between the two arms of $\delta\phi = \phi_{\mathrm{HMW};57} - \phi_{\mathrm{HMW};56}$.

Applying the Sangster-Hinds transformation amounts to straightening out the paths and inverting the direction of dipoles which traversed around one side of the monopole field. This is shown in the diagram where the paths are now identical and through regions of homogeneous magnetic field. Any dipole which traversed anti-clockwise as the figure is viewed has been inverted.

The result of this transformation is two sequential measurements of a HMW phase for the individual dipoles. The final step in transforming this into a form that resembles the experiment described in this chapter is to observe that, since the experiment occurs in a region of homogeneous electric and magnetic fields, and the phase is only related to the distance traveled by the atom in the state, we swap the order in which the atom traverses the fields.

In path 2 of the Sangster-Hinds scheme, the atom traverses the region of magnetic field in $-|57s\rangle$ before being swapped to $+|56s\rangle$. By swapping the order of the dipoles in this path the atom traverses the region in $+|56s\rangle$ before $-|57s\rangle$. The same total phase is acquired in both arms in these two schemes, but importantly, the new scheme does not require a superposition of two states with opposite dipoles.

The result is essentially an observation of the HMW phase but for a virtual state with a dipole given by $d' = d_{57} - d_{56}$ and giving rise to a phase $\phi_{\mathrm{HMW}} = \frac{2d'Bv_y t}{\hbar c}$, where t is the time spent by the arms in the crossed field in each state. The massive dipole moments available in Rydberg states mean this 'virtual dipole' can be orders of magnitude bigger than the dipoles available with ground-state atoms and allows for a measurement of the HMW phase using a pure Ramsey-type interferometer.

7.5 Experimental observation of the motional-Stark phase

7.5.1 Experimental apparatus

A schematic diagram of the experimental apparatus is shown in Figure 7.5. The neutral-atom beam enters the excitation and interferometry region between a pair of parallel copper electrodes separated by a distance $s = 1.48 \pm 0.01\,\mathrm{cm}$.

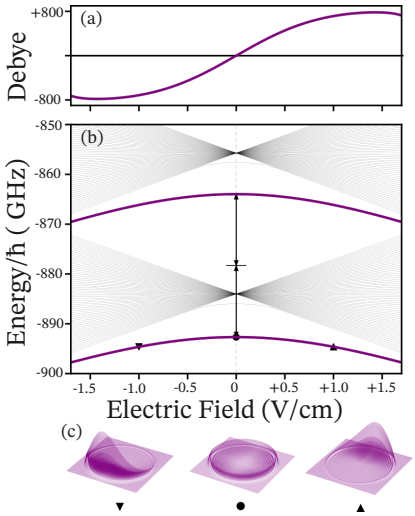

Figure 7.4: (a) The difference in the magnitude of the induced electric dipole moments of the 56s and 57s states in He as a function of electric field. (b) Rydberg Stark map for the $n = 56/57$ manifolds. The two-photon 18.530990 GHz transition between the 56s and 57s states is shown. (c) Visualisations of the electric field density of the valence electron at the three points highlighted in (b). When the direction of the electric field is reversed so does the electric field density of the state.

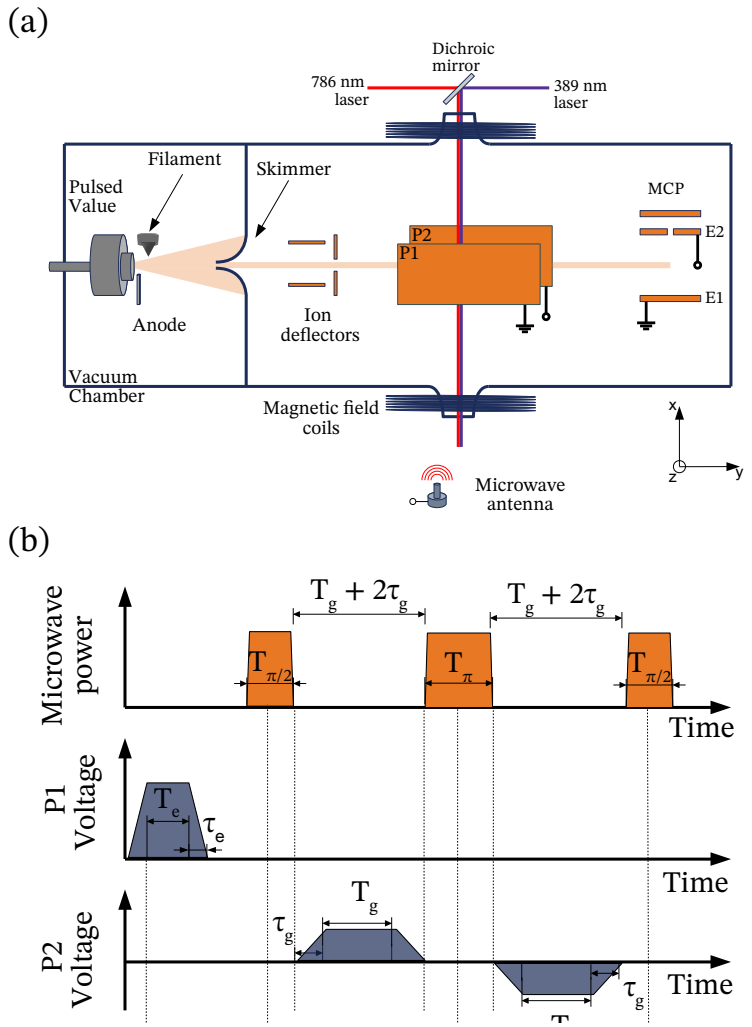

Figure 7.5: (a) Schematic of the experimental apparatus. The apparatus is the same as used in the experiments of Chapter 6 with the addition of magnetic coils outside the chamber to produce a region of homogenous magnetic field. (b) Sequence of applied microwave and voltage pulses used to perform motional-Stark phase interferometry. Inverting the second voltage pulse applied to P2 allows for the cancellation of the static-Stark phase but the enhancement of the motional-Stark phase.

The atoms are excited to the $1s56s\,^3S_1$ ($|56s\rangle$) Rydberg state using the $1s2s\,^3S_1 \rightarrow 1s3p\,^3P_2 \rightarrow 1s56s\,^3S_1$ two-color two-photon laser photoexcitation scheme. After laser photoexcitation, the Rydberg atoms are subjected to a $\pi/2$–π–$\pi/2$ Hahn-echo sequence of microwave pulses, which coherently transfer population between the $|56s\rangle$ and $1s57s\,^3S_1$ ($|57s\rangle$) states via a two-photon transition at a frequency of $\omega_{56s\,57s} = 2\pi \times (2 \times 18.530\,990)$ GHz.

In the time intervals between microwave pulses, a potential difference is applied across the electrodes to generate homogeneous electric fields at the atoms' position. The time evolution of the potential differences is characterized by a rise and fall time $t_r = 100$ ns and a duration at their maximum of $t_t = 1000$ ns (see Figure 7.5b). With the plates P1 and P2 placed parallel, the quality of the microwave field meant it was possible to perform equally spaced Rabi pulses in time.

The durations of the Rabi pulses were 60 ns, 105 ns and 65 ns respectively. The homogeneous electric field induces state-dependent electric dipole moments $\hat{d}_{56/57} = 2\alpha_{56/57}E$, where $\alpha_{56(57)} = 7.615(8.623) \pm 0.001 \times 10^{-29}\,\mathrm{J\,m^2/V^2}$ werecomputed numerically using Numerov meth-

ods outlined in Chapter 2. The maximum electric fields employed in this experiment are 0.135 V/cm and the $\ell = 0$ are well described by a quadratic energy shift up to this field strength. The magnitude of the effective electric dipole moment $\hat{d}' = \hat{d}_{57} - \hat{d}_{56}$ as a function of electric field up to the Inglis-Teller limit is shown in Figure 7.4(a), demonstrating the magnitude of d' that is possible.

The uniformity of the applied voltage pulse was checked and found to be accurate to within 0.5%. Current-carrying coils wrapped around the outside of the vacuum chamber allow magnetic fields to be applied along the $\hat{x}$ axis, perpendicular to both the beam direction ($\hat{y}$) and the axis of polarisation of the atoms ($\hat{z}$).

The magnetic field was measured using a hall probe after the experiment was completed by opening up the chamber and placing a hall probe in the location of the experiment within the plates. The magnetic field as a function of applied current was found to be $B_x = B_0 + \beta I$, where $B_0 = -0.25 \pm 0.25\,\mathrm{G}$ is the stray magnetic field, I is the applied current in the solenoids, and $\beta = -1.31 \pm 0.05\,\mathrm{G/A}$ is the proportionality factor.

7.5.2 Numerical model of the experiment

To simulate these experiments, a simplified numerical Monte-Carlo model is used to capture the essence of the motional-Stark effect as a function of varying the current to the magnetic coils. The total phase in each arm ϕ_i, can be separated into the combination of the HMW phase and other phases independent of the applied current, (e.g., microwave pulses, small dynamic phases, static Stark effect etc.). This quantity is $\phi_i(I) = \phi_{\mathrm{mS};i}(I) + \phi_{\mathrm{O};i}$.

Since $\phi_{\mathrm{O};i}$ is independent of the magnetic field, it can be treated as a free parameter in the model and fitted to the experimental data. The motional-Stark phase in each arm is calculated from Equation 7.5 as,

$$\phi_{\mathrm{mS;i}}(I) = \frac{2(B_0 + \beta I)v_y}{\hbar} \int_0^{t_f} \alpha_i(t) \left(E_0 + \frac{V(t)}{s} \right) \mathrm{d}t, \tag{7.13}$$

Here, the magnetic field is assumed to be $B_x = B_0 + \beta I$, the dipole in arm i is given by $d_i = 2\alpha_i(t)(E_0 + \frac{V(t)}{s})$, where $\alpha_i(t)$ is a step function between $\alpha_{56/57}$ at time t_π and $V(t)$ corresponds to the voltage pulse used. In the perfect limit where there are no stray fields $E_0 = B_0 = 0$ and $V(t)$ is a perfect step function, the total phase will be given by Equation 7.9, and would also constitute a measurement of the HMW phase for a virtual dipole.

To address the imperfections present in the experimental setup, Monte Carlo simulations were conducted. All initial parameters were sampled from random distributions, e.g., the voltage trace $V(t)$ is varied shot-by-shot to include the slight asymmetries introduced between the two voltage pulses $V_{\mathrm{max;p1}}$ and $V_{\mathrm{max;p2}}$. The total phase as a function of the applied current in is then given by $\phi_{\mathrm{total};1/2}(I) = \phi_{\mathrm{mS};1/2}(I) + \phi_{\mathrm{O};1/2}$.

All other possible phases arising from e.g. microwave pulses, dynamic phases, static Stark effects are accounted for by the term ϕ_{O}. This term is assumed to be independent of the magnetic field, and a free parameter to be fit to the experimental data. The probability of measuring each of the Rydberg states as a function of current I is given by $P_{56/57}(I) = \frac{1}{2} \pm \cos(\delta\phi_{\mathrm{mS}}(I) - \delta\phi_0)$.

7.5.3 Experimental results

The experiments shown in Figure 7.6 demonstrate the phase evolution for $V_{\mathrm{max}} = 0.2\,\mathrm{V}$ under two configurations of voltage pulses. Panel (a) shows the configuration of opposite-direction electric field pulses, which lead to a significant motional-Stark phase. The experimental periodicity of the fringes is in good agreement with the model outlined above.

As the applied current to the coils is increased, the population of the $|57\mathrm{s}\rangle$ state oscillates, indicating a full 2π phase accumulation due to the motional-Stark phase. Panel (b) has both electric field pulses orientated in the same direction, inducing dipole moments with similar orientations in each half of the measurement sequence.

Under ideal experimental conditions, there should not be any phase accumulation with the pulses orientated in the same direction, as the motional-Stark phase should cancel out. What is actually observed is a small variation in the observed $|57\mathrm{s}\rangle$ population as a function of magnetic field.

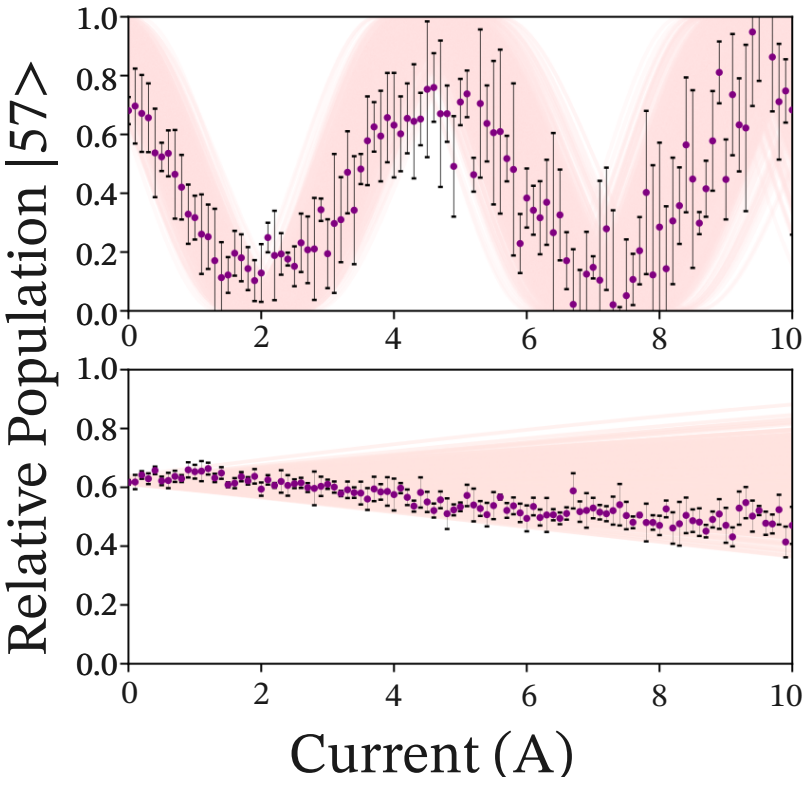

Figure 7.6: (a) Results of experiment using the pulse sequence shown in Figure 7.5 (inset). (b) Experiment repeated without inverting the direction of the second voltage pulse.

The largest source of uncertainty lies in the symmetry of the applied voltage pulses. This results in slightly different induced dipole moments in each half of the measurement sequence, i.e., before and after the π pulse, resulting in a small but observable motional-Stark phase shift.

Another possible source of slight asymmetry is the homogeneity of the magnetic field. The experiments take place over $\approx 4mm$ inside the plates; precise measurements mapping out the exact magnetic field distribution could reveal slight inhomogeneities which show up as uncancelled phases.

The uncancelled phases in the experiments indicated the conditions are not quite perfect in the sense of representing a measurement of the He-McKellar-Wilkens phase, as that would rely on the atoms traversing an identical region of electric and magnetic fields to allow for the transformation from the Sangster-Hinds set-up to the equivalent Ramsey-Hahn.

The motional-Stark phases observed here are, however, orders of magnitude larger than those observed in Ref. [131] and large enough to be easily discerned from small phase shifts due to other sources. This result shows the ease with which the HMW phase could be measured in Rydberg states compared to the intricate and carefully controlled experiments performed with ground-states.

More relevant and important for our goals in Rydberg-state interferometery, the experiments are successful in demonstrating controllability between the motional and static Stark phases by the simple inversion of a voltage pulse. We have demonstrated the ability to isolate the motional-Stark phase from the static-Stark phase and potential application of it's geometric properties are considered in the next section.

The magnitude of the motional-Stark phase is varied by changing the magnitude of the induced dipole moments, as shown in Figure 7.7. In each of the panels, an up-down sequence of voltage pulses is applied with varying $V_{\max}$ values. The magnitude of the resulting phase accumulation can be seen to decrease as the magnitude of the dipole moments decreases.

The observed periodicity of each set of fringes is in excellent agreement with that predicted by the model. The bottom panel shows the phase accumulated in the case where the atoms are not polarised and shows no phase accumulation indicating the insignificance of the Zeeman shift and supporting that the uncancelled phase in Figure 7.6 is due to motional-Stark effects.

Much greater phase accumulation could be achieved by polarizing the atoms more strongly. In these experiments, the maximum applied voltages were $V_{\max} = 0.2\,\mathrm{V}$, which produces an electric field around $F_{\max} \approx 0.135\,\mathrm{V/cm}$. The magnitude of the difference in dipole moments is $\hat{d}' \approx 50\,\mathrm{D}$. This value is far from the magnitude of $800\,\mathrm{D}$, which could be achieved below the Inglis–Teller limit field.

Additionally, the magnetic fields used reached $\approx 10\,\mathrm{G}$. The strength of the magnetic fields applied were limited due to the effect the mag-

netic field had on the collection efficiency of the MCP. Careful experimental design would eliminate this impact and allow for much greater magnetic fields to be used.

7.6 Accelerometery via the motional-Stark phase

In this section, we present one potential application for this scheme, accelerometry via the motional-Stark phase. The experiments of Chapter 6 demonstrated the necessary control over Rydberg states with inhomogeneous electric fields to create a Stern-Gerlach type interferometer. A full-loop version of this would be sensitive to inertial effects.

Those experiments demonstrated the challenges of dephasing arising from velocity dispersion across the Rydberg beam. The Humpy-Dumpty effect [111] also highlights the additional challenge of adequately controlling the inhomogeneous field gradients to recombine the arms of the interferometer.

This demonstration of the motional-Stark phase allows for a potential alternative approach to sense inertial effects. The motional-Stark effect arises from the coupling between the internal and external dynamics of the dipole in the magnetic field. This allows, in principal, for an internal state interferometer to be sensitive to centre-of-mass motion. Additionally, due to the structure of the motional-Stark phase, this approach does not rely on large physical path differences and inhomogenous field gradients like in a Stern-Gerlach type interferometer.

In this section, an experiment using the motional-Stark phase is discussed that could be sensitive to gravitational accelerations. By coherently repeating the experiment performed in this chapter either side of a period of free-fall, a dispersionless phase proportional to the acceleration could be observed. This is essentially a coherent extension of the free-fall thought experiment briefly discussed at the end in Section 7.3.

In that thought experiment, one waits a variable amount of time T_w before performing the interferometery sequence shown in this chapter. This allows time for a gravitational acceleration to modify the velocity, $v(T_w) = v_0 + gT$, and introduce a term in the phase difference $\delta\phi \propto v(T_w)$. Performing a series of independent experiments as a function of T_w the effect of gravity can in principle be observed. This experiment would be dispersive in initial velocity.

The dispersion could be overcome by putting the free-fall between two regions of crossed electric and magnetic field. Motional-Stark phases are generated in these regions by using the pulse sequence demonstrated in this chapter. If the voltage pulses, or the initial atom states in the second region, are reversed, the phase accumulation will also be reversed. This results in the motional-Stark phase proportional to the initial velocity v_0 to cancelling out.

However, an acceleration in the intervening T_w will result in all the atoms travelling further in the second region of crossed fields. As this acceleration will be the same for all atoms in the beam this distance will be identical. The leads to a residue phase difference is only related

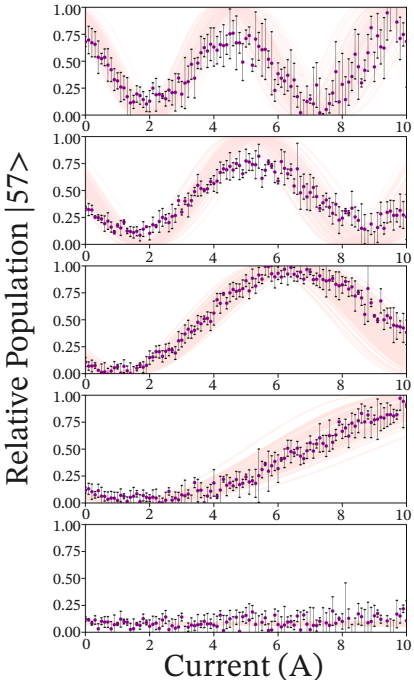

Figure 7.7: Series of experiments performed with configuration of voltage pulses to enhance the motional-Stark phase. The magnitude of the electric field, and hence induced electric dipole moments, were varied. (a) $V_{\max} = 0.20\,\mathrm{V}$. (b) $V_{\max} = 0.15\,\mathrm{V}$. (c) $V_{\max} = 0.10\,\mathrm{V}$. (d) $V_{\max} = 0.05\,\mathrm{V}$. (e) $V_{\max} = 0.0\,\mathrm{V}$.

to the acceleration, resulting in total phase which is dispersionless with respect to the initial velocity. Thus, all atoms will acquire an identical total motional-Stark phase.

Such a scheme has an additional advantage that the Rydberg states can be allowed to free-fall in a field-free environment allowing the effect of gravity to accumulate with minimal background noise. As Rydberg states are incredibly sensitive to external fields this is a very advantageous property given that the weak effect of gravity requires experiments with large free-fall times. This also removes the requirement of maintaining crossed fields throughout the whole beam path of the experiment. Instead small, well controlled regions of crossed fields can be maintained.

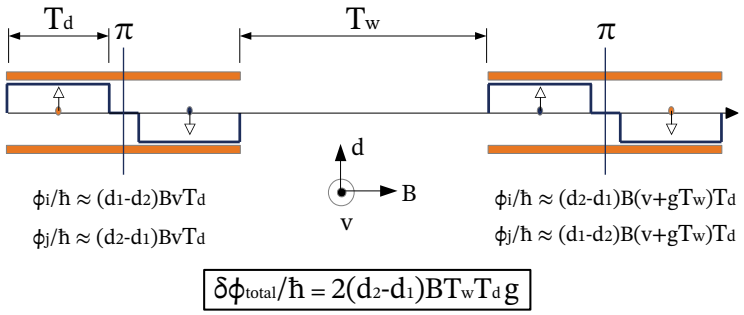

Figure 7.8: Proposed coherent free-fall experiment using the sequence of voltage and microwave pulses performed in this chapter. A free-fall period under gravity of T_w occurs between two regions of crossed magnetic and electric fields. The fields are configured where the magnetic field is along the beam axis which is perpendicular to the direction of gravity. Within these regions a motional-Stark phase proportional to the velocity v, is imprinted onto a coherent superposition of two dipole states. The pulse sequence in the second region is configured to reverse the phase accumulated in the first region. If there is an acceleration g within the free-fall period T_w the phases will not fully cancel leading to a dispersionless phase difference $\delta\phi_{\text{total}} \propto g$.

The described scheme is shown in Figure. 7.8. At $T = 0$ the motional-Stark sequence is performed to imprint information about the initial velocity onto the phase. This results in the dispersive phase $\delta\phi \propto v$, where $\phi_i \approx (d_1 - d_2)BvT_d$, where to simplify the analysis we assume $T_w \gg T_d$ and the phase differences due to g within the regions of crossed fields are small compared to the phase shift due to the initial velocity at the start of the crossed field region.

The atom is then allowed to free-fall under gravity for a time T_w. In this time period the arms acquire no additional phase difference. The atom then undergoes the reverse of the motional-Stark phase sequence. If there is no acceleration, the cancellation will be perfect, and no phase difference will be recorded. If there is an acceleration during the time T_w this will be measurable. This scheme has the advantage of being non-dispersive in velocity, as the phase due to the initial velocity cancels leaving only a phase term proportional to the acceleration $\delta\phi = 2\hbar(d_1 - d_2)BT_wT_dg$.

7.7 Future directions

There are a number of further potential directions for experiments that make use of the motional-Stark effect with Rydberg states. Incoherent Rydberg atom and molecule optics has been demonstrated with deflectors, traps, and beam splitters. The coupling of the internal dynamics to the external motion via the motional-Stark phase could open up avenues to explore coherent optical components.

The dynamic phase is dependent on the speed of the atom, while the motional-Stark phase depends on the velocity. Atoms travelling in opposite directions at the same speed acquire an identical dynamic phase and an opposite motional-Stark phase. The Stark shift, which generates the force for the dynamic phase shift, depends on the magnitude of the electric field, while the motional-Stark phase depends on both the magnitude and direction of the electric field.

One interesting application could therefore be the implementation of an atom diode. This is analogous to a conventional diode, where an atom in a given state will propagate only in a single direction. These have been demonstrated via optical pumping with ground-state atoms [132], [133] and are inherently non-coherent. Lepoutre *et al.* [131] commented that a similar, but coherent, diode effect could be achieved with the motional-Stark phase.

An atom passing through a region in which the dynamic phase is biased to impart a $\pi/2$ phase shift. This phase would be imparted irrespective of the direction of approach of the atom. The motional-Stark phase is biased to provide an additional $\pi/2$ phase, where atoms travelling in opposite directions will acquire $\pi/2 \pm \pi/2$ phase. The net result of this is that atoms travelling in one direction will switch internal states, while atoms travelling the other way will remain in their initial state.

The necessary geometric phase shifts to implement a Rydberg-atom diode have been demonstrated in this chapter, and the necessary dynamic phase shifts in Chapter 6. This effect has been proposed as a means of cooling and trapping neutral atoms [134]. It would be interesting to determine the region of applicability and utility of this for Rydberg states.

The quantisation of the orbit of a charged particle in a uniform magnetic field is known as Landau quantization [135]. The dynamics of neutral systems of particles in electromagnetic fields can lead to interesting coupling between the dipole moments and fields. An analogue of Landau quantisation for a magnetic dipole has been described in Ericsson *et al.* [136]. This required an electric field configuration in which the magnetic dipole interacts with an electric field such that no torque is introduced but the Aharonov–Casher phase is still present. The equivalent Landau–He–McKellar–Wilkens quantisation has also been theorised for an electric dipole [137].

8
Conclusions

In this thesis we present results of experiments exploring the interactions of Rydberg helium atoms in states of low-ℓ, with large electric dipole polarisabilities, and electromagnetic potentials.

In Part I, highly-excited atoms in states with principal quantum numbers $n > 100$ were used to probe the regime in which the strength of the rate of resonant driving of a two-level system is on the order of the transition frequency. The validity of various approximate models were probed by comparing the resulting energy spectra with the results of numerical calculations. These experiments demonstrated the applicability of the numerical techniques up to driving strengths that are beyond the commonly used rotating wave approximation.

By applying large enough driving fields, the polarizability of states can be modified via Floquet engineering. These experiments were initially conducted with the aim of exploring different trapping mechanisms for beams of atoms and molecules in Rydberg states. The findings were that such a mechanism could provide a trap depth appropriate for applications in the preparation of cold samples of Rydberg atoms and molecules. This has applications in the analysis of Rydberg-state sensing of RF electric fields and for rapid state preparation and manipulation.

In Part. II, the direction of research extended into exploring coherent effects related to the external motion of Rydberg states in beams. Incoherent atom optics components such as deflectors and beam-splitters have previously been demonstrated for Rydberg atom beams. It is also possible to apply these force generating components to coherent superpositions of states with different electric dipole moments, resulting in coherent superpositions of momentum states.

The experiment of Section 6 was a continuation of this line of research, that began with [41]. Here an electric analogue of Stern-Gerlach interferometry was performed with circular states in helium. The non-adiabatic losses seen in those experiments were overcome in the present work by using low-ℓ states that are well separated from the manifold of Rydberg-Stark states. This allowed for the mitigation of non-adiabatic losses in the force generating ramped electric fields. COM-separations on the order of .75 nm $\approx 15\lambda_{\mathrm{dB}}$ were achieved, which is much larger than had previously been seen.

The new limiting factor of these experiments was the dispersion of phases across the beam in our apparatus. The fast moving nature of the atoms and the dynamic phases due to both the kinetic energy and internal energy resulted in large dispersion across the bunch of atoms. The simple geometry of the interferometer used in both this experiment and the circular state experiment could be improved to achieve larger separations and sensitivities.

In the future, the spatial variation in the electric field generating the forces could be modified to remove the spatial dependence of the electric field gradient along the axis of interest. The use of the transverse component of velocity in a beam could also allow for greater coherence, as the beam is much colder in this direction.

A primary motivation for interferometry with Rydberg beams is the eventual application to beams of positronium. This poses problems in the form of much larger velocities and also the lack of low-ℓ states, due to the hydrogenic nature of Ps. More work would therefore be required to design and evaluate Stern-Gerlach type interferometers for Rydberg states, so as to be useful for observations of accelerations not suffering from dispersion.

In Chapter 7, the unique properties of Rydberg states were leveraged to observe the motional-Stark effect in a Ramsey-type interferometer. This was possible by measuring the difference between the motional-Stark phase for states with two different induced electric dipole moments. The coupling of the external motion into an internal state interferometer has some interesting future directions. The dipole-directional dependence could result in novel atom optics components such as diodes, that only allow transmission of a given Rydberg state in one direction. It has potential for use in interferometers using fast moving beams where established atom cooling methods are not possible. As this phase is non-dispersive under the appropriate configuration of electromagnetic potentials, we propose a scheme to use the motional-Stark phase to measure accelerations. More research would need to be performed to determine if such an accelerometer could be of use for measurements of gravity with positronium, or a potential approach for low-accuracy warm atom based accelerometers in vapour cells.

Bibliography

[1] J. R. Rydberg, "XXXIV. on the structure of the line-spectra of the chemical elements," *The London, Edinburgh, and Dublin Philosophical Magazine and Journal of Science*, vol. 29, no. 179, pp. 331–337, Apr. 1, 1890, Publisher: Taylor & Francis _eprint: https://doi.org/10.1080/14786449008619945, 1941-5982.

[2] A. Sommerfeld, "Zur quantentheorie der spektrallinien," *Annalen der Physik*, vol. 356, no. 17, pp. 1–94, 1916.

[3] E. Amaldi and E. Segré, "Effect of pressure on high terms of alkaline spectra," *Nature*, vol. 133, no. 3352, pp. 141–141, Jan. 1934, Number: 3352 Publisher: Nature Publishing Group, 1476-4687.

[4] F. A. Jenkins and E. Segrè, "The quadratic zeeman effect," *Physical Review*, vol. 55, no. 1, pp. 52–58, Jan. 1, 1939, 0031-899X.

[5] Y. N. Gnedin, A. A. Mihajlov, L. M. Ignjatović, *et al.*, "Rydberg atoms in astrophysics," *New Astronomy Reviews*, Proceedings of the VII Serbian Conference on Spectral Line Shapes (VII SCSLSA) held in Zrenjanin, Serbia June 15th-19th 2009, vol. 53, no. 7, pp. 259–265, Jul. 1, 2009, 1387-6473.

[6] D. Kleppner, "Inhibited spontaneous emission," *Physical Review Letters*, vol. 47, no. 4, pp. 233–236, Jul. 27, 1981, Publisher: American Physical Society.

[7] R. G. Hulet and D. Kleppner, "Rydberg atoms in "circular" states," *Physical Review Letters*, vol. 51, no. 16, pp. 1430–1433, Oct. 17, 1983, Publisher: American Physical Society.

[8] R. G. Hulet, E. S. Hilfer, and D. Kleppner, "Inhibited spontaneous emission by a rydberg atom," *Physical Review Letters*, vol. 55, no. 20, pp. 2137–2140, Nov. 11, 1985, Publisher: American Physical Society.

[9] M. Brune, S. Haroche, J. M. Raimond, L. Davidovich, and N. Zagury, "Manipulation of photons in a cavity by dispersive atom-field coupling: Quantum-nondemolition measurements and generation of ''schrödinger cat'' states," *Physical Review A*, vol. 45, no. 7, pp. 5193–5214, Apr. 1, 1992, 1050-2947, 1094-1622.

[10] M. Brune, F. Schmidt-Kaler, A. Maali, *et al.*, "Quantum rabi oscillation: A direct test of field quantization in a cavity," *Physical Review Letters*, vol. 76, no. 11, pp. 1800–1803, Mar. 11, 1996, 0031-9007, 1079-7114.

[11] S. Haroche, "Nobel lecture: Controlling photons in a box and exploring the quantum to classical boundary," *Reviews of Modern Physics*, vol. 85, no. 3, pp. 1083–1102, Jul. 12, 2013, Publisher: American Physical Society.

[12] A. Osterwalder and F. Merkt, "Using high rydberg states as electric field sensors," *Physical Review Letters*, vol. 82, no. 9, pp. 1831–1834, Mar. 1, 1999, Publisher: American Physical Society.

[13] M. T. Simons, A. B. Artusio-Glimpse, A. K. Robinson, N. Prajapati, and C. L. Holloway, "Rydberg atom-based sensors for radio-frequency electric field metrology, sensing, and communications," *Measurement: Sensors*, vol. 18, p. 100 273, Dec. 2021, 26659174.

[14] T. Gallagher, *Rydberg Atoms*. Jan. 1, 2006, Pages: 235 Publication Title: Springer Handbook of Atomic ADS Bibcode: 2006sham.book..235G.

[15] C. Cohen-Tannoudji, "The autler-townes effect revisited," *Amazing Light*, pp. 109–123, 1996.

[16] D. A. Anderson, S. A. Miller, G. Raithel, J. A. Gordon, M. L. Butler, and C. L. Holloway, "Optical measurements of strong microwave fields with rydberg atoms in a vapor cell," *Physical Review Applied*, vol. 5, no. 3, p. 034 003, Mar. 4, 2016, Publisher: American Physical Society.

[17] C. T. Fancher, D. R. Scherer, M. C. S. John, and B. L. S. Marlow, "Rydberg atom electric field sensors for communications and sensing," *IEEE Transactions on Quantum Engineering*, vol. 2, pp. 1–13, 2021, Conference Name: IEEE Transactions on Quantum Engineering, 2689-1808.

[18] M. T. Simons, A. H. Haddab, J. A. Gordon, D. Novotny, and C. L. Holloway, "Embedding a rydberg atom-based sensor into an antenna for phase and amplitude detection of radio-frequency fields and modulated signals," *IEEE Access*, vol. 7, pp. 164 975–164 985, 2019, Conference Name: IEEE Access, 2169-3536.

[19] T. F. Gallagher and P. Pillet, "Dipole–dipole interactions of rydberg atoms," *Advances in Atomic, Molecular, and Optical Physics*, vol. 56, pp. 161–218, 2008.

[20] M. D. Lukin, M. Fleischhauer, R. Cote, *et al.*, "Dipole blockade and quantum information processing in mesoscopic atomic ensembles," *Physical review letters*, vol. 87, no. 3, p. 037 901, 2001.

[21] D. Jaksch, J. I. Cirac, P. Zoller, S. L. Rolston, R. Côté, and M. D. Lukin, "Fast quantum gates for neutral atoms," *Physical Review Letters*, vol. 85, no. 10, pp. 2208–2211, Sep. 4, 2000, Publisher: American Physical Society.

[22] M. Endres, H. Bernien, A. Keesling, *et al.*, "Atom-by-atom assembly of defect-free one-dimensional cold atom arrays," *Science*, vol. 354, no. 6315, pp. 1024–1027, Nov. 25, 2016, Publisher: American Association for the Advancement of Science.

[23] T. M. Graham, Y. Song, J. Scott, *et al.*, "Multi-qubit entanglement and algorithms on a neutral-atom quantum computer," *Nature*, vol. 604, no. 7906, pp. 457–462, Apr. 2022, Number: 7906 Publisher: Nature Publishing Group, 1476-4687.

[24] M. Morgado and S. Whitlock, "Quantum simulation and computing with rydberg-interacting qubits," *AVS Quantum Science*, vol. 3, no. 2, p. 023 501, Jun. 2021, Publisher: American Vacuum Society.

[25] A. A. Morgan and S. D. Hogan, "Coupling rydberg atoms to microwave fields in a superconducting coplanar waveguide resonator," *Physical Review Letters*, vol. 124, no. 19, p. 193 604, May 12, 2020, Publisher: American Physical Society.

[26] M. Kaiser, C. Glaser, L. Y. Ley, *et al.*, "Cavity-driven rabi oscillations between rydberg states of atoms trapped on a superconducting atom chip," *Physical Review Research*, vol. 4, no. 1, p. 013 207, Mar. 18, 2022, 2643-1564.

[27] S. D. Hogan, "Rydberg-stark deceleration of atoms and molecules," *EPJ Techniques and Instrumentation*, vol. 3, no. 1, pp. 1–50, Dec. 2016, Number: 1 Publisher: SpringerOpen, 2195-7045.

[28] H. L. Bethlem, G. Berden, and G. Meijer, "Decelerating neutral dipolar molecules," *Physical Review Letters*, vol. 83, no. 8, pp. 1558–1561, Aug. 23, 1999, Publisher: American Physical Society.

[29] S. Y. T. van de Meerakker, H. L. Bethlem, N. Vanhaecke, and G. Meijer, "Manipulation and control of molecular beams," *Chemical Reviews*, vol. 112, no. 9, pp. 4828–4878, Sep. 12, 2012, Publisher: American Chemical Society, 0009-2665.

[30] S. D. Hogan, J. A. Agner, F. Merkt, T. Thiele, S. Filipp, and A. Wallraff, "Driving rydberg-rydberg transitions from a coplanar microwave waveguide," *Physical Review Letters*, vol. 108, no. 6, p. 063 004, Feb. 9, 2012, Publisher: American Physical Society.

[31] V. Sandoghdar, C. I. Sukenik, E. A. Hinds, and S. Haroche, "Direct measurement of the van der waals interaction between an atom and its images in a micron-sized cavity," *Physical Review Letters*, vol. 68, no. 23, pp. 3432–3435, Jun. 8, 1992, Publisher: American Physical Society.

[32] D. F. Gray, Z. Zheng, K. A. Smith, and F. B. Dunning, "Ionization of k(nd) rydberg-state atoms at a surface," *Physical Review A*, vol. 38, no. 3, pp. 1601–1603, Aug. 1, 1988, Publisher: American Physical Society.

[33] M. Amoretti, C. Amsler, G. Bonomi, *et al.*, "Production and detection of cold antihydrogen atoms," *Nature*, vol. 419, no. 6906, pp. 456–459, Oct. 2002, Number: 6906 Publisher: Nature Publishing Group, 1476-4687.

[34] A. Kellerbauer, M. Amoretti, A. S. Belov, *et al.*, "Proposed antimatter gravity measurement with an antihydrogen beam," *Nuclear Instruments and Methods in Physics Research Section B: Beam Interactions with Materials and Atoms*, Low Energy Positron and Positronium Physics, vol. 266, no. 3, pp. 351–356, Feb. 1, 2008, 0168-583X.

[35] G. B. Andresen, M. D. Ashkezari, M. Baquero-Ruiz, *et al.*, "Trapped antihydrogen," *Nature*, vol. 468, no. 7324, pp. 673–676, Dec. 2010, Number: 7324 Publisher: Nature Publishing Group, 1476-4687.

[36] R. S. Vallery, P. W. Zitzewitz, and D. W. Gidley, "Resolution of the orthopositronium-lifetime puzzle," *Physical Review Letters*, vol. 90, no. 20, p. 203 402, May 23, 2003, Publisher: American Physical Society.

[37] D. B. Cassidy, T. H. Hisakado, H. W. K. Tom, and A. P. Mills, "Efficient production of rydberg positronium," *Physical Review Letters*, vol. 108, no. 4, p. 043 401, Jan. 26, 2012, Publisher: American Physical Society.

[38] P. Lancuba and S. D. Hogan, "Transmission-line decelerators for atoms in high rydberg states," *Physical Review A*, vol. 90, no. 5, p. 053 420, Nov. 18, 2014, Publisher: American Physical Society.

[39] A. P. Mills and M. Leventhal, "Can we measure the gravitational free fall of cold rydberg state positronium?" *Nuclear Instruments and Methods in Physics Research Section B: Beam Interactions with Materials and Atoms*, vol. 192, no. 1, pp. 102–106, May 1, 2002, 0168-583X.

[40] D. B. Cassidy and S. D. Hogan, "Atom control and gravity measurements using rydberg positronium," *International Journal of Modern Physics: Conference Series*, vol. 30, p. 1 460 259, Jan. 2014, Publisher: World Scientific Publishing Co.

[41] J. E. Palmer and S. D. Hogan, "Electric rydberg-atom interferometry," *Physical Review Letters*, vol. 122, no. 25, p. 250 404, Jun. 27, 2019, Publisher: American Physical Society.

[42] I. I. Beterov, D. B. Tretyakov, I. I. Ryabtsev, V. M. Entin, A. Ekers, and N. N. Bezuglov, "Ionization of rydberg atoms by blackbody radiation," *New Journal of Physics*, vol. 11, no. 1, p. 013 052, Jan. 2009, 1367-2630.

[43] J. W. Farley and W. H. Wing, "Accurate calculation of dynamic stark shifts and depopulation rates of rydberg energy levels induced by blackbody radiation. hydrogen, helium, and alkali-metal atoms," *Phys. Rev. A*, vol. 23, pp. 2397–2424, 5 May 1981.

[44] L. L. Brown and S. D. Hogan, "Tunable rydberg–rydberg transitions in helium with reduced sensitivity to dc electric fields by two-colour microwave dressing," *Journal of Physics B: Atomic, Molecular and Optical Physics*, vol. 56, no. 20, p. 205 001, Sep. 2023.

[45] S. H. Autler and C. H. Townes, "Stark effect in rapidly varying fields," *Physical Review*, vol. 100, no. 2, pp. 703–722, Oct. 15, 1955, Publisher: American Physical Society.

[46] J. H. Shirley, "Solution of the schr\"odinger equation with a hamiltonian periodic in time," *Physical Review*, vol. 138, no. 4, B979–B987, May 24, 1965, Publisher: American Physical Society.

[47] A. A. Morgan, V. Zhelyazkova, and S. D. Hogan, "Preparation of circular rydberg states in helium with $n \geq 70$ using a modified version of the crossed-fields method," *Phys. Rev. A*, vol. 98, p. 043 416, 4 Oct. 2018.

[48] M. L. Zimmerman, M. G. Littman, M. M. Kash, and D. Kleppner, "Stark structure of the rydberg states of alkali-metal atoms," *Physical Review A*, vol. 20, no. 6, pp. 2251–2275, Dec. 1, 1979, Publisher: American Physical Society.

[49] A. Deller and S. D. Hogan, "Microwave spectroscopy of the $1snp ^{3}p_{j} $ fine structure of high rydberg states in $^{4} \mathrm{he}$," *Physical Review A*, vol. 97, no. 1, p. 012 505, Jan. 12, 2018, Publisher: American Physical Society.

[50] P. Virtanen, R. Gommers, T. E. Oliphant, *et al.*, "SciPy 1.0: Fundamental Algorithms for Scientific Computing in Python," *Nature Methods*, vol. 17, pp. 261–272, 2020.

[51] R. Lehoucq, D. Sorensen, and C. Yang, *ARPACK Users' Guide: Solution of Large-scale Eigenvalue Problems with Implicitly Restarted Arnoldi Methods* (Software, Environments, and Tools). Society for Industrial and Applied Mathematics (SIAM, 3600 Market Street, Floor 6, Philadelphia, PA 19104), 1998, 9780898719628.

[52] p. lancuba patrick, "Rydberg-stark deceleration and trapping of helium atoms above electrical transmission-lines," Ph.D. dissertation, UCL (University College London), 2016.

[53] T. Halfmann, J. Koensgen, and K. Bergmann, "A source for a high-intensity pulsed beam of metastable helium atoms," *Measurement Science and Technology*, vol. 11, no. 10, p. 1510, Oct. 2000, 0957-0233.

[54] S. Y. T. van de Meerakker, H. L. Bethlem, and G. Meijer, "Taming molecular beams," *Nature Physics*, vol. 4, no. 8, pp. 595–602, Aug. 2008, Number: 8 Publisher: Nature Publishing Group, 1745-2481.

[55] H. Haberland, U. Buck, and M. Tolle, "Velocity distribution of supersonic nozzle beams," *Review of Scientific Instruments*, vol. 56, no. 9, pp. 1712–1716, Sep. 1985, 0034-6748, 1089-7623.

[56] J. L. Wiza *et al.*, "Microchannel plate detectors," *Nucl. Instrum. Methods*, vol. 162, no. 1-3, pp. 587–601, 1979.

[57] E. Vliegen, "Rydberg states in atom and molecule optics," Ph.D. dissertation, ETH Zurich, 2006.

[58] J. D. R. Tommey and S. D. Hogan, "Resonant rydberg-atom–microwave-field interactions in the ultrastrong-driving regime: Beyond the rotating-wave approximation," *Physical Review A*, vol. 100, no. 5, p. 053 417, Nov. 25, 2019, Publisher: American Physical Society.

[59] M. O. Scully and M. S. Zubairy, *Quantum optics*. Cambridge university press, 1997.

[60] B. R. Mollow, "Power spectrum of light scattered by two-level systems," *Physical Review*, vol. 188, no. 5, pp. 1969–1975, Dec. 25, 1969, Publisher: American Physical Society.

[61] F. Bloch and A. Siegert, "Magnetic resonance for nonrotating fields," *Physical Review*, vol. 57, no. 6, pp. 522–527, Mar. 15, 1940, Publisher: American Physical Society.

[62] H. Fan, S. Kumar, J. Sedlacek, H. Kübler, S. Karimkashi, and J. P. Shaffer, "Atom based RF electric field sensing," *Journal of Physics B: Atomic, Molecular and Optical Physics*, vol. 48, no. 20, p. 202 001, Sep. 2015, Publisher: IOP Publishing, 0953-4075.

[63] C. L. Holloway, M. T. Simons, J. A. Gordon, A. Dienstfrey, D. A. Anderson, and G. Raithel, "Electric field metrology for SI traceability: Systematic measurement uncertainties in electromagnetically induced transparency in atomic vapor," *Journal of Applied Physics*, vol. 121, no. 23, p. 233 106, Jun. 21, 2017, 0021-8979, 1089-7550.

[64] C. Deng, F. Shen, S. Ashhab, and A. Lupascu, "Dynamics of a two-level system under strong driving: Quantum-gate optimization based on floquet theory," *Physical Review A*, vol. 94, no. 3, p. 032 323, Sep. 27, 2016, Publisher: American Physical Society.

[65] P. Forn-Díaz, J. J. García-Ripoll, B. Peropadre, *et al.*, "Ultrastrong coupling of a single artificial atom to an electromagnetic continuum in the nonperturbative regime," *Nature Physics*, vol. 13, no. 1, pp. 39–43, Jan. 2017, Number: 1 Publisher: Nature Publishing Group, 1745-2481.

[66] Y. Ni, P. Xu, and J. D. D. Martin, "Reduction of the dc-electric-field sensitivity of circular rydberg states using nonresonant dressing fields," *Physical Review A*, vol. 92, no. 6, p. 063 418, Dec. 21, 2015, Publisher: American Physical Society.

[67] S. Merz, N. Vanhaecke, W. Jäger, M. Schnell, and G. Meijer, "Decelerating molecules with microwave fields," *Physical Review A*, vol. 85, no. 6, p. 063 411, Jun. 19, 2012, Publisher: American Physical Society.

[68] S. D. Hogan, Y. Houston, and B. Wei, "Laser photoexcitation of rydberg states in helium with $n > 400$," *Journal of Physics B: Atomic, Molecular and Optical Physics*, vol. 51, no. 14, p. 145 002, Jul. 28, 2018, 0953-4075, 1361-6455.

[69] J. Tuorila, M. Silveri, M. Sillanpää, E. Thuneberg, Y. Makhlin, and P. Hakonen, "Stark effect and generalized bloch-siegert shift in a strongly driven two-level system," *Physical Review Letters*, vol. 105, no. 25, p. 257 003, Dec. 14, 2010, Publisher: American Physical Society.

[70] B. Zaks, D. Stehr, T.-A. Truong, P. M. Petroff, S. Hughes, and M. S. Sherwin, "THz-driven quantum wells: Coulomb interactions and stark shifts in the ultrastrong coupling regime," *New Journal of Physics*, vol. 13, no. 8, p. 083 009, Aug. 2011, 1367-2630.

[71] J. D. Pritchard, J. A. Isaacs, M. A. Beck, R. McDermott, and M. Saffman, "Hybrid atom-photon quantum gate in a superconducting microwave resonator," *Physical Review A*, vol. 89, no. 1, p. 010 301, Jan. 16, 2014, Publisher: American Physical Society.

[72] T. Young, "II. the bakerian lecture. on the theory of light and colours," *Philosophical Transactions of the Royal Society of London*, vol. 92, pp. 12–48, Jan. 1997, Publisher: Royal Society.

[73] J. Frercks, "Fizeau's research program on ether drag: A long quest for a publishable experiment," *Physics in Perspective*, vol. 7, no. 1, pp. 35–65, Mar. 1, 2005, 1422-6960.

[74] A. A. Michelson and E. W. Morley, "On the relative motion of the earth and the luminiferous ether," *American Journal of Science*, vol. s3-34, no. 203, pp. 333–345, 1887, Publisher: American Journal of Science _eprint: https://www.ajsonline.org/content/s3-34/203/333.full.pdf, 0002-9599.

[75] M. Planck, "Ueber das gesetz der energieverteilung im normalspectrum," *Annalen der Physik*, vol. 309, no. 3, pp. 553–563, 1901, _eprint: https://onlinelibrary.wiley.com/doi/pdf/10.1002/andp.19013090310, 1521-3889.

[76] A. Einstein, "Über einen die erzeugung und verwandlung des lichtes betreffenden heuristischen gesichtspunkt," *Annalen der Physik*, vol. 322, no. 6, pp. 132–148, 1905, 1521-3889.

[77] L. De Broglie, "Waves and quanta," *Nature*, vol. 112, no. 2815, pp. 540–540, Oct. 1923, Number: 2815 Publisher: Nature Publishing Group, 1476-4687.

[78] C. Davisson and L. H. Germer, "The scattering of electrons by a single crystal of nickel," *Nature*, vol. 119, no. 2998, pp. 558–560, Apr. 1927, Number: 2998 Publisher: Nature Publishing Group, 1476-4687.

[79] G. P. Thomson and A. Reid, "Diffraction of cathode rays by a thin film," *Nature*, vol. 119, no. 3007, pp. 890–890, Jun. 1927, Number: 3007 Publisher: Nature Publishing Group, 1476-4687.

[80] G. Möllenstedt and H. Düker, "Beobachtungen und Messungen an Biprisma-Interferenzen mit Elektronenwellen," *Zeitschrift für Physik*, vol. 145, no. 3, pp. 377–397, Jun. 1, 1956, 0044-3328.

[81] C. Jönsson, "Elektroneninterferenzen an mehreren künstlich hergestellten Feinspalten," *Zeitschrift für Physik*, vol. 161, no. 4, pp. 454–474, Aug. 1, 1961, 0044-3328.

[82] Y. Aharonov and D. Bohm, "Significance of electromagnetic potentials in the quantum theory," *Physical Review*, vol. 115, no. 3, pp. 485–491, Aug. 1, 1959, Publisher: American Physical Society.

[83] R. G. Chambers, "Shift of an electron interference pattern by enclosed magnetic flux," *Physical Review Letters*, vol. 5, no. 1, pp. 3–5, Jul. 1, 1960, Publisher: American Physical Society.

[84] A. Tonomura, N. Osakabe, T. Matsuda, *et al.*, "Evidence for aharonov-bohm effect with magnetic field completely shielded from electron wave," *Physical Review Letters*, vol. 56, no. 8, pp. 792–795, Feb. 24, 1986, Publisher: American Physical Society.

[85] W. Gerlach and O. Stern, "Der experimentelle Nachweis der Richtungsquantelung im Magnetfeld," *Zeitschrift für Physik*, vol. 9, no. 1, pp. 349–352, Dec. 1, 1922, 0044-3328.

[86] I. I. Rabi, J. R. Zacharias, S. Millman, and P. Kusch, "A new method of measuring nuclear magnetic moment," *Physical Review*, vol. 53, no. 4, pp. 318–318, Feb. 15, 1938, Publisher: American Physical Society.

[87] I. I. Rabi, "Space quantization in a gyrating magnetic field," *Physical Review*, vol. 51, no. 8, pp. 652–654, Apr. 15, 1937, Publisher: American Physical Society.

[88] N. F. Ramsey, "A new molecular beam resonance method," *Physical Review*, vol. 76, no. 7, pp. 996–996, Oct. 1, 1949, Publisher: American Physical Society.

[89] J. M. Raimond, M. Brune, and S. Haroche, "Manipulating quantum entanglement with atoms and photons in a cavity," *Reviews of Modern Physics*, vol. 73, no. 3, pp. 565–582, Aug. 28, 2001, Publisher: American Physical Society.

[90] M. Brune, S. Haroche, V. Lefevre, J. M. Raimond, and N. Zagury, "Quantum nondemolition measurement of small photon numbers by rydberg-atom phase-sensitive detection," *Physical Review Letters*, vol. 65, no. 8, pp. 976–979, Aug. 20, 1990, Publisher: American Physical Society.

[91] A. Peters, K. Yeow Chung, and S. Chu, "High Precision Gravity Measurements Using Atom Interferometry," in *34th Rencontres de Moriond: Gravitational Waves and Experimental Gravity*, Hanoi: The Gioi world Publishers, 2000, pp. 411–420.

[92] B. Canuel, A. Bertoldi, L. Amand, *et al.*, "Exploring gravity with the miga large scale atom interferometer," *Scientific Reports*, vol. 8, no. 1, p. 14 064, 2018.

[93] M. Kasevich and S. Chu, "Atomic interferometry using stimulated raman transitions," *Physical review letters*, vol. 67, no. 2, p. 181, 1991.

[94] C. J. Bordé, "Atomic interferometry with internal state labelling," *Physics Letters A*, vol. 140, no. 1, pp. 10–12, Sep. 4, 1989, 0375-9601.

[95] V. Ménoret, P. Vermeulen, N. Le Moigne, *et al.*, "Gravity measurements below 10−9 g with a transportable absolute quantum gravimeter," *Scientific Reports*, vol. 8, no. 1, p. 12 300, Aug. 17, 2018, 2045-2322.

[96] D. M. Giltner, R. W. McGowan, and S. A. Lee, "Atom interferometer based on bragg scattering from standing light waves," *Physical review letters*, vol. 75, no. 14, p. 2638, 1995.

[97] H. Müller, S.-w. Chiow, S. Herrmann, S. Chu, and K.-Y. Chung, "Atom-interferometry tests of the isotropy of post-newtonian gravity," *Physical Review Letters*, vol. 100, no. 3, p. 031 101, 2008.

[98] T. Kovachy, P. Asenbaum, C. Overstreet, *et al.*, "Quantum superposition at the half-metre scale," *Nature*, vol. 528, no. 7583, pp. 530–533, Dec. 2015, Number: 7583 Publisher: Nature Publishing Group, 1476-4687.

[99] D. J. Wineland, "Nobel lecture: Superposition, entanglement, and raising schrödinger's cat," *Reviews of Modern Physics*, vol. 85, no. 3, pp. 1103–1114, 2013.

[100] M. A. Lombardi, T. P. Heavner, and S. R. Jefferts, "Nist primary frequency standards and the realization of the si second," *NCSLI Measure*, vol. 2, no. 4, pp. 74–89, 2007.

[101] C. Wood, S. Bennett, D. Cho, *et al.*, "Measurement of parity nonconservation and an anapole moment in cesium," *Science*, vol. 275, no. 5307, pp. 1759–1763, 1997.

[102] A. D. Ludlow, M. M. Boyd, J. Ye, E. Peik, and P. O. Schmidt, "Optical atomic clocks," *Reviews of Modern Physics*, vol. 87, no. 2, pp. 637–701, 2015.

[103] M. Takamoto, F.-L. Hong, R. Higashi, and H. Katori, "An optical lattice clock," *Nature*, vol. 435, no. 7040, pp. 321–324, 2005.

[104] J. Guéna, M. Abgrall, D. Rovera, *et al.*, "Progress in atomic fountains at lne-syrte," *IEEE transactions on ultrasonics, ferroelectrics, and frequency control*, vol. 59, no. 3, pp. 391–409, 2012.

[105] D. Budker and M. Romalis, "Optical magnetometry," *Nature physics*, vol. 3, no. 4, pp. 227–234, 2007.

[106] F. Riehle, T. Kisters, A. Witte, J. Helmcke, and C. J. Bordé, "Optical ramsey spectroscopy in a rotating frame: Sagnac effect in a matter-wave interferometer," *Physical Review Letters*, vol. 67, no. 2, pp. 177–180, Jul. 8, 1991, Publisher: American Physical Society.

[107] W. Ketterle, D. S. Durfee, and D. Stamper-Kurn, "Making, probing and understanding bose-einstein condensates," in *Bose-Einstein condensation in atomic gases*, IOS Press, 1999, pp. 67–176.

[108] P. Cladé, E. De Mirandes, M. Cadoret, *et al.*, "Determination of the fine structure constant based on bloch oscillations of ultracold atoms<? format?> in a vertical optical lattice," *Physical review letters*, vol. 96, no. 3, p. 033 001, 2006.

[109] S. Fray, C. A. Diez, T. W. Hänsch, and M. Weitz, "Atomic interferometer with amplitude gratings of light and its applications<? format?> to atom based tests of the equivalence principle," *Physical Review Letters*, vol. 93, no. 24, p. 240 404, 2004.

[110] Y. Shin, M. Saba, T. Pasquini, W. Ketterle, D. Pritchard, and A. Leanhardt, "Atom interferometry with bose-einstein condensates in a double-well potential," *Physical review letters*, vol. 92, no. 5, p. 050 405, 2004.

[111] B.-G. Englert, J. Schwinger, and M. O. Scully, "Is spin coherence like humpty-dumpty? i. simplified treatment," *Foundations of Physics*, vol. 18, no. 10, pp. 1045–1056, Oct. 1, 1988, 1572-9516.

[112] B. Dubetsky and M. Kasevich, "Atom interferometer as a selective sensor of rotation or gravity," *Physical Review A—Atomic, Molecular, and Optical Physics*, vol. 74, no. 2, p. 023 615, 2006.

[113] S. Kleinert, E. Kajari, A. Roura, and W. P. Schleich, "Representation-free description of light-pulse atom interferometry including non-inertial effects," *Physics Reports*, vol. 605, pp. 1–50, 2015.

[114] C. Overstreet, P. Asenbaum, and M. A. Kasevich, "Physically significant phase shifts in matter-wave interferometry," *American Journal of Physics*, vol. 89, no. 3, pp. 324–332, Mar. 2021, 0002-9505, 1943-2909.

[115] M. Zimmermann, M. A. Efremov, A. Roura, *et al.*, "T3-interferometer for atoms," *Applied Physics B*, vol. 123, no. 4, p. 102, Mar. 20, 2017, 1432-0649.

[116] J. D. R. Tommey and S. D. Hogan, "Matter-wave interferometry with helium atoms in low-l rydberg states," *Physical Review A*, vol. 104, no. 3, p. 033 305, Sep. 3, 2021, Publisher: American Physical Society.

[117] D. Chan and J. Martin, "Comment on "matter-wave interferometry with helium atoms in low-l rydberg states"," *Physical Review A*, vol. 109, no. 1, p. 017 301, 2024.

[118] E. H. Kennard, "Zur Quantenmechanik einfacher Bewegungstypen," *Zeitschrift für Physik*, vol. 44, no. 4, pp. 326–352, Apr. 1, 1927, 0044-3328.

[119] O. Amit, Y. Margalit, O. Dobkowski, *et al.*, "${T}^{3}$ stern-gerlach matter-wave interferometer," *Physical Review Letters*, vol. 123, no. 8, p. 083 601, Aug. 21, 2019, Publisher: American Physical Society.

[120] G. W. F. Drake, "High precision theory of atomic helium," *Physica Scripta*, vol. 1999, p. 83, T83 Jan. 1, 1999, Publisher: IOP Publishing, 1402-4896.

[121] Y. Pu, D. D. Neufeld, and F. B. Dunning, "Ionization of rydberg atoms at metallic surfaces: Influence of stray fields," *Physical Review A*, vol. 81, no. 4, p. 042 904, Apr. 30, 2010, Publisher: American Physical Society.

[122] J. D. Carter and J. D. D. Martin, "Energy shifts of rydberg atoms due to patch fields near metal surfaces," *Physical Review A*, vol. 83, no. 3, p. 032 902, Mar. 7, 2011, Publisher: American Physical Society.

[123] B. R. Johnson, J. O. Hirschfelder, and K.-H. Yang, "Interaction of atoms, molecules, and ions with constant electric and magnetic fields," *Reviews of Modern Physics*, vol. 55, no. 1, pp. 109–153, Jan. 1, 1983, Publisher: American Physical Society.

[124] W. E. Lamb, "Fine structure of the hydrogen atom. III," *Physical Review*, vol. 85, no. 2, pp. 259–276, Jan. 15, 1952, Publisher: American Physical Society.

[125] J. P. Dowling, C. P. Williams, and J. D. Franson, "Maxwell duality, lorentz invariance, and topological phase," *Physical Review Letters*, vol. 83, no. 13, pp. 2486–2489, Sep. 27, 1999, Publisher: American Physical Society.

[126] A. Cimmino, G. I. Opat, A. G. Klein, *et al.*, "Observation of the topological aharonov-casher phase shift by neutron interferometry," *Physical Review Letters*, vol. 63, no. 4, pp. 380–383, Jul. 24, 1989, Publisher: American Physical Society.

[127] K. Sangster, E. A. Hinds, S. M. Barnett, and E. Riis, "Measurement of the aharonov-casher phase in an atomic system," *Physical Review Letters*, vol. 71, no. 22, pp. 3641–3644, Nov. 29, 1993, Publisher: American Physical Society.

[128] S. Lepoutre, A. Gauguet, M. Büchner, and J. Vigué, "Test of the he-mckellar-wilkens topological phase by atom interferometry. i. theoretical discussion," *Physical Review A—Atomic, Molecular, and Optical Physics*, vol. 88, no. 4, p. 043 627, 2013.

[129] M. Wilkens, "Quantum phase of a moving dipole," *Physical Review Letters*, vol. 72, no. 1, pp. 5–8, Jan. 3, 1994, Publisher: American Physical Society.

[130] H. Wei, R. Han, and X. Wei, "Quantum phase of induced dipoles moving in a magnetic field," *Physical Review Letters*, vol. 75, no. 11, pp. 2071–2073, Sep. 11, 1995, Publisher: American Physical Society.

[131] S. Lepoutre, A. Gauguet, G. Trénec, M. Büchner, and J. Vigué, "He-McKellar-wilkens topological phase in atom interferometry," *Physical Review Letters*, vol. 109, no. 12, p. 120 404, Sep. 21, 2012, 1079-7114.

[132] A. Ruschhaupt and J. G. Muga, "Three-dimensional effects in atom diodes: Atom-optical devices for one-way motion," *Physical Review A*, vol. 76, no. 1, p. 013 619, Jul. 18, 2007, Publisher: American Physical Society.

[133] J. J. Thorn, E. A. Schoene, T. Li, and D. A. Steck, "Experimental realization of an optical one-way barrier for neutral atoms," *Physical Review Letters*, vol. 100, no. 24, p. 240 407, Jun. 20, 2008, Publisher: American Physical Society.

[134] A. Ruschhaupt and J. G. Muga, "Control of atomic motion with an atom-optical diode on a ring," *Journal of Physics B: Atomic, Molecular and Optical Physics*, vol. 41, no. 20, p. 205 503, Oct. 2008, 0953-4075.

[135] L. Landau, "Diamagnetismus der Metalle," *Zeitschrift für Physik*, vol. 64, no. 9, pp. 629–637, Sep. 1, 1930, 0044-3328.

[136] M. Ericsson and E. Sjöqvist, "Towards a quantum hall effect for atoms using electric fields," *Physical Review A*, vol. 65, no. 1, p. 013 607, Dec. 13, 2001, 1050-2947, 1094-1622.

[137] L. R. Ribeiro, C. Furtado, and J. R. Nascimento, "Landau levels analog to electric dipole," *Physics Letters A*, vol. 348, no. 3, pp. 135–140, Jan. 2, 2006, 0375-9601.